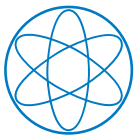

Fakultät für Physik
Technische Universität München

Advanced Acquisition, Reconstruction and Quantification Methods for Magnetic Resonance Spectroscopy and Spectroscopic Imaging

Jorge Eduardo Coello Uribe

Fakultät für Physik
Technische Universität München

Advanced Acquisition, Reconstruction and Quantification Methods for Magnetic Resonance Spectroscopy and Spectroscopic Imaging

Jorge Eduardo Coello Uribe

Vollständiger Abdruck der von der Fakultät für Physik der Technischen Universität München zur Erlangung des akademischen Grades eines

Doktors der Naturwissenschaften (Dr. rer. nat.)

genehmigten Dissertation.

Vorsitzender:

Prof. Dr. Martin Zacharias

Prüfende der Dissertation:

Prof. Dr. Axel Haase

Priv.-Doz. Dr. Marion I. Menzel

Die Dissertation wurde am 18.11.2020 bei der Technischen Universität München eingereicht und durch die Fakultät für Physik am 09.11.2021 angenommen.

Acknowledgements

First, my sincere acknowledgment to Prof. Dr. Axel Haase, PD. Dr. Marion Menzel and Prof. Dr. Bjoern Menze for the academic supervision of this Ph.D. thesis. Special thanks to Dr. Anja Drescher for her valuable work at the Munich School of Bioengineering.

My deepest gratitude to the team at GE Global Research, Dr. Timo Schirmer, Dr. Rolf Schulte, Dr. Cristina Cozzini, Dr. Ralph Noeske, Dr. Jonathan Sperl, and Dr. Dirk Bequé. Thank you for your scientific guidance and professional advice. Specially, thank you for the great working atmosphere and for the opportunity to learn and grow professionally being part of this team.

My most sincere gratitude to Dr. Alex Lin and the team at BWH. Thanks for contributing significantly to my professional development and academic career. I learned a lot being part of your group and enjoyed the always friendly and welcoming environment.

Thanks to all the collaborators for their time and effort put in this work. In UCSF, Dr. Peder Larson, Dr. Brian Burns, Dr. Jeremy Gordon, Dr. Jason Crane and all the people at the department of Radiology and Biomedical Imaging.

To my dear colleagues and friends from TU München and GE Global Research.

To all my friends, for their advice and all experiences we have shared together.

To my family, for always giving me the strength and motivation to achieve greater things.

To Sandra, for always being there with your unconditional support and love.

This work was partly supported by the doctoral fellowship CONACyT–DAAD (91549693) and the Bavaria California Technology Center (BaCaTeC).

Abstract

In recent years, advances in medical imaging technologies like Magnetic Resonance (MR) Imaging have demonstrated their potential to positively impact the diagnosis and treatment of diseases, improving the life quality of individuals. Specifically, two modalities that are particularly interesting for the medical community are MR Spectroscopy (MRS) and Spectroscopic Imaging (MRSI) capable of mapping the metabolic composition of tissues.

The present thesis addresses the major challenges of this technique that limits the access to MRS and MRSI examinations and their adoption in the medical practice. The work focuses on the development of optimized acquisition and reconstruction methods to achieve higher robustness, sensitivity, and speed. Thus, improving the reliability of the examinations and diagnosis made by the radiologist.

The obtained improvements in acquisition sequences, signal reconstruction, signal enhancement, and data visualization are presented and validated. These major developments include: (i) A reconstruction framework that enabled accelerated brain MRSI with an improved signal quality and reduced artifacts, acquired in standard MR systems (3 Tesla) within a clinically relevant time, (ii) an MRSI methodology optimized for ultra-high magnetic fields (7 Tesla) that enabled high-resolution metabolite mapping, and (iii) machine learning methods for an improved signal quantification in MRS and MRSI.

Zusammenfassung

Fortschritte in den medizinisch bildgebenden Verfahren, wie Magnetresonanztomographie (MRT), haben in den letzten Jahren gezeigt, dass sie das Potenzial haben, die Diagnose und Behandlung von Krankheiten und die Lebensqualität von Menschen zu verbessern. MR-Spektroskopie (MRS) und MR Spektroskopische-Bildgebung (MRSI) sind Technologien, die für die Medizin und die Wissenschaft interessant sind, als sie die metabolische Zusammensetzung von Geweben messen können.

Diese Dissertation befasst sich mit den großen Herausforderungen, die diese bildgebenden Verfahren haben, die die Verfügbarkeit und Akzeptanz dieser Art von Studien in der medizinischen Praxis einschränken. Die Arbeit konzentriert sich auf die Entwicklung optimierter Aufnahme- und Rekonstruktionsmethoden, um eine höhere Empfindlichkeit und Geschwindigkeit zu erreichen. Somit verbessert sich die Zuverlässigkeit der vom Radiologe durchgeführten Untersuchungen und Diagnosen.

Verbesserungen in den Pulssequenzen, der Signalrekonstruktion, der Signalverarbeitung und der Datenvisualisierung werden vorgestellt und validiert. Zu diesen wichtigen Entwicklungen gehören: (i) eine Rekonstruktionsmethode, die beschleunigte Gehirn MRSI mit verbesserter Signalqualität und reduzierten Artefakten ermöglichte, die in Standard MR Systemen (3 Tesla) innerhalb einer klinisch relevanten Zeit gemessen wurden, (ii) eine MRSI Methodologie, die für ultrahohe Magnetfelder (7 Tesla) optimiert wurde und hochauflösende MRSI Bilder ermöglichte, und (iii) Maschinenlernalgorithmen, die die Quantifizierung von Metaboliten und Gewebe in MRS und MRSI verbessern können.

List of Publications

Journal Papers

E. Coello, F. S. Hafalir, R. Noeske, M. I. Menzel, A. Haase, B. Menze, and R. F. Schulte. Overdiscrete Echo-Planar Spectroscopic Imaging with Correlated Higher-Order Phase Correction. In: *Magnetic Resonance in Medicine*. Volume 84(1), 11–24 (2019).

E. Coello, R. Noeske, B. Burns, J. W. Gordon, A. Jakary, B. Menze, A. Haase, P. E. Z. Larson, Y. Li, and R. F. Schulte. High-Resolution Echo-Planar Spectroscopic Imaging at Ultra-High Field. In: *NMR in Biomedicine*. Volume 31(11), e3950 (2018).

E. Coello, J. I. Sperl, Dirk Bequé, T. Benz, K. Scherer; A. Sztrókay-Gaul, K. Hellerhoff; F. Pfeiffer, C. Cozzini, and S. Grandl. Fourier Domain Image Fusion for Differential X-ray Phase-Contrast Breast Imaging. In: *European Journal of Radiology*. Volume 89, 27–32 (2017).

M. Wu, H. T. Mulder, P. Baron, **E. Coello**, M. I. Menzel, G. C. van Rhoon, and A. Haase. Correction of Motion-Induced susceptibility Artifacts and B_0-Drift During Proton Resonance Frequency Shift-Based MR Thermometry in the Pelvis with Background Field Removal Methods. In: *Magnetic Resonance in Medicine*. Volume 84(5), 2495-2511 (2020).

Book Chapters

E. Coello, T. C. Starr, and A. P. Lin. Magnetic Resonance Spectroscopy Methods. In: Kubicki M., Shenton M. *Neuroimaging in Schizophrenia.* Springer Cham (2020).

Conference Papers

D. Das, **E. Coello**, R. F. Schulte, and B. Menze. Quantification of Metabolites in Magnetic Resonance Spectroscopic Imaging using Machine Learning. In: *MICCAI: International Conference on Medical Image Computing and Computer-Assisted Interventions* (2017).

D. Das, **E. Coello**, R. F. Schulte, and B. Menze. Spatially Adaptive Spectral Denoising for MR Spectroscopic Imaging using Frequency-Phase Non-Local Means. In: *MICCAI: International Conference on Medical Image Computing and Computer-Assisted Interventions* (2016).

Conference Abstracts

E. Coello, R. Huang, M. F. Charney, W. Zhao, H. Liao, C. Choi, and A. P. Lin. Long Term Monitoring of Brain Tumors Using MR Metabolic Phenotyping. In: *Proc Intl Soc Mag Reson Med* (2020).

E. Coello, N. R. Bolo, H. Liao, A. Awad, M. A. Niznikiewicz, and A. P. Lin. Reproducibility of Auditory Functional Magnetic Resonance Spectroscopy at 7T. In: *Proc Intl Soc Mag Reson Med* (2020).

E. Coello, M. F. Charney, T. C. Starr, H. Liao, M. Louis and A. P. Lin. Estimation of Brain Tissue Composition and Voxel Location in MR Spectroscopy Using Neural Networks. In: *Proc Intl Soc Mag Reson Med* (2019).

E. Coello, N. R. Bolo, G. Chiou, H. Liao, M. F. Charney, T. C. Starr, E. C. Del Re, M. A.

Niznikiewicz, and A. P. Lin. Functional Magnetic Resonance Spectroscopy of the Sensory and Attentional Auditory Processing at 7T. In: *Proc Intl Soc Mag Reson Med* (2019).

E. Coello, H. Liao, C. Papaleo, M. F. Charney, T. C. Starr, E. C. Del Re, S. K. Merugumala, S. Waisbren, and A. P. Lin. Regional Differences in Cerebral Phenylalanine Measured with Single Voxel Spectroscopy using PRESS Localization and LCModel Quantification. In: *Proc Intl Soc Mag Reson Med* (2019).

E. Coello, R. Noeske, B. Burns, J.W. Gordon, A. Jakary, B. Menze, A. Haase, P.E.Z. Larson, Y. Li, and R. F. Schulte. High Resolution Semi-LASER Localized Echo Planar Spectroscopic Imaging at Ultra High Field. In: *Proc Intl Soc Mag Reson Med* (2018).

D. Das, **E. Coello**, A. Sekuboyina, R. F. Schulte, B. Menze. Direct Estimation of Model Parameters in Magnetic Resonance Spectroscopic Imaging using Deep Learning. In: *Proc Intl Soc Mag Reson Med* (2018).

M. Wu, P. Baron, H. T. Mulder, **E. Coello**, M. I. Menzel, G. C. Van Rhoon, A. Haase. Correction of Motion-Induced Artifacts in PRFS MR Thermometry During Mild Hyperthermia in the Pelvis. In: *Proc Intl Soc Mag Reson Med* (2018).

E. Coello, F. S. Hafalir, B. Menze, A. Haase, R. F. Schulte. High-Resolution Phase Correction in Overdiscrete Spectroscopic Imaging Reconstruction using Piecewise Polynomial Interpolation. In: *Proc Intl Soc Mag Reson Med* (2017).

E. Coello, E. S. Hansen, C. Laustsen, B. Menze, A. Haase, R. F. Schulte. Overdiscrete Reconstruction for Signal Enhancement in Hyperpolarized ^{13}C Spectroscopic Imaging. In: *Proc Intl Soc Mag Reson Med* (2017).

E. Coello, R. Noeske, B. Menze, A. Haase, R. F. Schulte. Overdiscrete Reconstruction for Signal Enhancement in Single Voxel Spectroscopy. In: *Proc Intl Soc Mag Reson Med* (2017).

D. Das, **E. Coello**, R. F. Schulte, B. Menze. Spectral-Dephasing based Non-Local Means for Spatially Adaptive Denoising in 3D-MRSI. In: *Proc Intl Soc Mag Reson Med* (2017).

T. J. Hoh, **E. Coello**, J. Carretero, A. Haase, R. F. Schulte. Temperature Mapping of Fluorinated (^{19}F) Gas in a Cool Down Experiment. In: *Proc Intl Soc Mag Reson Med* (2017).

E. Coello, M. A. Janich, T. Schirmer, R. Noeske, T. Borbath, A. Haase, R. F. Schulte. Overdiscrete Reconstruction in Echo-Planar Spectroscopic Imaging with Auto-Calibrated B_0-Field Map Estimation. In: *Proc Intl Soc Mag Reson Med* (2016).

E. Coello, J.I. Sperl, D. Bequé, K. Scherer, S. Grandl, K. Willer, L. Birnbacher, A. Sztrókay-Gaul, K. Hellerhoff, M. Chabior, J. Herzen, P. Edic, M. Reiser, F. Pfeiffer and C. Cozzini. Fourier domain image fusion framework for analysis and visualization of attenuation, phase and dark field information retrieved in differential X-ray Phase Contrast Imaging. In: *IMXP: International Symposium on Biomedical Applications of X-Ray Phase Contrast Imaging* (2015).

Contents

Part I.

Introduction and Theoretical Background

1. Introduction

In the last century, developments in medical imaging technologies have improved patient-specific health care, positively impacting the diagnosis, monitoring, and treatment of diseases. Yet, one of the major challenges in this field is to obtain the most amount of diagnostic information in a clinically relevant time and with sufficient quality to get meaningful conclusions out of it. Among a wide variety of technologies used every day in a clinical environment, magnetic resonance (MR) imaging gained special attention in radiology due to their versatility and the wide variety of applications where it provides quantitative anatomical and functional information. However, access to this technology is still limited due to its cost and the relatively long time that MR scans take.

In this field, MR spectroscopy (MRS) and spectroscopic imaging (MRSI) are unique modalities that provide a quantitative measurement of the metabolic composition of tissues and its spatial distribution. These technologies allow measuring changes in the chemical components of tissues with high specificity, which is of great interest in many clinical applications [7], like breast [41], prostate [58] and central nervous system (CNS) disorders [80, 112]. Furthermore, its clinical value has been shown with studies in oncology, neurodegenerative diseases, psychiatric disorders, ischemia, and traumatic brain injury, among others.

Nevertheless, the fundamentally low concentration of metabolites in the brain results in a low sensitivity limiting the maximum spatial resolution and minimum acquisition time in this type of examinations. Despite the clinical interest and the availability of this modality in clinical systems for more than a decade, its adoption as a diagnostic tool has

been slow due to its complexity. Moreover, the adoption of more sensitive modalities such as positron emission tomography (PET) partially replaced MRSI as a metabolic diagnostic tool for some metabolic diseases. Yet, proton MRS and MRSI remain of great interest due to its non-invasive nature, flexibility, and diagnostic potential.

Achieving high-resolution distribution of metabolic information within a clinically relevant time remains one of the major challenges of MRSI. Furthermore, the complex of the spectro-spatial information acquired has typically low signal to noise ratio (SNR) and the potential presence of nuisance signals and artifacts. For this reason, a robust framework that includes accelerated acquisitions, advanced signal processing, accurate quantification, and an intuitive visualization needs to be properly implemented to allow technologists and radiologists to obtain meaningful scans that can be used for diagnostic purposes.

1.1. Thesis Description

In the present dissertation, contributions in Magnetic Resonance Spectroscopy and Spectroscopic Imaging are described. The main challenges of these technologies slowing their effective translation into clinics are addressed. First, the basic physical principles and clinical applications of MRS and MRSI are introduced in Chapter 2. Then the main body of this work is described, which has been divided into four major contributions:

- **Chapter 3.** A novel reconstruction method combined with accelerated acquisitions was developed to improve the spatial and spectral quality of MRSI. The methodology included the development of a robust framework that minimized system instabilities patient motion and artifacts. Moreover, an automatic measurement, estimation, and correction of physical disturbances were performed.

- **Chapter 4.** A fast MRSI acquisition method optimized for ultra-high magnetic fields (7T) was developed and evaluated. This enabled high-resolution metabolite mapping of the in a clinically relevant time and showing a high correlation with anatomical structures.

- **Chapter 5.** A machine learning methodology for the estimation of tissue composition in an MRS volume was trained and evaluated, reducing the variability and improving voxel placement accuracy compared to manually placed voxels.

- **Chapter 6.** A methodology for the absolute quantification of low-concentration molecules that have downfield resonances using standard widely available pulse sequences was developed. The method was implemented to measure primarily the concentration of cerebral phenylalanine accumulation in the brain in a population of patients with phenylketonuria.

2. Theoretical Background

This chapter presents a general introduction of the physical principles of nuclear magnetic resonance (NMR), MR spectroscopy (MRS) and spectroscopic imaging (MRSI). Additionally, the description of standard acquisition and reconstruction techniques used in clinical examinations is presented. Although similar methodologies are applicable for different nuclei, such as Carbon-13 (^{13}C), Phosphorus-31 (^{31}P), Fluorine-19 (^{19}F) and Sodium-23 (^{23}Na), the main application of this work is in-vivo proton (^{1}H) MRS and MRSI.

2.1. Principles of Magnetic Resonance Spectroscopy

2.1.1. Nuclear Magnetic Resonance

Nuclear magnetic resonance (NMR) is the study of magnetic properties of nuclei with a nuclear spin $I > 0$ [20]. The nuclear spin is a quantum mechanical entity, that can be conceptualized as a magnetic moment $\vec{\mu}$ that spins around its own axis (Figure 2.1). When this spin is placed under a magnetic field $\vec{B_0}$, it starts oscillating or precessing in a three-dimensional cone at a frequency known as the Larmor frequency, given by

$$\omega_0 = \gamma \vec{B_0}. \tag{2.1}$$

where γ denotes the gyromagnetic ratio (for protons $\gamma \approx 26.75 \cdot 10^7$ radT^{-1} s^{-1}). This frequency is typically in the mega Hertz regime (MHz) and is directly proportional to the external magnetic field B_0 expressed in Tesla (T) and the gyro-magnetic ratio.

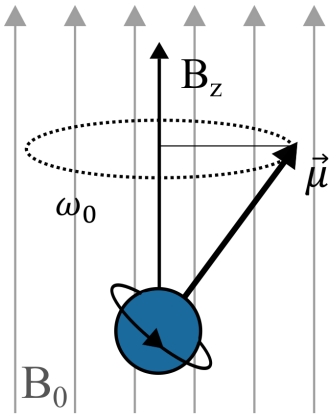

Figure 2.1.: The magnetic moment $\vec{\mu}$ precesses about the static magnetic field B_z with the Larmor frequency ω_0. Modified from [23].

In order to model the effects of the spins in a larger scale, the signal can be defined as the sum of all nuclear magnetic moments, or the magnetization $\vec{M}$, defined as

$$\vec{M} = \left(M_{xy0}\cos\left(\gamma B_{z0}t + \varphi\right), -M_{xy0}\sin\left(\gamma B_{z0}t + \varphi\right), M_{z0}\right)^{\mathrm{T}}, \tag{2.2}$$

In thermal equilibrium the transverse magnetization $M_{xy}(t)$ cancels out due to the randomly distributed phase φ. At this point, the quantum mechanical argumentation is needed. In classical physics, the potential energy $E_{\mathrm{pot}} = -\vec{\mu}\cdot\vec{B_0}$ could take any value between $-\mu B_0$ and $+\mu B_0$ [20]. However, the quantum theory postulates that the angular frequency is quantized to discrete values. Generally, the corresponding quantum number m can have $2I+1$ values. In case of protons, the spin is $I = \frac{1}{2}$ and thus two orientations between $\vec{\mu}$ and B_0 and accordingly two energy states are allowed (Figure 2.2.b). The splitting of the states is called the Zeeman effect and increases linearly with the magnetic field strength. Thus, the NMR signal generated from the net magnetization is proportional to the difference of the population of both states

$$n_{\mathrm{L}} - n_{\mathrm{H}} \approx \frac{n\hbar\cdot\gamma\cdot \mathrm{B}_0}{2\cdot k_{\mathrm{B}}\cdot T}, \tag{2.3}$$

with n_L and n_H indicating population of low and high energy states respectively, n is the total number of spins inside the sample, k_B the Boltzmann constant and T the temperature

in Kelvin (K) [20].

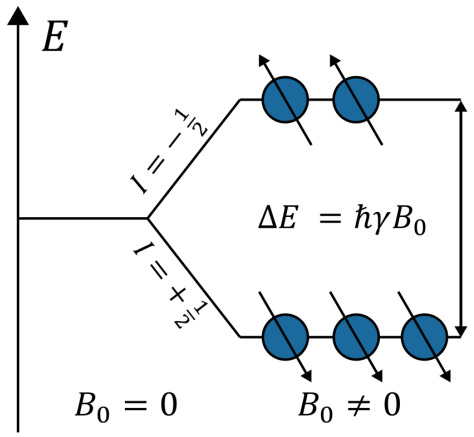

Figure 2.2.: Inside an external magnetic field, energy states split proportional to the field strength. Modified from [23].

Generally, the direct detection of this longitudinal magnetization is not feasible because its relatively small magnitude is overwhelmed by the larger magnetization contributions from electron current. Hence, to perform an NMR measurement, the magnetization is taken into the transverse plane via an oscillating magnetic field $\vec{B_1}(t)$. In this way, the spins precessing at the range of the specific Larmor frequency (for protons at $B_0 = 3\,\mathrm{T}$, $f_0 = 127.7\,\mathrm{MHz}$) induce a current in a receiver coil, which records the signal. The strength of the induced NMR signal, proportional to the number of spins in the orientation parallel to the external magnetic field with respect to the spins in anti-parallel orientation.

2.1.2. Radio-Frequency Pulses

The measurement of the net macroscopic magnetization $\vec{M_0}$ requires a second oscillating magnetic field called $\vec{B_1}(t)$ field, which is much smaller in magnitude than B_0. The effect of this field, applied as a radio-frequency pulse and following the resonance condition $\omega_{\mathrm{RF}} = \omega_0$, causes the magnetization to be flipped into the transverse plane. The time-dependent motion of the magnetization is fully described by the Bloch equations [20]

$$\dot{\vec{M}}(t) = \begin{pmatrix} -\frac{1}{T_2} & \gamma B_0 & -\gamma B_{1y} \\ -\gamma B_0 & -\frac{1}{T_2} & \gamma B_{1x} \\ \gamma B_{1y} & -\gamma B_{1x} & -\frac{1}{T_1} \end{pmatrix} \vec{M}(t) + \begin{pmatrix} 0 \\ 0 \\ \frac{M_0}{T_1} \end{pmatrix} \tag{2.4}$$

where T_1 denotes the longitudinal relaxation time or spin-lattice relaxation, T_2 denotes the transverse relaxation time or spin-spin relaxation.

The rotating magnetization is detected by a receiving coil in the transverse plane, where the change of magnetic flux induces a voltage according to Faraday's law of induction. Due to transverse relaxation, the measured signal shows an exponential decay, also known as free induction decay (FID). Finally, the frequency components of the signal, i.e. the spectrum, are obtained from the 1D Fourier transform of the FID, following the reconstruction pipeline that will be described later in this chapter.

Adiabatic Condition

An effective method for inverting nuclear spins over a wide frequency band is adiabatic fast passage [57]. To achieve this, the following adiabatic condition need to be satisfied

$$\mid \frac{\mathrm{d}\theta}{\mathrm{d}t} \mid \ll \omega_{\text{eff}} \tag{2.5}$$

where $\omega_{\text{eff}} = \gamma \mathrm{B}_{\text{eff}}$ is the angular frequency of the effective field that results from the applied RF field $\omega_1 = \gamma \mathrm{B}_1$ and the resonance offset $\Delta\omega$, and where ω is the angle of B_{eff} with respect to the +x axis.

2.1.3. MR Relaxometry

Following the RF excitation, the net magnetization will return to thermal equilibrium following tissue-specific time constants, namely T_1 and T_1 relaxation, which represent perhaps of the most important source of contrast in MR imaging and are of special interest for quantitative MRI. Quantitative relaxometry aims to map the properties of tissue (T_1, T_2, T_2^*) in absolute units that are independent of the MR systems and protocols, providing a metric for the objective study of physiological and pathological conditions in a non-invasive

manner [64, 12].

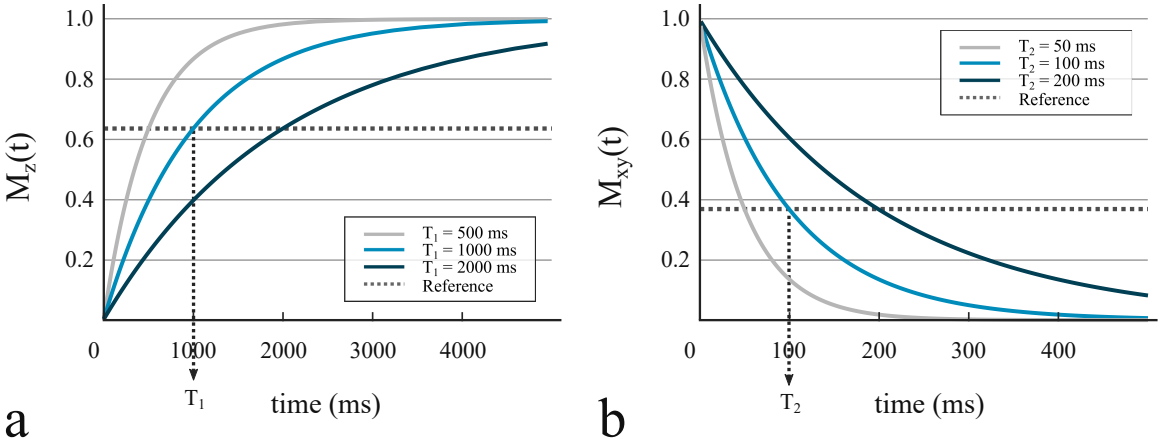

Figure 2.3.: (a) Characteristic curve for the longitudinal magnetization recovering that follows the T_1 relaxation constant. Relaxation curves are shown for different T_1 values and the threshold from which the value is calculated (∼63% of the normalized signal magnitude) (b) Exponential decay of the transverse magnetization following T_2 relaxation constant. Curves for different T_2 values showing the threshold from which the T_2 value is determined (∼37% of the normalized signal). Adapted from [22]

T_1 Relaxation (Spin-Lattice)

T_1 relaxation, originated by the interaction of the spins with surrounding molecules, resulting in a loss of energy. The T_1 relaxation is defined by the Block equation

$$\frac{\delta M_z(t)}{\delta t} = \frac{M_0 + M_z(t)}{T_1} \tag{2.6}$$

In the case of protons (^{1}H), T1 relaxation involves an exchange of energy between water protons and the surrounding lipids, proteins, and macromolecules also referred to as lattice (Figure 2.3.a).

T_2 Relaxation (Spin-Spin)

In an MR experiment, the measured transverse component of the magnetization decays following T_2 relaxation, caused by phase incoherence due to spin-spin interactions. It is

described by the following equation

$$\frac{\delta M_{xy}(t)}{\delta t} = -\frac{M_{xy}(t)}{\mathrm{T}_2} \tag{2.7}$$

T_2 relaxation in the ^{1}H case is originated by the interactions protons, mainly in the water molecules. Each individual spin will experience a slightly different local magnetic field due to the close presence of other spins, this changes the precessing frequency and ultimately cause them to dephase. Figure2.3.b shows decay in the magnetization for different T_2 values.

T_2^* Relaxation

Along with spin-spin interactions, dephasing may also be induced by the local B_0-field inhomogeneities. This effect, combined with the T_2^* known as T_2^* relaxation, generates a faster signal decay due to an additional term $T_2^{'}$ that represents the irrecoverable loss of the transverse magnetization. The combination of T_2 and $T_2^{'}$ is defined as T_2^*, where $1/T_2^* = 1/T_2 + 1/T_2^{'}$ [22].

2.1.4. Chemical Shift

Shielding effects that are caused by the magnetic moment associated with the electrons in the atomic shell reduce the effective magnetic field seen by the nucleus. This magnetization is usually opposed to the external static field, hence the magnetic field strength becomes $B = B_0(1 - \sigma)$, with shielding constant σ. As a result, the resonance frequency of protons will slightly change, shifting the resonance peaks of that specific nucleus, in the spectrum. To make the chemical shift independent of the magnetic field strength, it is calculated relative to a reference substance

$$\delta = \frac{\omega - \omega_{\mathrm{ref}}}{\omega_{\mathrm{ref}}} \times 10^6 \tag{2.8}$$

which corresponds to a scalar given in parts-per-million (ppm). Tetramethylsilane (TMS) is commonly used as a reference compound with a resonance peak defined at 0 ppm, allowing

the chemical shift of most molecules to be positive. Proton MRS and MRSI, also known as chemical shift imaging (CSI), exploit the chemical shift phenomenon to separate metabolic compounds that contain protons from the water signal.

2.1.5. MR Spatial Encoding

In MR imaging, the spatial distribution of spins is measured using spatially-varying magnetic field gradients that induce a change in the magnetic field, hence changing the resonance frequency of spins. The resulting field is denoted as

$$B_z\left(\vec{r}\right) = B_0 + \vec{G}\left(t\right) \cdot \vec{r} \qquad \text{where} \qquad \vec{G} = \left(\frac{\partial B}{\partial x}, \frac{\partial B}{\partial y}, \frac{\partial B}{\partial z}\right)^T. \tag{2.9}$$

Slice Selection

By inducing an additional component in the magnetic field through a spatially varying magnetic gradient, the selection of a slice in one of the main image axis or an arbitrary plane. Then the Larmor frequency is modified as follows

$$\omega(z) = \omega_0 + \gamma G_z(z). \tag{2.10}$$

By application of simultaneously switched on sinc-shaped RF-pulse and slice gradient G_z, only the spins with resonance frequencies inside this bandwidth are excited, therefore a slice along z-direction is selected. A sinc RF excitation pulse is chosen as it corresponds to a rectangle in the Fourier domain, ideally exciting a rectangular profile (Figure 2.4.a).

Phase Encoding

For the second image dimension, a perpendicular gradient G_y is applied after the slice selection.Before switching on G_y, the spins precess with Larmor frequency. As it is switched on for a time period τ, they start to precess with different angular frequencies. Hence, they gain an extra phase

$$\varphi\left(y\right) = \gamma \int_0^\tau G_y\left(t\right) y \, \mathrm{d}t \tag{2.11}$$

that is characteristic for the local position along the gradient axis. Therefore in order to cover the whole k-space, N_y repetitions of the slice excitation are needed for the measurement. This process is depicted in Figure 2.4.c.

Frequency Encoding

Similarly, a frequency encoding along the x-axis is performed to using a gradient G_x. This gradient is active during the whole sampling of the signal, also known as the readout gradient. As a result, the spins precess locally with a varying frequency accross the x-axis

$$\omega(x) = \omega_0 + \gamma G_x(x). \tag{2.12}$$

Hence, each frequency is characteristic for the location along the gradient dimension. Since local information is contained in the frequency spectrum, it can be retrieved by the inverse Fourier transform (FT).

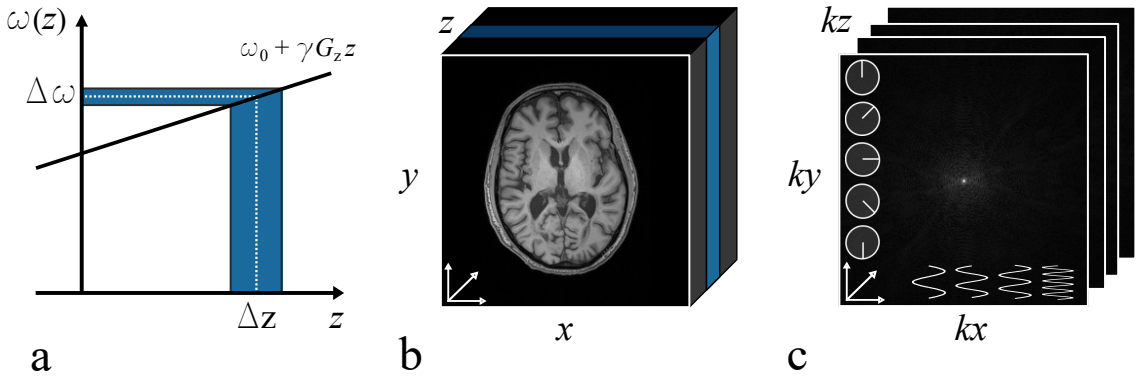

Figure 2.4.: (a) Slice selection principle. Spins in a single slice are excited by simultaneous application of an RF-pulse and a gradient modulation. The center frequency determines the position and the bandwidth determines the slice thickness. Adapted from [23]. (b) Image space showing selected slice (blue) in the z-axis. (c) Measured k-space using spatial encoding in-plane. This is done via frequency-encoding along the x-axis and phase-encoding along the y-axis.

Chemical Shift Displacement Error

A wrong mapping of two substances with different chemical shift might occur since the frequency encoding will fail. In imaging, this is usually visible for water and lipid signals and called chemical shift artifact or chemical shift displacement error (CSDE). The fat appears shifted along the frequency encoding direction. Since slice selection also depends on the frequency, it is also affected by this artifact. Using a high transmitter and receiver bandwidth minimizes the displacement.

The CSDE is proportional to the magnitude of the magnetic field and inversely proportional to the bandwidth of the RF pulse:

$$\mathrm{CSDE}(\delta) = \frac{\Delta\delta \mathrm{B}_0}{\mathrm{BW}}. \tag{2.13}$$

where $\Delta\delta$ is the chemical shift difference in ppm between the metabolite component and the carrier frequency of the RF field, B_0 represents the frequency of the main magnetic field and BW is the bandwidth of the RF pulse [4].

2.2. Single Voxel Spectroscopy

In Figure 2.5, an exemplary human brain spectrum is shown. It contains signals of the most predominant metabolites present in the human brain. It is solely intended to give a short overview of the spectral positions of the major contributions of these metabolites. For a more detailed description of their meaning to spectroscopy and physiology, see [31, 20]. The focus in this work lies on the three major metabolite resonances, namely N-acetyl-aspartate (NAA), creatine (Cre), and choline (Cho). Other metabolites that can be detected in proton spectroscopy, namely myo-inositol (Ins), glutamate (Glu), glutamine (Gln), and γ-aminobutyric acid (GABA). Macromolecules (MM) are also visible in spectra and contribute to a broad baseline. In the presence of lipids appear in the spectrum as a broad resonance peak.

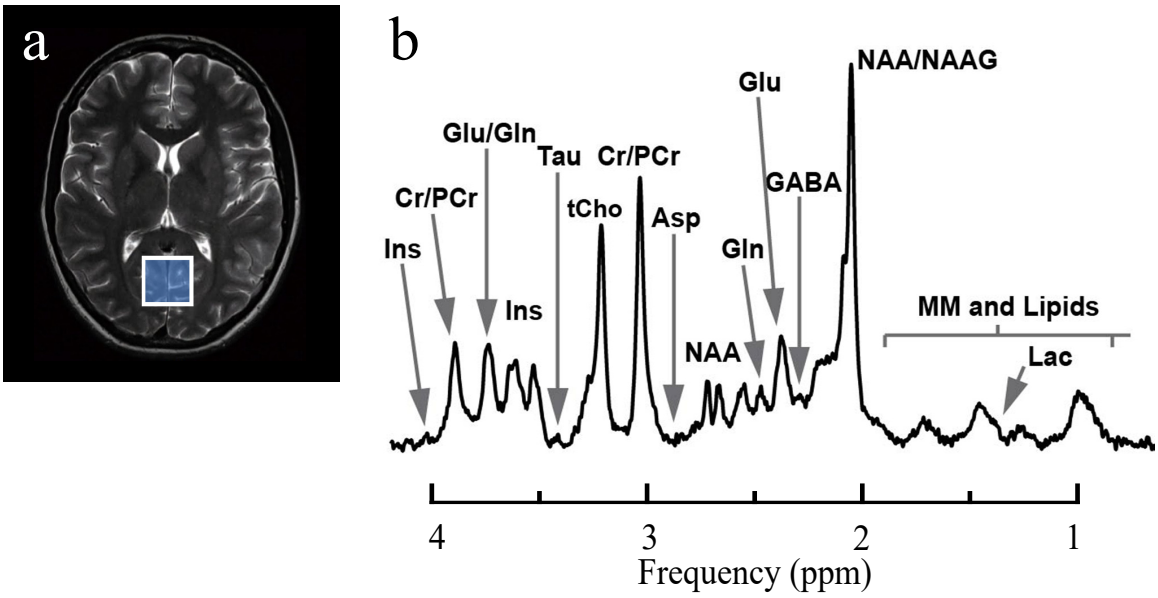

Figure 2.5.: Exemplary brain spectrum of a $8\,\mathrm{cm}^3$ voxel inside the occipital lobe published by Öz et al [80]. The single-voxel spectrum is acquired with TE/TR = 8/5000 ms and 128 repetitions. It shows signal of the main metabolites present in the human brain.

2.3. Brain Metabolites

In organic molecules, the abundance of hydrogen (^{1}H) and its relatively high NMR signal, enables the detection of resonances of interest for the study of the central nervous system (CNS). However, the detection of these neuro-metabolites has some limitations and depends on the magnetic field strength, hardware sensitivity, spectral overlap, artifacts, and patient motion. Here, the most relevant brain metabolites that can be measured and quantified under healthy and disease conditions using clinical MR scanners, typically at 3T, are introduced. In Figure 2.5, a representative ^{1}H MRS examination is shown together with the measured spectrum and the different metabolic components present in it.

N-acetyl aspartate (NAA)

NAA is a metabolite synthesized in neurons [73]. It is considered a marker of metabolic health of neurons, axons, and dendrites [111], and the concentration of NAA has been cor-

related with the number of neurons, however, the main role of NAA in the central nervous system is not yet fully understood [6]. Under healthy conditions, the main resonance of NAA, located at 2.02 ppm, corresponds to the typically largest peak in the spectrum. Its diagnostic value is well known in MRS, identifying conditions by either comparing the numeric values of NAA concentrations or by recognizing abnormal patterns of peaks in the spectra [61, 36, 74].

Creatine (Cr)

Creatine (Cr) is a metabolite that shows the main resonance at 3.02 ppm. The metabolism of Cr and phospho-creatine (PCr) provides insight into energy metabolism in the brain, where Cr phosphorylation is performed by the enzyme creatine kinase and adenosine triphosphate (ATP) to form PCr [98]. The ratio to Cr is typically used to report normalized concentrations as Cr concentration has a low variation in different areas of the brain. However, it is important to keep in mind that under specific conditions, like mitochondrial dysfunction, energy metabolism may change, impacting the reliability of concentration ratios. Changes in Cr and PCr and have been reported in neuropsychiatric diseases including schizophrenia and bipolar disorders [93].

Choline (Cho)

Molecules containing choline (Cho), also referred to as total Cho (tCho), include different metabolites, mainly: choline, phosphorylcholine (PC), and glycerophosphorylcholine (GPC) as well as, phosphorylethanolamine (PE) and glycerophosphorylethanolamine, to a lesser extent [20]. The largest resonance peak is a singlet at 3.2 ppm. These molecules are components of myelin, important for the propagation of neuronal signals. For this reason, high Cho levels are found in the white matter. Moreover, PC and GPC are involved in the metabolism of membrane phospholipids. Thus, it is a sensitive marker of membrane condition, due to the involvement of Cho in both membrane turnover and degradation. Recent reports on Cho levels in conditions like schizophrenia [51], Alzheimer's disease [43],

and depression [16] have not shown consistent results. However, consistently elevated tCho in the basal ganglia in bipolar disorder has been published [63]. A reason for these conflicting findings even within the same disease could be to the sensitivity of Cho to the proportion of gray and white matter tissue in the measured MRS voxel. A solution to this problem is to account for the relative contributions of gray and white within the voxel of interest for MRS matter. This concept will be described in Chapter 5 and an alternative method for this calculation will be presented.

Glutamate (Glu)

Glutamate (Glu) is an amino acid with important functions in the brain and it is the most abundant excitatory neurotransmitter. High concentrations of Glu result in and are an indication of neuronal dysfunction. Additionally, Glu is a key element in the citric acid cycle important for the energy metabolism of the brain. Astrocytes uptake most extracellular Glu and regulate the low extracellular concentration needed for proper receptor-mediated functions [104, 103]. Glu is stored as glutamine (Gln) in the glial cells, and the cycle between these two neuro-metabolites is crucial for the correct functioning of the brain [33, 66].

Glutamine (Gln)

Glutamine (Gln) is the main precursor of Glu and GABA within the brain [38]. It has been reported that more than 80% of the cerebral glucose consumption is originated from the cycling between Gln and Glu [105, 82]. The structures, and consequently MR spectra, of Glu and Gln are very similar [31], and although Glu has a relatively higher concentration in the brain, its major resonances usually overlap with contributions from Gln, GABA, GSH, and NAA. For this reason, a more reliable measurement is provided by the combined concentrations of Glu and Gln, known as Glx.

γ-Amino Butyric Acid (GABA)

GABA is an inhibitory neurotransmitter interesting for the study of a broad range of psychiatric conditions like anxiety, memory changes, pain, and depression. The detection of GABA with MRS is challenging due to its relatively low concentration in the brain, between 1.3 â 1.9 mM [31], therefore it is difficult to quantify it accurately. Moreover, GABA spins couple with other neighboring spins, originating multiple resonances around 1.9 ppm, 2.28 ppm, and 3.0 ppm, that overlap with other resonances such as NAA, Glu, and Cr, respectively. Therefore, specialized sequences, such as spectral editing or 2D spectroscopy, are needed to reliably measure GABA concentrations in vivo.

Myo-inositol (mI)

Myo-inositol (mI) is a cyclic sugar-alcohol with the main resonance peak at 3.52 ppm. mI is involved in different metabolic processes [97], from cerebral osmotic regulation to demyelination. mI has been found to be highly specific and sensitive in disease diagnosis of patients when compared with healthy controls. Studies of dementia have highlighted the importance of mI being highly sensitive and specific in the diagnosis of Alzheimer's disease [80]. In mild cognitive impairment (MCI), an early stage of dementia, mI is elevated before symptoms are obvious [44]. Moreover, in combination with NAA, mI predicts the outcome of MCI patients.

Glutathione (GSH)

Glutathione (GSH) is an antioxidant that plays a major role in oxidative stress [24], from which the brain is especially vulnerable and can cause DNA damage, lipid peroxidation, and protein modification. Oxidative stress is also strongly associated with neuroinflammatory processes [2, 75]. Therefore, GSH metabolism is involved in the pathogenesis of neurodegenerative disorders as well as psychiatric disorders. GSH provides an interesting cellular specificity to inflammatory processes as it is synthesized differently between neurons, astrocytes, and glial cells. GSH is composed of Glu, cysteine, and glycine, therefore its

spectrum highly overlaps with all three of those metabolites [68]. 2D spectroscopy methods and spectral editing can be implemented to effectively measure the resonances of GSH.

2.4. MR Spectroscopic Imaging

2.4.1. Signal Model

The general MRSI experiment consist in acquiring the signal $m_\gamma(\mathbf{k}, t)$ for every coil element γ, at a k-space position $\mathbf{k}$ and the temporal point t. This signal is modeled as follows

$$m_\gamma(\mathbf{k}, t) = \int \int_{FOV} p(\mathbf{r}, f) \cdot s_\gamma(\mathbf{r}) \cdot e^{-i2\pi \mathbf{k}_\kappa \cdot \mathbf{r}} \cdot e^{-i2\pi (f + \Delta f(\mathbf{r})) \cdot t} d\mathbf{r}\, dt, \tag{2.14}$$

where $p(\mathbf{r}, f)$ corresponds to the signal of interest at the spatial position $\mathbf{r}$ and resonance frequency f. The signal is spectrally ($e^{-i2\pi(f+\Delta f(\mathbf{r}))\cdot t}$) and spatially ($e^{-i2\pi \mathbf{k}_\kappa \cdot \mathbf{r}}$) encoded and weighted by the complex sensitivity operator $s_\gamma(\mathbf{r})$ of each receiver coil γ. For spins precessing at frequency f, Eq. 2.14 can be expressed as

$$m_\gamma(\mathbf{k}, t) = \int \int_{FOV} p(\mathbf{r}, f) \cdot s_\gamma(\mathbf{r}) \cdot e^{-i2\pi \mathbf{k}_\kappa \cdot \mathbf{r}} \cdot e^{-i2\pi \Delta f(\mathbf{r}) \cdot t} d\mathbf{r}\, dt, \tag{2.15}$$

and reduced to

$$m_\gamma(\mathbf{k}, t) = \int \int_{FOV} p(\mathbf{r}, f) \cdot \mathbf{e}_{\gamma,\kappa}(\mathbf{r}) \cdot e^{-i2\pi \Delta f(\mathbf{r}) \cdot t} d\mathbf{r}\, dt, \tag{2.16}$$

where $\mathrm{e}_{\gamma,\kappa}(\mathbf{r})$ is the spatial and sensitivity encoding term. Thus, an encoding matrix, which includes the spatial Fourier encoding term and the coil sensitivity information $s_\gamma(\mathbf{r})$, can be built as follows

$$E_{(\gamma,\kappa),\,\rho} = s_\gamma(\mathbf{r}) \cdot e^{-i2\pi \mathbf{k}_\kappa \cdot \mathbf{r}}. \tag{2.17}$$

This encoding operator allows to state, for a single time point, the reconstruction problem in matrix form as follows

$$\mathbf{m} = E\mathbf{p} + \eta, \tag{2.18}$$

where $\mathbf{m}$ corresponds to the measurements in vector form, E corresponds to the encoding matrix and $\mathbf{p}$ the spatial distribution of the spin density.

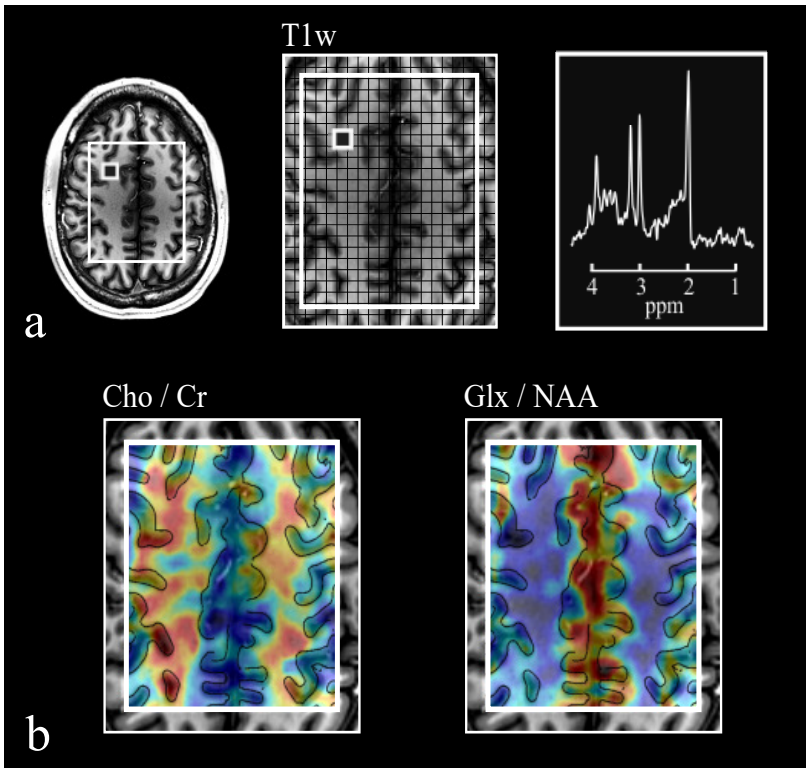

Figure 2.6.: Exemplary brain MRSI examination showing the (a) prescribed volume of interest (VOI) displayed using the anatomical images, an exemplary grid representing the voxel size of the reconstructed data and the spectrum of a representative white matter voxel. (b) Reconstructed metabolite ratio maps showing the contrast in composition between gray and white matter anatomical structures.

2.5. MRS / MRSI Acquisition

A typical MRS / MRSI acquisition sequence consists of magnetization preparation, excitation, and signal readout through spectro-spatial encoding. In principle, each part is independent of the other and thus the pulse sequence can be designed according to the application. Preparative techniques include signal saturation, inversion recovery, and outer volume suppression (OVS).

Another important factor in MRS is an excited ROI. In single voxel spectroscopy, in particular, a localization technique that ensures that exclusively the desired voxel is excited is needed. Localization is not only restricted to single voxel spectroscopy but can also be

applied in CSI. Exciting any lipids are often carefully avoided in order to prevent distortions in the wanted signal.

2.5.1. Spatial Localization

Spatial localization modules are pulse sequences that selectively excite a given volume of tissue V. This allows getting rid of nuisance signals surrounding the tissue of interest. Moreover, B_0-field inhomogeneity can be further optimized for the selected area using shim coils, thus improving the spectral line width and the quality of the measurement. Note that the spatially localized volume is often improved by additional OVS bands around the ROI.

Point-Resolved Spectroscopy (PRESS)

Point-resolved spectroscopy (PRESS) is a localization pulse sequence that consists of a slice selective $90°$ pulse followed by two slice selective refocusing $180°$ pulses [14][50]. Each pulse is applied in conjunction with an orthogonal gradient (G_z, G_y, G_x) turned on (Figure 2.7.a). The first pulse excites an axial slice Δz, whereas the other two pulses only refocus the proton spins inside the intersection of these three perpendicular slices.

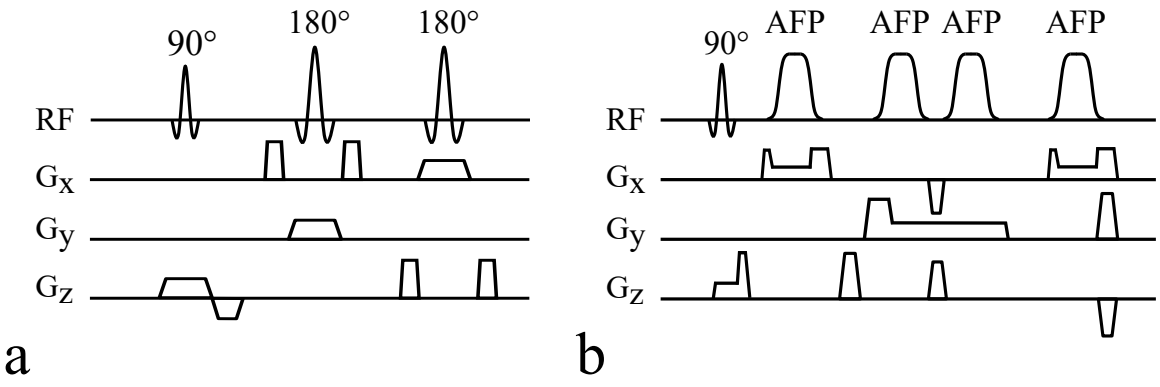

Figure 2.7.: (a) PRESS localization sequence diagram. (b) Semi-LASER localization pulse sequence diagram. A 90°excitation pulse followed by a pair of adiabatic full passage (AFP) refocusing pulses used in combination with gradient modulations. The high bandwidth of AFP pulses allows to substantially reduce the CSDE in-plane.

Semi-Localization by Adiabatic Selective Refocusing (semi-LASER)

Semi-LASER is an improved localization method that makes use of amplitude and frequency modulated adiabatic full passage (AFP) refocusing pulses. The sequence diagram is depicted in Figure 2.7.b. A Shinnar-Le-Roux optimized $90°$ slice selective pulse is followed by a pair of $180°$ adiabatic hyperbolic secant slice selective refocusing pulses [101, 102]. In order to prevent spurious echoes, crusher gradients are turned on before and after the slice selective pulses. Thanks to the adiabatic pulses, slice excitation is less sensitive to B_1^+-field inhomogeneities, resulting in the advantage of more accurate localization over a greater volume of interest. Due to higher energy deposition, SAR limits need to be considered.

2.5.2. Water Suppression

In MRS, suppressing the overwhelming water signal prior to the excitation of the metabolites is designed. Without water suppression, the water signal would introduce artifacts such as a complex baseline into the metabolite signal, which hinders the reliable quantification of low concentration metabolites.

Chemical Shift Selective Saturation (CHESS)

CHESS is a magnetization preparation method for signal saturation. Its core consists of a tissue-selective $90°$-pulse that is followed by strong crusher gradients. The crusher gradients dephase the magnetization and consequently, the unwanted net magnetization is destroyed. The selective pulse ensures that only the unwanted signal is affected and the remaining signal is retained [34]. In principle, the selective pulse can be tuned to any resonance frequency, but here it is used for suppression of water. In order to achieve higher signal suppression, subsequent CHESS pulses are applied. The schematic sequence diagram is depicted in Figure 2.8.a.

Variable Power and Optimized Relaxation Delays (VAPOR)

There are other water suppression techniques besides the ones mentioned above. One of them is called VAPOR and is based on the same idea as CHESS. Its core consists of 8 CHESS pulses with variable RF power and optimized time delays between the pulses, in contrast to CHESS, where both are constant. For efficient signal suppression, the initial flip angle can be calibrated. An advantage over CHESS is increased B_1 and T_1 insensitivity [110].

On the other hand, at $800\,\mathrm{ms}$, the VAPOR technique demands a considerably longer time frame than CHESS, which increases the minimum TR of the sequence. Also, higher exposure to RF energy in comparison to CHESS might limit usage at higher field strengths.The sequence diagram is shown in Figure 2.8.b.

OVS is also based on the same idea as CHESS. Instead of a chemical shift selective pulse, it functions selectively in space. Hence, the signal is eliminated inside the entire spatial band. Several saturation bands can be placed around the skull in order to suppress lipid regions. However, placing them can be time-consuming and difficult to realize in practice, especially in three-dimensional scans.

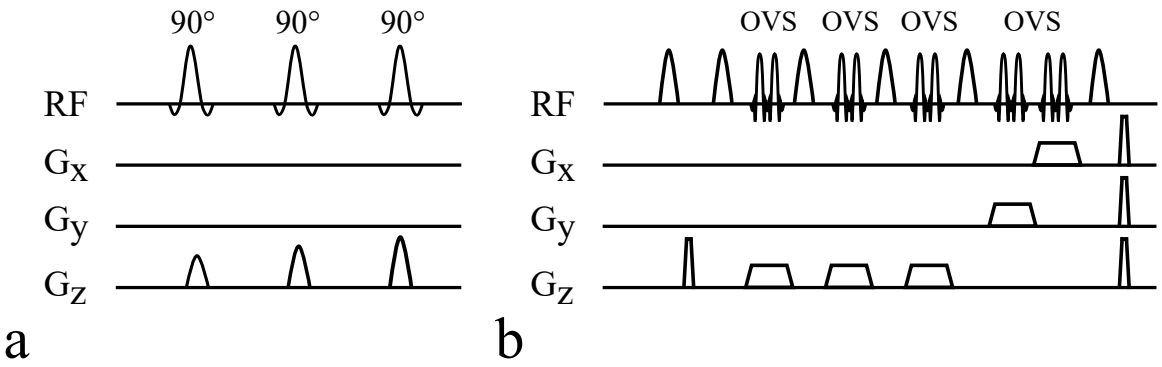

Figure 2.8.: Water suppression using (a) CHESS sequence with $3\times$ pulses and (b) VAPOR combined with $8\times$OVS bands for a better selection profile.

2.5.3. Spectro-Spatial Encoding

In MRSI, numerous spectro-spatial readout methods with differences in k-space sampling trajectories have been proposed. These present differences in encoding efficiency, speed,

and SNR. Hence, the selection of the readout methodology is highly dependent on the application. Here, two well-known techniques will be described to give insight into the range of possibilities when selecting the encoding strategy.

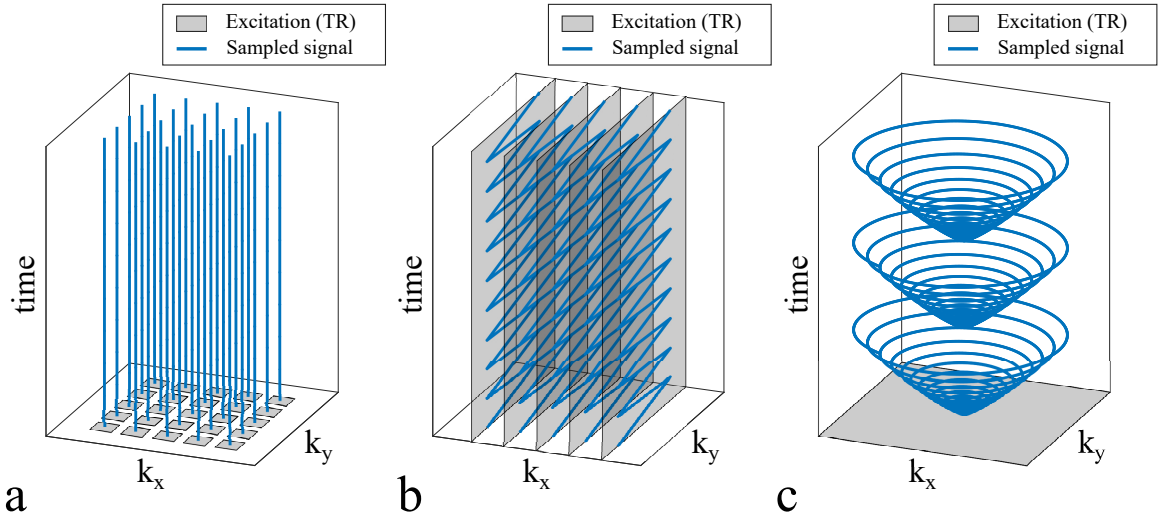

Figure 2.9.: Spectro-spatial encoding techniques showing the signal readout in blue and the each excitation block in gray, which corresponds to a TR. (a) Standard PE MRSI, (b) EPSI with a symmetric readout trajectory and (c) spiral MRSI.

Phase Encoded MR Spectroscopic Imaging (PE MRSI)

Phase Encoded MRSI (PE MRSI), is a standard technique where one echo or FID is sampled at every TR, sampling one point in k-space at a time (Figure 2.9.a). Phase encoding gradients localize the signal in k-space and no gradients are used during the readout. As this sequence requires one phase encoding step for all spatial dimensions, its encoding efficiency is very low, making this readout method inherently slow. As an example, a 2D PE MRSI scan with a matrix size of 32×32 and a TR of $1\,\mathrm{s}$ would require $17\,\mathrm{min}\ 4\,\mathrm{s}$, and a 3D scan would require n_z times longer, with n_z being the number of phase encodes in $z-$direction. This is at the limit of clinically feasible times, which is the major limitation of PE MRSI. Recent methods have been proposed to use ultra-short TR PE MRSI accelerated with parallel imaging [35, 78], which allows for 3D scans in a feasible time ($\Gamma 30 min$).

Echo Planar Spectroscopic Imaging (EPSI)

Echo Planar Spectroscopic Imaging (EPSI) is an encoding-efficient MRSI technique that achieves a significant acceleration compared to standard PE MRSI. EPSI enables the simultaneous acquisition of one spatial dimension and the time signal in one TR. EPSI is based on the same principle as echo-planar imaging (EPI), where a full plane in k-space is encoded after a single excitation module. The spectro-spatial encoding is performed by an oscillating gradient sampling the echo or FID during the readout. In EPSI, the k_x-t-plane or k_x-t-plane is sampled analogous to the k_x-k_y-plane in echo-planar imaging (Figure 2.9.b).

EPSI sequences are typically implemented using two types of k-space trajectories, namely, symmetric and flyback readouts. Flyback EPSI samples the signal exclusively during positive lobes of the readout gradient. This has the advantage of being more robust to system imperfections and timing errors since the flyback gradient causes the sampling points to be well aligned. Nevertheless, the dead time spent in the flyback portion of the trajectory reduces the encoding efficiency. Moreover, for high-resolution or high-bandwidth acquisitions, the gradient requirements are usually not met by standard MRI gradients, thus interleaved acquisitions are required, increasing scanning time. Symmetric EPSI, on the other hand, samples the signal during both positive and negative gradient lobes. This improves the encoding efficiency. However, inconsistencies in odd and even k-space lines [30] of the symmetric trajectory, cause phase differences and ghosting artifacts that need to be corrected in an additional step. Chapter 4 presents a method to perform this correction between even and odd lines, enabling high-resolution and high-bandwidth MRSI at 7T.

Spiral Spectroscopic Imaging (Spiral MRSI)

Spiral MRSI uses the interleaving of spiral encoding in 2D and 3D for the acquisition (Figure 2.9.c). This approach offers a higher acceleration and more an encoding-efficient readout than EPSI [27]. Furthermore, it provides the flexibility to shape the point spread function.

Nevertheless, data reconstruction is computationally demanding due to the non-cartesian spatial encoding and more sensitive to off-resonance effects which require additional

corrections. Additionally, as it also occurs with EPSI, the encoding of a large k-space coverage is limited by the gradient maximum gradient performance [87].

2.6. MRS / MRSI Reconstruction

MR data reconstruction, depending on the modality, has specific and flexible processing pipelines that need to be executed to obtain a meaningful physical measure from the raw data. In this section, a standard generic pipeline for MRS and MRSI is described (Figure 2.10). This pipeline should serve as a reference to understand the improved methods developed as part of this work. Typically, a main water-suppressed scan is acquired and a supplementary water-reference scan serves as the calibration data that allows correcting for signal disturbances, such as Eddy currents, and also to properly scale the spectrum to perform absolute metabolite quantification.

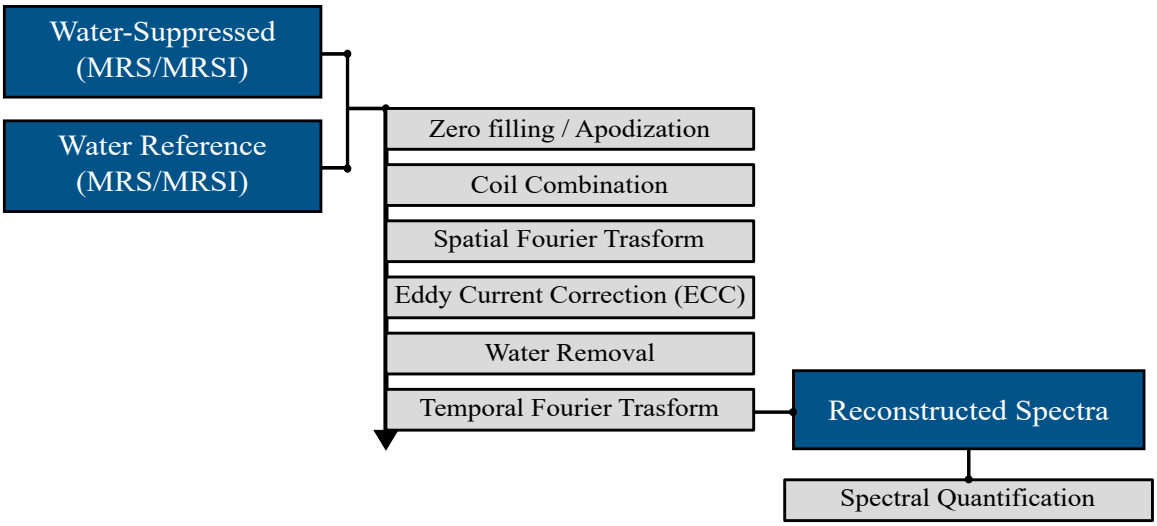

Figure 2.10.: Generic reconstruction pipeline for MRS and MRSI reconstruction of raw data. The main difference between the single voxel MRS and MRSI processing is the additional spatial Fourier transform that retrieves the spatial distribution from the encoded signal in k-space.

2.6.1. Zero Filling and Apodization

The most common interpolation method in both spectral and spatial domain is based on the FT. This is performed by zero-filling the higher-order Fourier coefficients of the signal prior to the FT. This originates a virtually higher spectral and spatial resolution but no actual information is added to the data [9, 25]. Furthermore, spectral and spatial apodization allows weighting the frequency components of the signal using different filter functions, e.g. Hamming or Gaussian windows, to improve SNR [40]. Chapter 3 presents a novel methodology to interpolate the MRSI signal into a higher resolution to correct for magnetic field inhomogeneities, phase disturbances and reduce the spatial response function of the acquisition, overall improving signal quality and measurement robustness.

2.6.2. Multi-Channel Signal Combination

There are different designs of receiver coils. State-of-the-art coil systems are built as phased arrays, where several coils overlap and each coil is associated with its own channel [96]. Multi-channel receiver coils achieve a higher sensitivity. In this type of hardware, the signal is pre-amplified individually to minimize noise correlation. The combination of a multi-channel signal can be then performed by measuring the complex sensitivity profile of each element and include this term in the encoding operator (Eq. 2.17).

In the absence of sensitivity information, the signal of multi-element receiver coils can be combined by phasing the signal of each coil element and adding the signal coherently using weights from the maximum averaged magnitude [99, 94]. Given the time-domain signal $y_\gamma(t, \mathbf{r})$ at voxel position r measured with the γ-th coil element, singular value decomposition (SVD) is computed for the maximum temporal signal at each voxel position $\mathbf{r}$, obtaining $\mathbf{Y} = \mathbf{U\Sigma V}^*$. The weight w_γ for each coil element is then estimated from the normalized singular vector in V corresponding to the largest singular value

$$w_\gamma(\mathbf{r}) = \frac{\mathbf{v}^*_{\gamma,\sigma_\mathbf{1}}}{\sum_\gamma \mid \mathbf{v}^*_{\gamma,\sigma_\mathbf{1}} \mid}, \tag{2.19}$$

where * denotes the complex conjugate and σ_1 the largest singular value. The term $w_\gamma(\mathbf{r})$ contains the relative phase and scaling information for each coil. Finally, the combined

temporal signal $S(t, \mathbf{r})$ at voxel position $\mathbf{r}$ is obtained as follows

$$S(t, \mathbf{r}) = \sum_{\gamma} w_{\gamma}(\mathbf{r}) \cdot y_{\gamma}(t, \mathbf{r}). \tag{2.20}$$

Acquisition in multiple independent channels cannot only be used for SNR-enhancement, but also for reduction of acquisition time, as it is done parallel imaging methodologies, e.g. SENSE [92], GRAPPA [32] and SPIRiT [62].

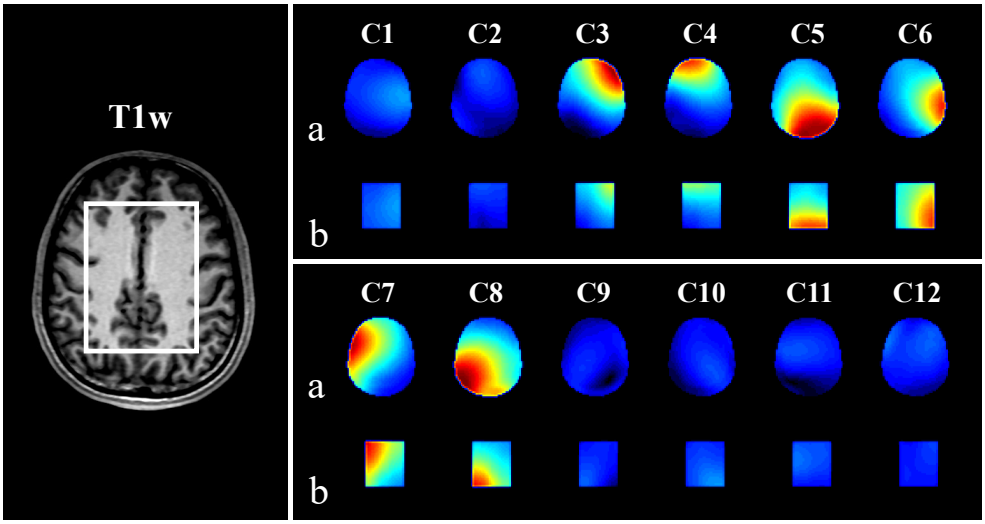

Figure 2.11.: Coil sensitivity profiles (magnitude) of a 12-channel coil. (a) Measured sensitivity using standard sequence (ASSET) and (b) estimated sensitivity from a reference water signal using SVD phasing and weight estimation for every voxel.

2.6.3. Eddy Current Correction

During the MR acquisition experiments, the hardware interaction with the changes in the magnetic field originated mainly by the gradients, generate Eddy currents that introduce disturbances in the phase component of the measured signal. In the case of MRS and MRSI, these effects could be very harmful as the disturbances in the large water signal may propagate to regions where resonances of important metabolites are located, affecting their correct quantification. The widely used Eddy current correction (ECC) method in MRS and MRSI [49], uses a water reference scan (W_{ref}), i.e. an acquisition with identical scanning

settings but without water suppression, to estimate the phase of this signal the time domain and subtract it from the water-suppressed scan (W_{sup}) as follows

$$S^{\text{ECC}}(t) = S(t) \cdot e^{i\varphi_{W_{\text{sup}}}} \cdot e^{-i\varphi_{W_{\text{ref}}}}. \tag{2.21}$$

A major limitation of this method occurs in the presence of lipids or any large nuisance signal. As this phase estimation relies on a water reference with only one component and negligible contributions form metabolite, lipids, and macromolecules.

2.6.4. Residual Water Removal

Water suppression modules are routinely used as a standard element of the MRS and MRSI acquisition sequences to substantially reduce the magnitude of the water signal, which is around 3 to 4 orders of magnitude higher than the metabolites. However, the resulting spectrum contains inevitably a residual contribution of water that may corrupt the baseline and metabolite signals. For this reason, further removal of the water signal needs to be performed by signal decomposition of the spectrum. The most widely used method to remove residual water is Hankel singular value decomposition (HSVD) [8, 40], which decomposes the time domain signal into decaying sinusoidal signals and removes the coefficients that correspond to a specific spectral range. Then a temporal Fourier transform retrieves the water-subtracted spectrum. Alternative approaches for water removal are based on solving an optimization problem to separate metabolite and water signals [10].

2.7. MRS / MRSI Quantification

Quantitative MRS and MRSI require estimating the relative area of the resonance peaks, which are proportional to their concentration in tissue [20].

Fitting algorithms based prior knowledge have shown superior robustness to non-linear distortions present in the spectra, such as Eddy currents, baseline, linear and zero-phase effects. Most widely used commercially available software are jMRUI [76], AMARES [113], Tarquin [65] and LCModel [91]. These tools are based on modeling a linear combination of

metabolite spectra, which are generated via simulations, signal models, or measured with high quality under identical experimental conditions.

For the purpose of the present thesis, LCModel has been the standard quantification methodology using simulated datasets for short TE PRESS and semi-LASER sequences at two different field strengths (3T and 7T). Figure 2.12 shows a representative report generated from LCModel. The fitting algorithm estimates and separates the metabolite signal from the estimated baseline component and the noise. Moreover, a list of the absolute and relative concentrations and Cramer-Rao Lower Bound (CRLB) is computed for each metabolite component that was simulated and included in the analysis.

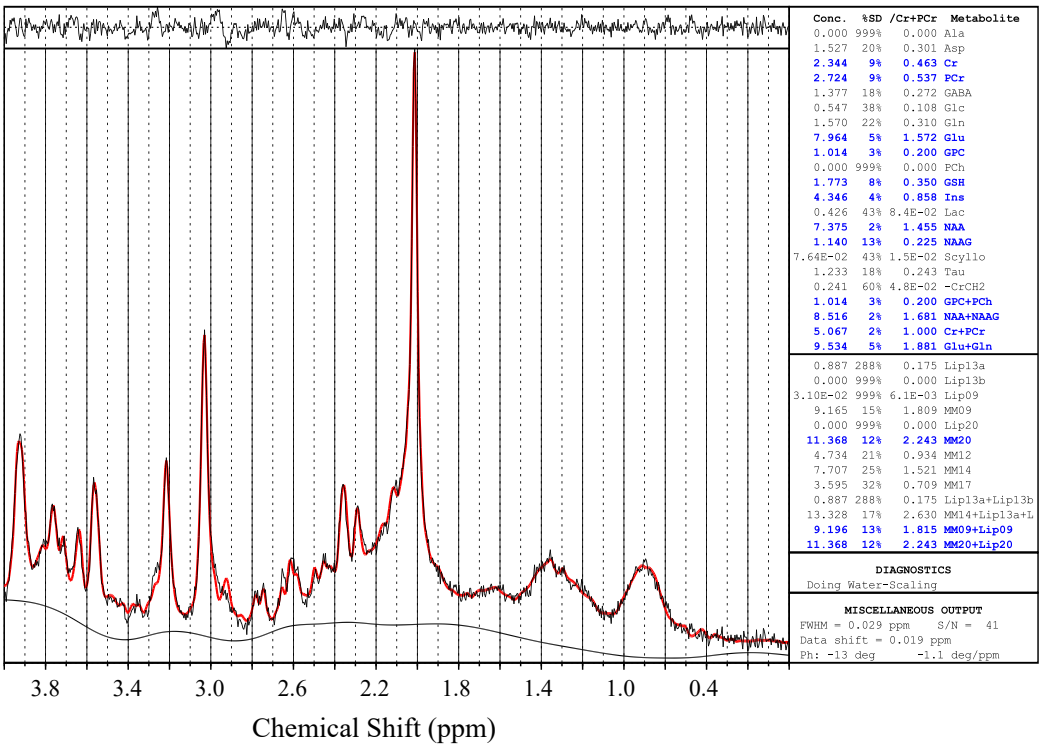

Figure 2.12.: Spectral quantification output obtained using LCModel [91]. The spectral fit using a simulated metabolite basis set estimates the baseline, noise and the zero- and first order phase of the signal. Moreover, the concentration values, relative concentrations (i.e. Cr ratio) and the Cramer-Rao Lower Bound (CRLB) is computed for each metabolite component

Part II.

Accelerated Magnetic Resonance Spectroscopic Imaging

3. Overdiscrete Spectroscopic Imaging with High-Resolution Corrections

In this chapter, a novel reconstruction method combined with accelerated acquisitions was developed to achieve fast MRSI of the brain with improved signal to noise ratio (SNR). The methodology included the development of a robust framework that minimized instabilities such as B_0 drift and patient motion. Moreover, the acquisition of a water reference scan, allowed to estimate and correct for physical disturbances avoiding the need for additional scans.

A manuscript of the present work has been published in the Journal of Magnetic Resonance in Medicine (MRM), entitled ”Overdiscrete Echo-Planar Spectroscopic Imaging with Correlated Higher-Order Phase Correction”. These results have been also presented at the 24th and 25th annual meetings of the International Society of Magnetic Resonance in Medicine (ISMRM) in the abstracts entitled ”Overdiscrete Reconstruction in Echo-Planar Spectroscopic Imaging with Auto-Calibrated B_0-Field Map Estimation” and ”High-Resolution Phase Correction in Overdiscrete Spectroscopic Imaging Reconstruction using Piecewise Polynomial Interpolation”, respectively.

3.1. Introduction

Magnetic Resonance Spectroscopic Imaging (MRSI) allows determining the spatial distribution of the metabolic components of brain tissue, which is of interest to a wide range

of clinical applications, especially for studying the central nervous system [80]. However, clinical MRSI scans suffer from low signal to noise ratio (SNR), limiting the minimum scan duration and maximum spatial resolution. Therefore, shorter acquisitions with higher SNR are desired to improve reproducibility, increase patient comfort, reduce motion artifacts, and minimize the instabilities in the MR system that take place during the examination and reduces the robustness of the technology.

The different acquisition elements that can affect the signal quality and introduce distortions can be classified into phase components and system instabilities. Phase-related distortions have different sources and generate specific effects in the MRSI signal. B_0-field inhomogeneity reduces the spectral resolution due to the intravoxel spectral shifts. Eddy currents [49] and system vibrations induce phase disturbances that can be especially harmful when residual water signal is strong, causing sidebands beyond the resonance frequency of water that hinder the detection of certain in specific spectral regions. Patient motion and B_0 drift [26], typically observed in long acquisitions are common instabilities that cause spatial distortions, affecting the reliability of the measurement.

Linear and high order shim coils allow to reduce the effects of spectral shifts and improve the linewidth of the metabolite peaks by minimizing the B_0 inhomogeneity [77, 17]. The correction of eddy currents and high order phase distortions is performed using a full water-unsuppressed scan and subtracting the phase of this reference scan from the water-suppressed metabolite signal [95, 69]. Nevertheless, an extra acquisition of the water signal is required, extending the acquisition duration, increasing energy deposition in the subject and for large matrix sizes, it could be unfeasible to acquire at the full resolution that the water-suppressed scan. Moreover, the reference scan is acquired at a different time during the examination potentially reducing the correlation of both datasets.

Short acquisitions reduce time-dependent system instabilities, as they allow to assume that the B_0-field and patient position remain stable during short time intervals. Short TR phase-encoded MRSI (PE MRSI) methods [78, 11, 35, 89] acquire large matrix sizes in a clinically feasible time. Although acceleration effectively reduces the overall acquisition time, this acquisition only samples one full k-space throughout the total scan duration.

This relies on the system being stable during the full exam duration. Parallel imaging methods [92, 32, 62, 48] retrieve undersampled scans using information from multi-element receiver coils. In MRSI, however, parallel imaging with large acceleration factors (R>4) is challenging. The inherent low resolution of MRSI makes the solution of the reconstruction problem ill-posed, mainly because of intravoxel variations in the sensitivity. This may cause incorrect signal unfolding and potential contamination from residual lipid signals.

To address the challenges of parallel imaging in MRSI, an overdiscrete reconstruction framework has been proposed [47, 46]. This method was successfully applied at 7T, improving spatial resolution via spatial response function optimization. Moreover, correcting for B_0-field variations effectively improved the spectral resolution and SNR. Yet, some methodological details remain challenging. First, the correlation of these datasets strongly depends on the stability of the measurement, because the water-suppressed MRSI, the water reference scan, and the B_0-field map are acquired separately and at different resolutions. Therefore, with long scans, the temporal and spatial correlation of the correction factors can be lost.

An alternative to achieve accelerated MRSI acquisitions is echo-planar spectroscopic imaging (EPSI) [86, 88, 79, 19, 117], which simultaneously encodes one spectral and one spatial dimension. This technique samples the full k-space with high acceleration, however, signal averaging is usually required to improve SNR. Moreover, rapid gradient switching of the EPSI trajectories leads to eddy currents and system vibrations that affect the measured signal.

This work describes a robust methodology for fast MRSI of the brain that combines EPSI acquisitions with the overdiscrete reconstruction. The method achieves improved stability via the simultaneous acquisition of a fully-correlated water reference scan at every phase encoding, allowing to dynamically correct for phase distortions. Furthermore, high-order phase correction is proposed as the generalization of the B_0 correction originally proposed. In a single correction step, phase distortions from B_0 inhomogeneity, eddy currents, B_0 drifts, and vibrations, are effectively corrected without requiring additional measurements. High SNR spectra were obtained with a simplified acquisition and reconstruction procedure.

3.2. Theory

3.2.1. Overdiscrete Reconstruction

The overdiscrete reconstruction [47, 46], consist in finding a reconstruction matrix F that solves the spatial reconstruction problem

$$\mathbf{p} = F\mathbf{m}, \tag{3.1}$$

where **p** corresponds to the reconstructed image and **m** corresponds to the measurements acquired with a multi channel receiver coil. F can be found by solving for each voxel the following optimization

$$\arg\min_{F} ||(FE - T)A||_2^2 + \alpha(F\Psi F^H) \tag{3.2}$$

where FE represents the spatial response function (SRF) of the measurement, Ψ corresponds to the noise covariance matrix and A is a spatial weighting factor.

In MRSI, the spectro-spatial data in the overdiscrete space can be reconstructed by applying the intermediate reconstruction operator F' to every temporal point of the k-t signal. The intermediate reconstruction operator is obtained by

$$F' = \Theta E^H (E\Theta E^H + \alpha\Psi)^+, \tag{3.3}$$

where E represents the encoding matrix, expressed at ζ^2-fold of the nominal resolution, Ψ corresponds the noise covariance matrix, Θ is a spatial weighting factor where $\Theta = AA^H$, and $^+$ denotes the pseudo-inverse. The regularization parameter α controls the noise optimization (Figure 3.1).

In the obtained dataset that is discretized at a higher resolution, spatial distortions that vary smoothly (e.g. the B_0 field inhomogeneity) can be corrected. Finally, an optimized SRF function, typically a Gaussian function, is chosen to return the data to the nominal resolution by applying the Target matrix T. This last step benefit for coherent signal averaging of the corrected subvoxel spectra (Figure 3.2).

The detailed algorithm for the implementation of the overdiscrete reconstruction with high-order phase correction is described in Table 3.1. Additionally, Figure 3.2 explain the

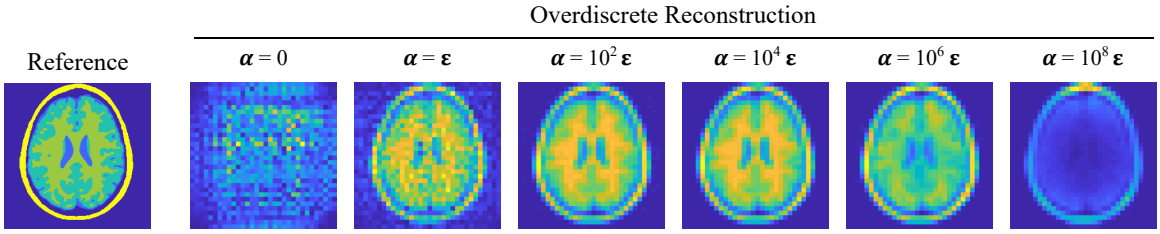

Figure 3.1.: Effect of noise regularization for different values of the parameter α. The parameter ε is computed from the data as $\varepsilon = mean(E\Theta E^H)/mean(\Psi)$. For the present work a regularization of $\alpha = 10^3 \cdot \varepsilon$ was chosen.

different elements of the overdiscrete reconstruction and their impact on the noise enhancement.

3.2.2. High-Order Phase Correction

The correction for signal dephasing due to B_0-field inhomogeneities is applied in an intermediate step, obtaining

$$h_{corr}(\mathbf{r}, t) = h(\mathbf{r}, t) \cdot e^{-i2\pi\Delta f_0(\mathbf{r})\cdot t}, \tag{3.4}$$

where $h(r, t)$ represents signal at the overdiscrete location r and time t, and $\Delta f_0(r)$ to the local frequency shift in Hz. The final corrected signal can be generalized to

$$h_{corr}(\mathbf{r}, t) = h(\mathbf{r}, t) \cdot e^{-i2\pi\varphi(\mathbf{r},t)}, \tag{3.5}$$

where the polynomial phase term $\varphi(\mathbf{r}, t)$ contains the zero-, first- and higher order spatial and temporal phase components. Estimation these phase distortions correspond allow to correct for off-resonance and eddy currents effects among other system instabilities.

3.2.3. Polynomial Phase Interpolation

The coefficients of the polynomial term are obtained from the simultaneously acquired water unsuppressed signal solving the weighted least squares problem

$$p = (A^T W^2 A)^{-1} A^T W^2 y \tag{3.6}$$

Table 1. Overdiscrete reconstruction algorithm with high-order phase correction

Requisites: Spatial registration of coil sensitivity maps (c_γ), MRSI water suppressed (m^{sup}) and water reference (m^{ref}) datasets.

1: Reconstruct m^{ref} spatially: → $s^{\mathrm{ref}}(\mathbf{r}_\pi, t) = cc\left(\mathcal{F}_{\mathbf{k}}\{\, m_\gamma^{\mathrm{ref}}(\mathbf{k}_\kappa, t)\,\}\right)$

2: Extract and unwrap phase from s^{ref}: → $\varphi\,(\mathbf{r}_\pi, t) = unwrap\left(\arg\left(s^{ref}(\mathbf{r}_\pi, t)\right)\right)$

3: Interpolate phase to the overdiscrete resolution: → $p_\varphi(\mathbf{r}_\rho, t) = \Gamma_{polynomial}(\,\varphi\,(\mathbf{r}_\pi, t)\,)$

4: Compute phase correction term: → $h_\varphi(\mathbf{r}_\rho, t) = \exp\left(-i \cdot p_\varphi\,(\mathbf{r}_\rho, t)\right)$

5: Build encoding matrix (E): → $\mathrm{E}_{(\gamma,\kappa),\rho} = c_\gamma(\mathbf{r}_\rho) \cdot \exp(-i\mathbf{k}_\kappa \mathbf{r}_\rho)$, where $\mathrm{E} \in \mathbb{C}^{(\mathrm{N}_\gamma \cdot \mathrm{N}_\kappa)\times \mathrm{N}_\rho}$

6: Build target Matrix (T): → $\mathrm{T}_{\pi,\rho} = SRF_\pi^{\mathrm{target}}(\mathbf{r}_\rho)$, where $\mathrm{T} \in \mathbb{C}^{\mathrm{N}_\pi \times \mathrm{N}_\rho}$

7: Compute noise matrix (Ψ): → $\Psi = \overline{\eta_\gamma \eta_\gamma^*}$, where $\Psi \in \mathbb{C}^{\mathrm{N}_\gamma \times \mathrm{N}_\gamma}$

8: Compute noise covariance matrix ($\widetilde{\Psi}$): → $\widetilde{\Psi} = \Psi \otimes I_{\mathrm{N}_\kappa}$, where $\widetilde{\Psi} \in \mathbb{C}^{(\mathrm{N}_\gamma \cdot \mathrm{N}_\kappa)\times(\mathrm{N}_\gamma \cdot \mathrm{N}_\kappa)}$

9: Compute spatial weight matrix (Θ): → $\Theta = \mathrm{A}\mathrm{A}^H$, where $\mathrm{A} \in \mathbb{C}^{\mathrm{N}_\pi \times \mathrm{N}_\rho}$

10: Compute reconstruction matrix (F′): → $\mathrm{F}' = \Theta\mathrm{E}^H\left(\mathrm{E}\Theta\mathrm{E}^H + \alpha\widetilde{\Psi}\right)^+$, where $\mathrm{F} \in \mathbb{C}^{\mathrm{N}_\rho \times (\mathrm{N}_\gamma \cdot \mathrm{N}_\kappa)}$

11: **for** every t in N_t

12: Compute intermediate image: → $\mathrm{s}'(\mathbf{r}_\rho, t) = \mathrm{F}' \cdot m^{\mathrm{sup}}(\mathbf{k}_\kappa, t)$

13: Apply phase correction term: → $s'_{\mathrm{corr}}(\mathbf{r}_\rho, t) = h_\varphi(\mathbf{r}_\rho, t) \circ s'(\mathbf{r}_\rho, t)$

14: Apply target matrix: → $s_{\mathrm{corr}}(\mathbf{r}_\pi, t) = \mathrm{T} \cdot s'_{\mathrm{corr}}(\mathbf{r}_\rho, t)$

15: **end for**

16: Compute Fourier transform along t → $s_{\mathrm{corr}}(\mathbf{r}_\pi, \omega) = \mathcal{F}_t\{s_{\mathrm{corr}}(\mathbf{r}_\pi, t)\}$

Definitions:

$\boldsymbol{r}$	Spatial dimension
$\boldsymbol{k}$	k-space dimension
t	Time dimension
ω	Frequency dimension
ζ	Overdiscrete factor
γ	Coil index
κ	k-space location index
π	Spatial location index at nominal resolution
ρ	Spatial location index at overdiscrete resolution
N_γ	Number of coils
N_t	Number of temporal points
N_κ	Number of k-space points
N_π	Number of spatial points at the nominal resolution ($\mathrm{N}_\pi = \mathrm{N}_\kappa$)
N_ρ	Number of spatial points at the overdiscrete resolution ($\zeta^2 \mathrm{N}_\pi$)
s'	Intermediate reconstructed image at the overdiscrete resolution
s'_{corr}	Phase-corrected intermediate reconstructed image
s_{corr}	Phase-corrected reconstructed image at the nominal resolution
p_φ	Polynomial fit of the unwrapped phase
c_φ	Phase correction term
η_γ	Noise of coil element γ
I	Identity matrix
α	Regularization parameter

Operators:

$\circ$	Element-wise multiplication
$\otimes$	Kronecker product
$*$	Complex conjugate
$^+$	Moore-Penrose pseudo inverse
^{H}	Matrix Hermitian
cc	Channel combination
Γ	Interpolation function
$\mathcal{F}$	Fourier Transform

Table 3.1.: Overdiscrete reconstruction algorithm with high-order phase correction.

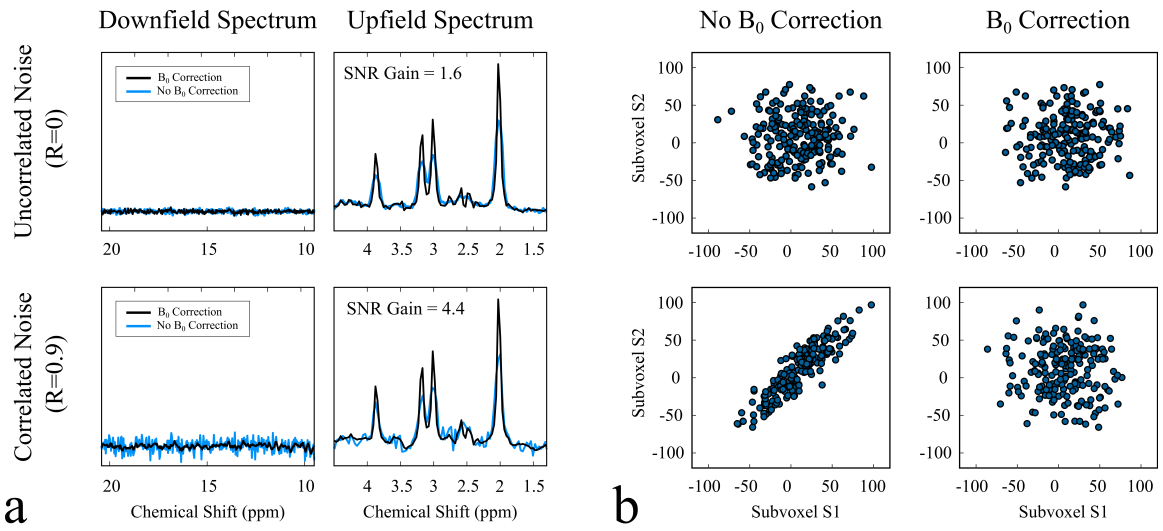

Figure 3.2.: Simulation of noise decorrelation by applying the B_0 correction. (a) Reconstructed spectrum with (black) and without (blue) B_0 correction for the case with uncorrelated noise (R=0) and highly correlated noise (R=0.9). Noticeable improvements in linewidth are observed for the up-field spectrum in both cases with an additional noise reduction in the case with high noise correlation. (b) Correlation between the spectral points of two subvoxels (S1 and S2) in the range from 10 to 20 ppm shown before and after B0 correction.

where y corresponds to the unwrapped phase of the measured water reference and W to the weight matrix extracted from the magnitude of the reference signal.

3.3. Methods

3.3.1. EPSI with Simultaneous Water Reference Acquisition

The proposed MRSI sequence (Figure 3.3) combines CHESS water suppression and PRESS spatial localization a flyback EPSI readout, which requires fewer repetitions to acquire a full k-space, thus reducing the scan time. Outer volume suppression (OVS) pulses are used prior to the excitation to destroy magnetization outside of the volume of interest. An effective repetition time involves the acquisition of two signals, namely the water-suppressed (W_{sup}) and the water reference (W_{ref}) data. The first excitation suppresses water using the CHESS

module and excites the selected volume with a 90°flip angle. In the second excitation, CHESS is disabled and a low flip angle α used to excite the sample and acquire a water reference. The low flip angle excitation let the metabolite components relax while acquiring sufficient water signal, thus avoiding extending the effective TR of the acquisition.
All the MR experiments in the present work were conducted on a GE 3T MR750w (GE Healthcare, Waukesha, WI, USA) using a 12 channel receive array with a volume transmit body coil (GE Healthcare, Waukesha, WI, USA). The gradient system used had the following a maximum gradient strength of 33 mTm^{-1} and a slew rate of 120 $\mathrm{T\,m}^{-1}\,\mathrm{s}^{-1}$ in each direction.

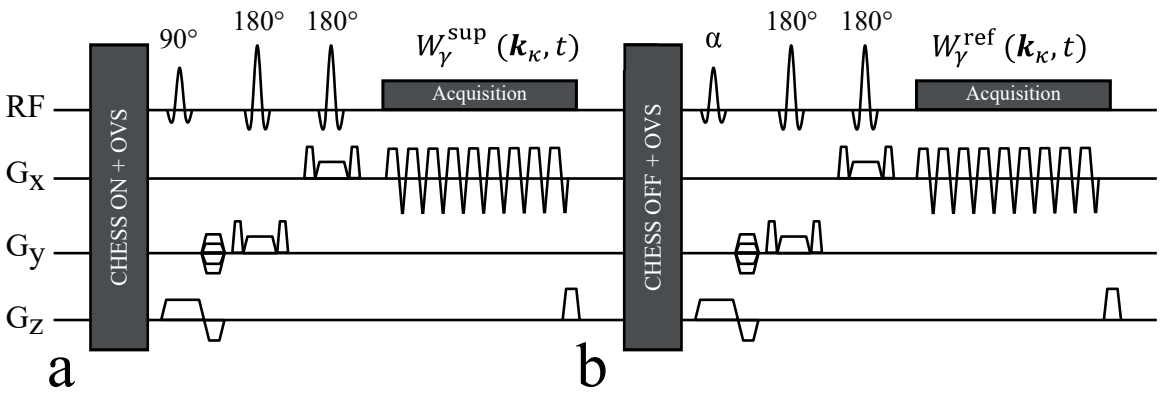

Figure 3.3.: Sequence diagram of the proposed acquisition which performs an interleaved acquisition of a water-unsuppressed reference scan in an effective TR of 1100 ms. First, (a) a water suppressed phase encode is acquired using CHESS and a 90° excitation pulse. Subsequently, (b) a low flip angle excitation without water suppression is performed to acquire the water reference.

3.3.2. Simulation Experiments

A simulation was implemented to show the different elements of the overdiscrete reconstruction and their effects in the spatial domain. This experiment was used to determine the optimal parameters for the algorithm. A high-resolution synthetic brain was created and the measurements using multi-element receiver coil were simulated (Figure 3.4. The

MRSI raw dataset was reconstructed using the following methods for comparison: (i) a Fourier transform at nominal resolution (FT Nominal), (ii) an FT at a higher resolution (FT Zero-Filled), and (iii) the overdiscrete reconstruction with different correction factors (Figure 3.2).

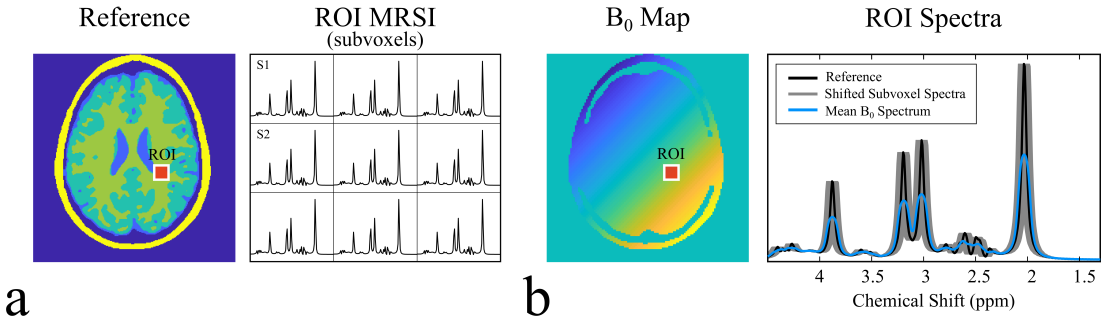

Figure 3.4.: Simulation of intravoxel spectra in the intermediate overdiscrete image. (a) Synthetic MRSI phantom and an ROI of simulated spectra representing the subvoxels in the intermediate overdiscrete reconstruction. (b) Simulated B_0 inhomogeneity (left) and the effect of the B_0 inhomogeneity in the subvoxel spectra (right).

3.3.3. Phantom Experiments

A 3D printed spherical phantom was built to validate MRSI measurements (Figure 3.5). The phantom was filled with distilled water and doped with gadolinium solution (Dotarem). Two 10 mL spheres (I and II) and a 60 mL sphere (III) made of glass were filled with metabolite solutions, containing myo-inositol (mI), choline (Cho), creatine (Cr) and N acetyl aspartate (NAA) with physiological concentration levels [91]. Cr and mI were mixed in a 1:1 ratio in all spheres with 10 mM concentration. NAA concentration was varied to approximately achieve a ratio to Cr of 1, 2, and 1.5 for spheres I, II, and III respectively (10-20 mM). Cho to Cr ratio was chosen from approximately 0.2, 0.3, and 0.4 for spheres I, II, and III respectively (2-4 mM). The ground truth for the metabolite concentrations in every sphere was determined from high SNR single voxel spectroscopy measurements and quantified using LCModel. The scans were obtained by localization of a $2\times2\times2$ cm^3

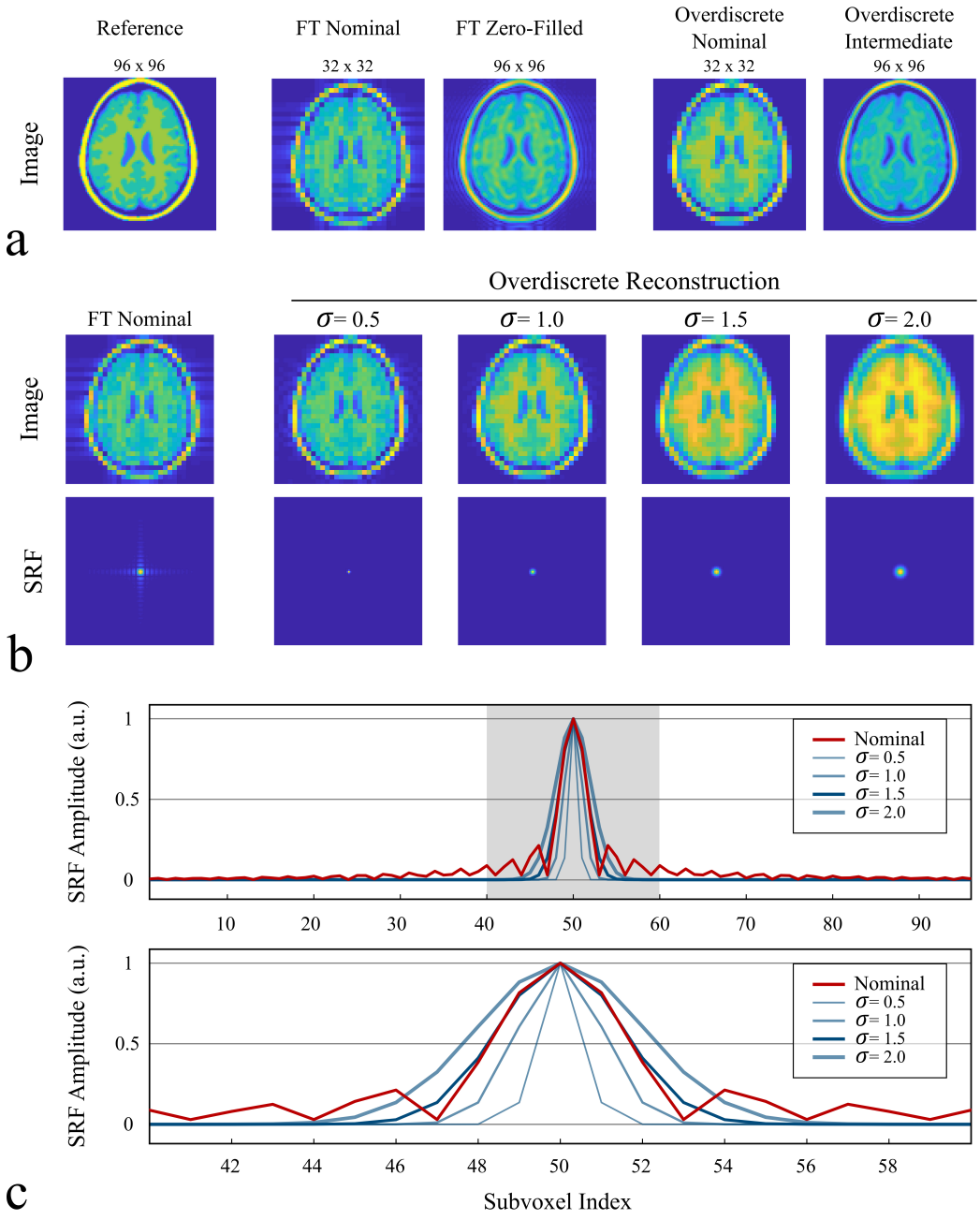

Table 3.2.: Simulation experiment showing the components of the overdiscrete reconstruction. (a) Spatial reconstruction showing the results of standard Fourier Transform (FT), zero-filled FT, the overdicrete at nominal resolution, and the intermediate high resolution overdiscrete image. (b) Effect of the SRF optimization in image domain using Gaussian functions with different σ values, which control the spatial resolution of the final image. (c) Plots of the SRF for different sigma values showing a reduction of the side-bands in the nominal resolution via SRF optimization

volume using PRESS, CHESS water suppression, TE/TR=35/1500 ms and 128 averages. MRSI EPSI scans were acquired for two different spatial resolutions by reducing the field of view (FOV) keeping the matrix size fixed.

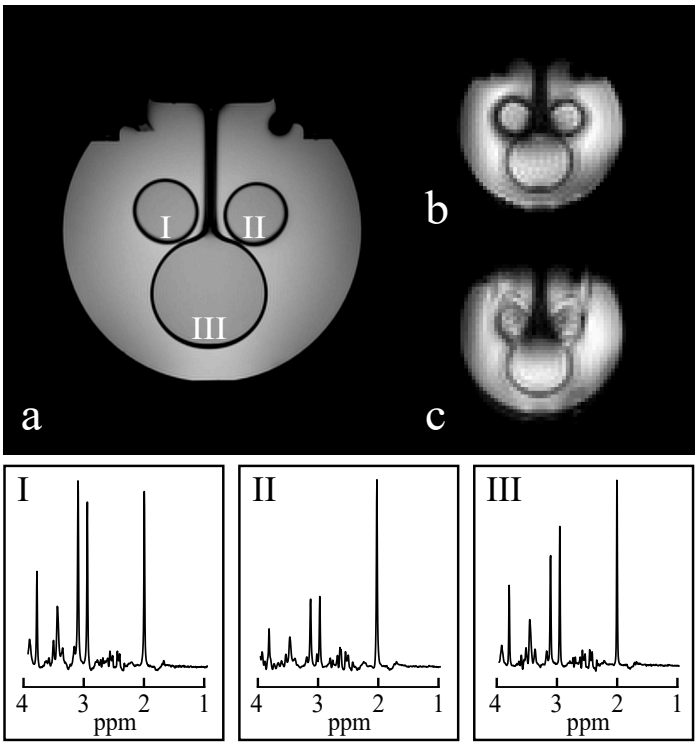

Figure 3.5.: Phantom designed for MRSI scans. (a) T2w image compared to a (b) maximum of the water signal acquired using EPSI and (c) maximum of the water signal acquired using PE MRSI with a 64×64 matrix size measured within 46 min. Noticeable spatial distortions can be observed due to instabilities in the system even in the absence of motion, caused mainly by B_0 drift.

3.3.4. In Vivo Experiments

Single slice MRSI measurements of four healthy volunteers (V1-V4) were acquired with the following protocol: (i) 16 average EPSI scan using the proposed acquisition sequence with an interleaved water reference scan acquired for every average, (ii) acquisition of sensitivity maps using a standard product sequence and (iii) reference B_0-field map measurement using a dual TE gradient echo sequence with TE1/TE2 = 10/12 ms. The acquisition settings

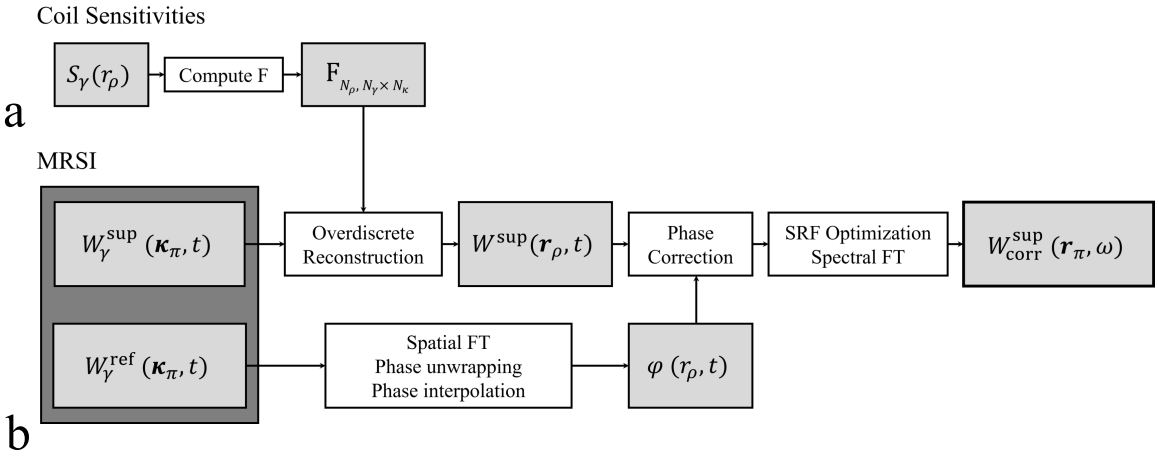

Figure 3.6.: Overdiscrete reconstruction pipeline with phase correction performed at high resolution. The framework only requires the acquisition of (a) coil sensitivities and (b) MRSI dataset with interleaved water reference.

for EPSI were the following: matrix size 24×24, FOV 24×24 cm^2, slice thickness 1.5 cm, TE/TR=35/1500 ms, and 34 seconds per average, i.e. a total scan duration of 8 minutes.

3.3.5. Reconstruction and Data Processing

The reconstruction pipeline showed in Figure 3.6 was used to process the EPSI datasets after reshaping the raw data into a k-t space. The intermediate reconstruction operator F was obtained from the measured sensitivity information (Fig. 3.6.a), no spatial weighting was used and uncorrelated noise was assumed. F was applied to each time point of the signal. The Spatial Fourier transform (FT) was computed followed by a channel combination as described in the theory section, zero-order phase subtraction, and temporal FT.

3.4. Results

3.4.1. Phase Estimation

The estimation of the phase correction term was evaluated for different orders of polynomials. The temporal (Fig. 3.7) and spatial fit (Fig. 3.8) are shown for the in vivo datasets at

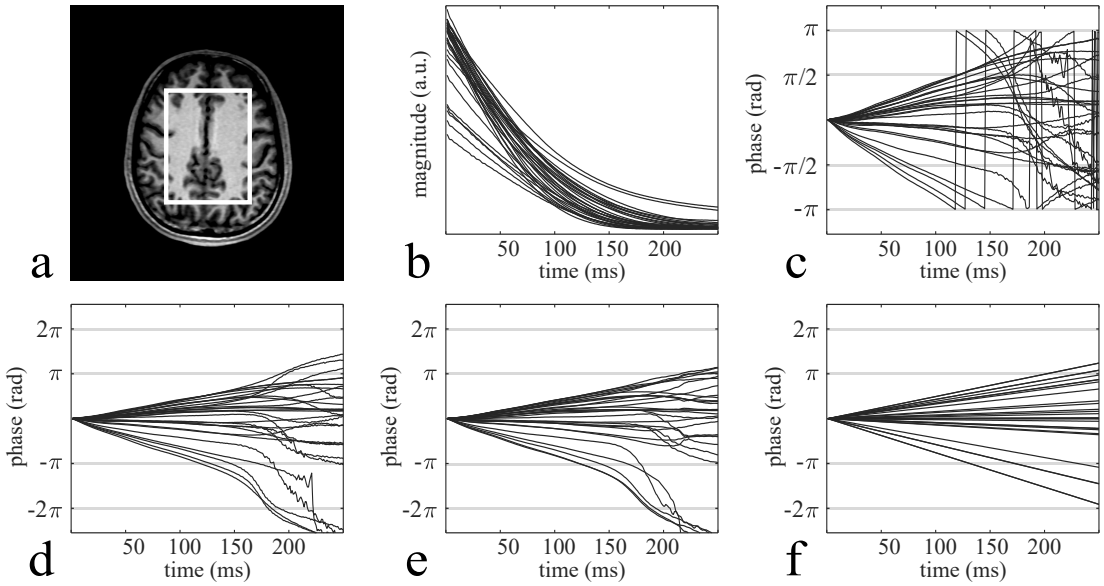

Figure 3.7.: (a) Prescribed PRESS volume, (b) magnitude and (c) phase of the temporal signals for all voxels inside the localized volume. A comparison is shown between the phase term (d) after phase unwrapping (e) after the fit using a polynomial basis and (f) the phase term corresponding to the B_0 correction term.

nominal and high resolution. Fitted third-order polynomials showed a negligible phase difference compared to the measured signal. Similarly, B_0-field inhomogeneity information was retrieved from the MRSI data by fitting a linear temporal function (Fig. 3.8b and 3.8c). The estimated map showed a good agreement with the measured B_0 map both visually and quantitatively, with a mean absolute difference of 3.54 Hz.

3.4.2. Phantom Quantification

A qualitative comparison between the standard processing pipeline and the proposed reconstruction method is shown in Figure 3.9 for all the compartments in the phantom. The spectra shown correspond to the sum of a $2.0\times2.0\times1.0$ cm^3 region inside each sphere.

In Figure 3.9 the spatial distribution of the measured MRSI phantom is shown. The SNR_{NAA} map was reconstructed to visualize the effect of the proposed reconstruction and compare it to ECC and spatial apodization. For each compartment in the MRSI

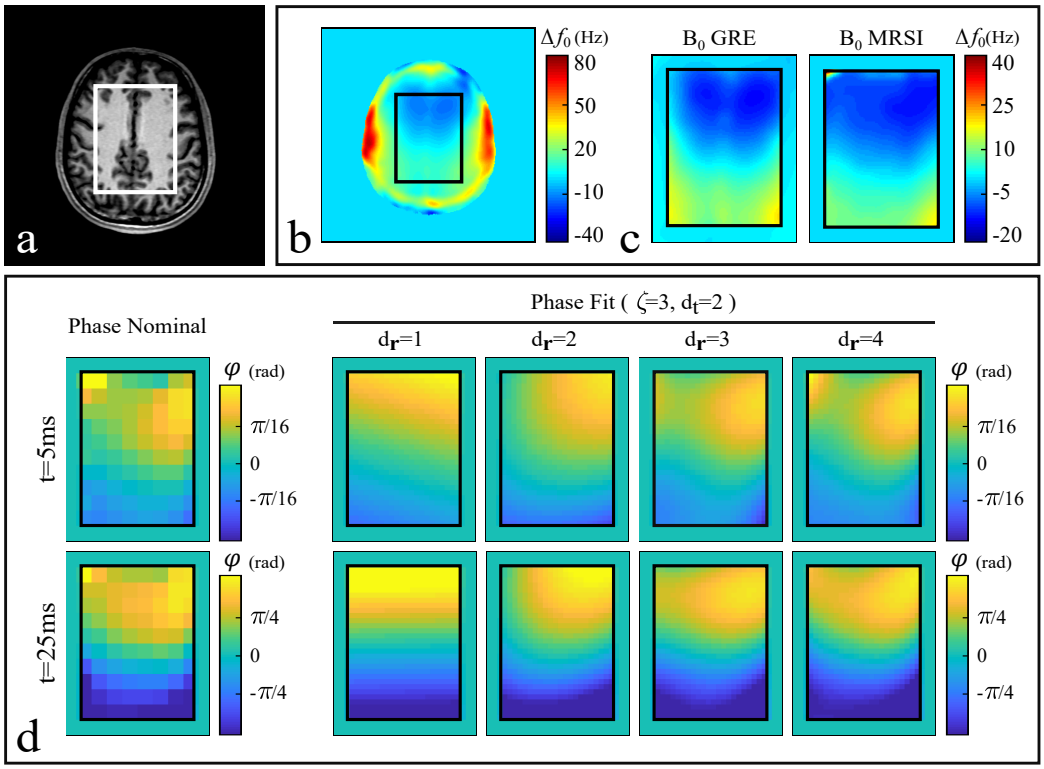

Figure 3.8.: Visualization of the spatial distribution of phase disturbances and estimation of the correction terms. (a) T1w image of the prescribed PRESS volume, (b) measured B_0 field map obtained with a dual gradient-echo acquisition, (c) comparison between the measured B_0 map within the localized volume and the B_0 estimated from the water reference acquisition, and (d) comparison between measured and fitted spatial phase term using increasing degrees of polynomials. Good agreement is shown with the advantage of a better correlation of the estimated terms.

phantom (I, II, and III), the SNR_{NAA} and SNR_{Cre} were plotted against the number of signal averages to assess the acceleration. Moreover, a quantitative analysis of the accuracy of the measurement is presented in Figure 3.9.d using the SNR_{NAA}/SNR_{Cre} ratio which is known for the compartments.

3.4.3. Higher-Order Phase Correction

Figure 3.10 shows the benefits of ECC and phase correction. The displayed spectra correspond to the mean and standard deviation (in blue) of all the voxels. The analysis of

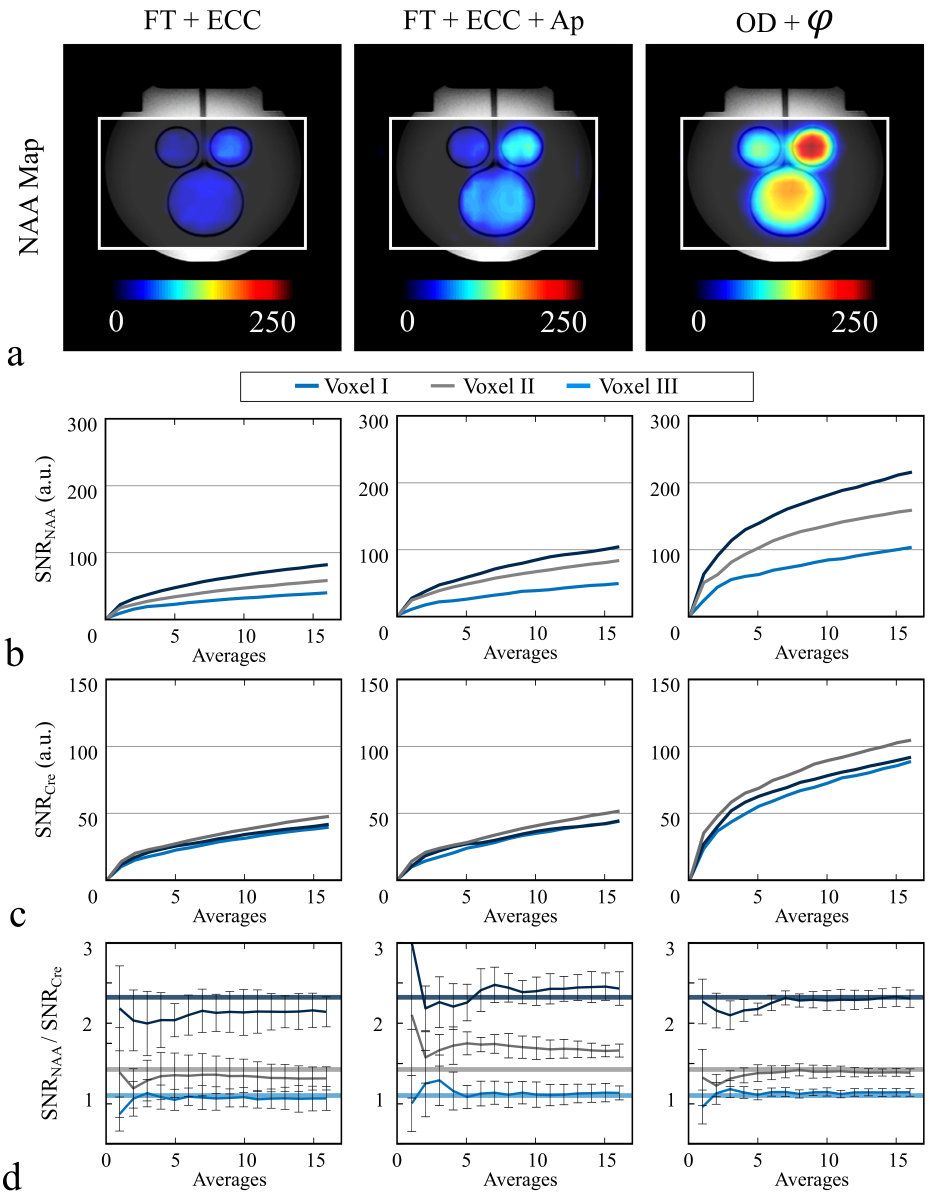

Figure 3.9.: Phantom MRSI experiments acquired with the proposed acquisition sequence. The datasets were reconstructed using standard FT with ECC, standard FT with ECC and spatial apodization (FT + ECC + Ap.) and the overdiscrete reconstruction with phase correction (OD + φ Corr.). (a) $\mathrm{SNR}_{\mathrm{NAA}}$ maps of the reconstructed MRSI datasets scaled to the same range. Mean (b) $\mathrm{SNR}_{\mathrm{NAA}}$ and (c) $\mathrm{SNR}_{\mathrm{Cre}}$ of each compartment plotted for the acquired signal averages. (d) Mean $\mathrm{SNR}_{\mathrm{NAA}}$ / $\mathrm{SNR}_{\mathrm{Cre}}$ and standard deviation of each compartment plotted for all signal averages. Ground truth value obtained with SVS is displayed for reference.

spectral data shows substantial improvements in line width and noise using the proposed overdiscrete reconstruction approach with phase correction achieves comparable results to the state of the art pipeline (B_0+ECC). The correction of phase distortion achieved a noticeable removal of spectral artifacts, observed in the region between 4.5 to 3.5 ppm where metabolites of interest can be found.

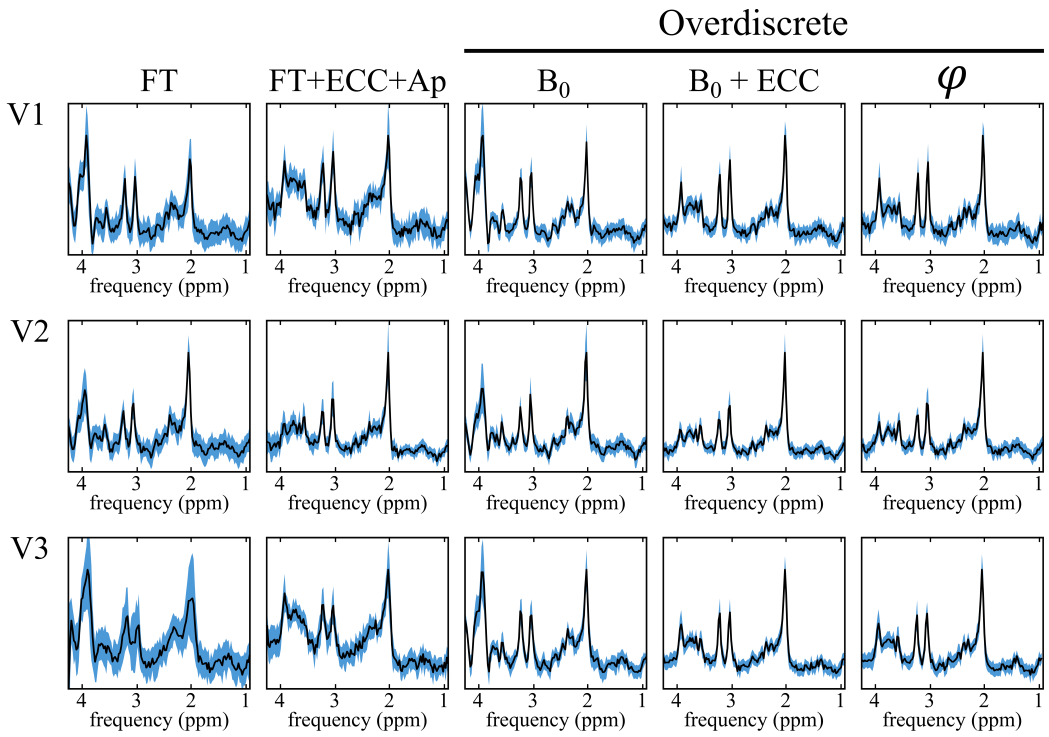

Figure 3.10.: Comparison of spectra obtained with standard FT and overdiscrete reconstruction. The mean spectrum of all voxels inside the volume selected with PRESS is presented and the standard deviation is displayed in blue. The effect of different correction steps is shown.

3.4.4. SNR Enhancement and Acceleration

A comparison between different correction approaches is presented in Figure 3.12 for all the measured volunteers (V1-V4). Improvements in spectral quality and SNR enhancement was evaluated qualitatively (3.12b) and quantitatively (3.12 c and d). For the quantitative

analysis, the mean SNR_{NAA} of all the voxels within the PRESS volume was analyzed. Substantial signal enhancement was achieved using the overdiscrete reconstruction with phase correction (OD + φ) and was comparable to the B_0 correction (OD + B_0). Moreover, no significant change in FWHM is observed while SNR increased with the proposed methodology.

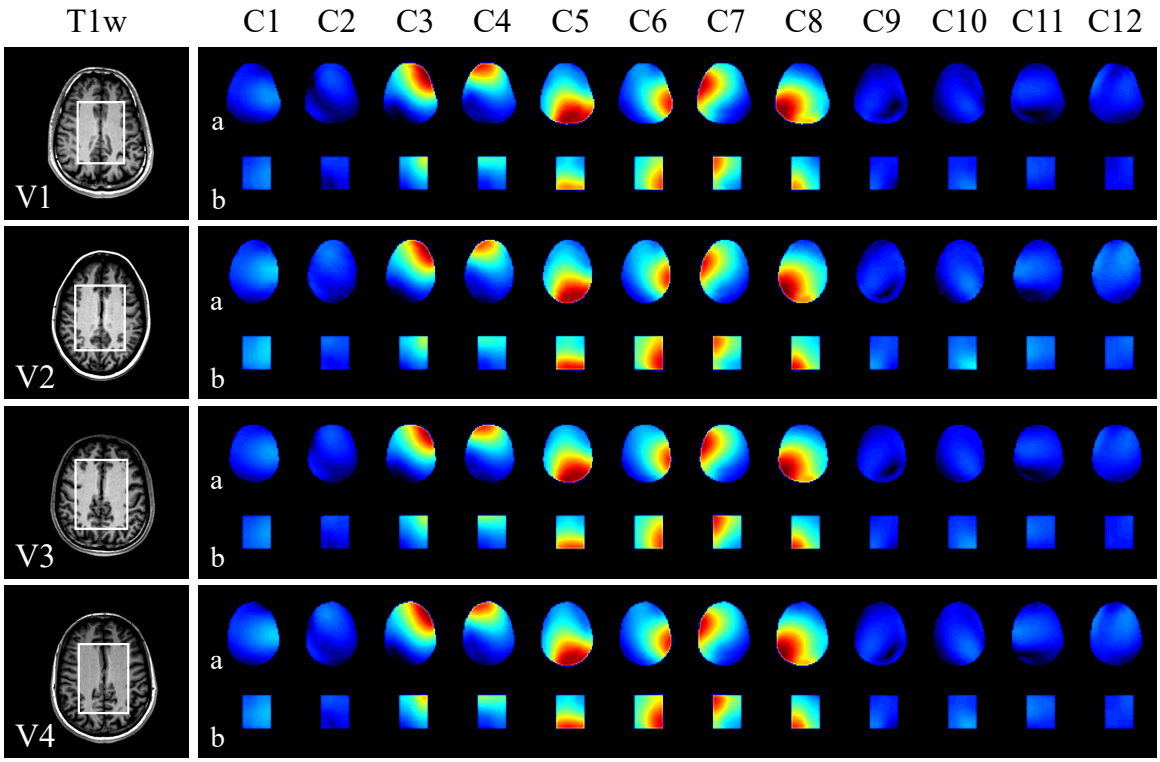

Figure 3.11.: Coil sensitivity maps (a) measured and (b) estimated from the water reference acquisition.

3.5. Discussion

The goal of the methodology described in this work is to achieve robust MRSI scans with high SNR and minimal instability effects such as B_0 drifts, patient motion, and eddy currents. EPSI acquisition sequence with interleaved water referencing measures a full slice in 36 seconds. In this interval, it is feasible to assume that the system is stable. Moreover, the correlation of the correction terms is maximized for every slice acquired. This approach

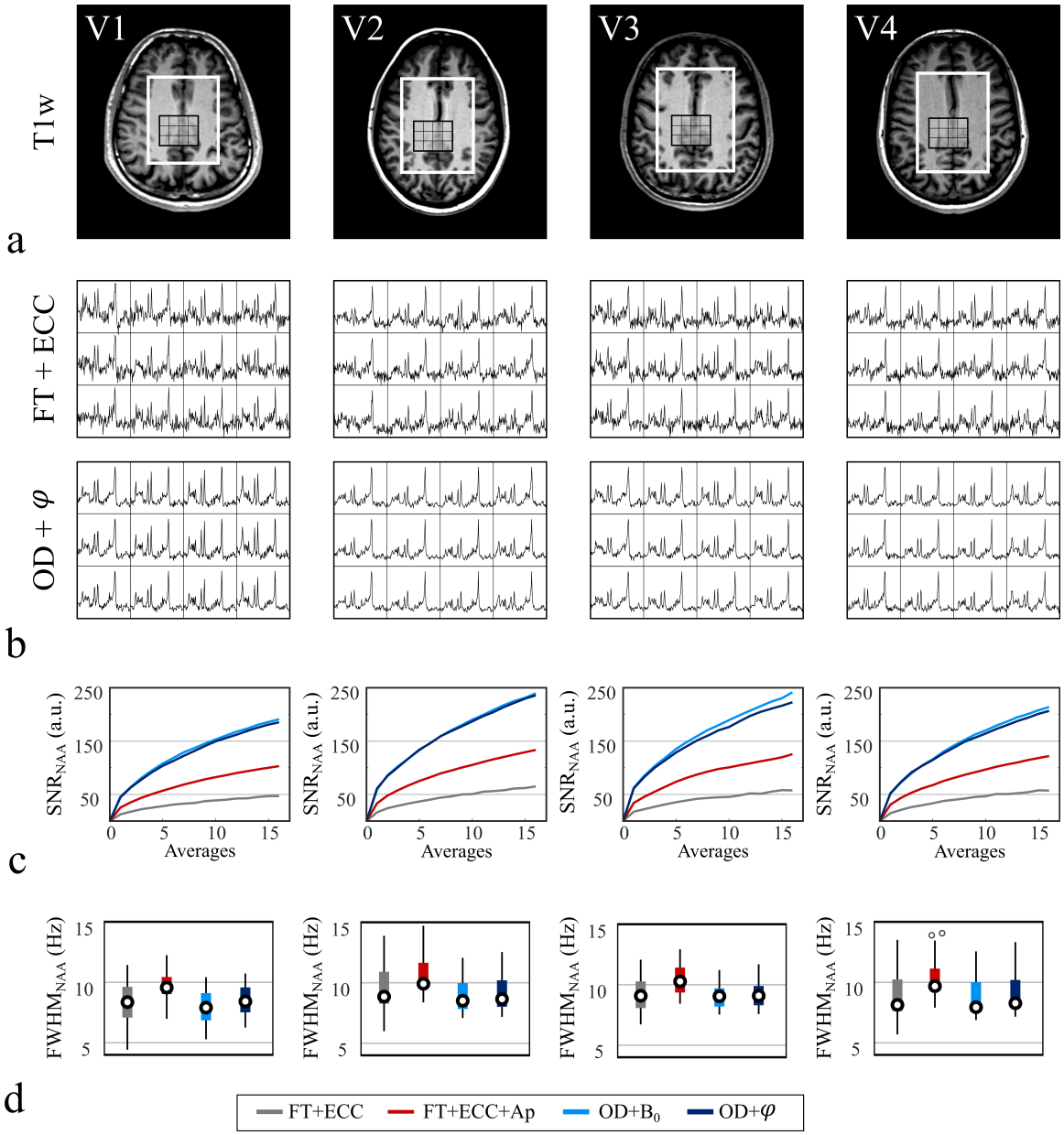

Figure 3.12.: In vivo MRSI datasets of the measured volunteers (V1-V4). (a) T1w anatomical images showing the location of the PRESS volume and an ROI (3×4 voxels). (b) The spectra in the ROI are shown for the FT reconstruction with ECC and the proposed overdiscrete reconstruction with phase correction (OD + φ Corr.). (c) Mean SNR_{NAA} computed for all voxels in the volume selected with PRESS and (d) $FWHM_{NAA}$ for the datasets with 16 averages between the different reconstructions and corrections schemes is shown. No significant change in FWHM is observed while SNR increased with the proposed methodology.

could also enable motion estimation and correction avoiding reacquiring the full dataset after in the presence of patient motion.

The flyback EPSI trajectory was optimized to encode the k-t space with an in-plane resolution of 10×10 mm^2 with a bandwidth of 1200 Hz in a single interleave (max. gradient strength 33 mTm^{-1}, slew rate 120 T m^{-1} s^{-1}). Higher spatial resolutions and higher bandwidth could be achieved by interleaved EPSI acquisitions at the cost of additional excitations. Alternatively, symmetric EPSI acquisitions [117], which are less gradient intense, can equally benefit from overdiscrete reconstruction and interleaved water referencing.

The proposed sequence acquires a fully correlated water reference for every EPSI readout without increasing the scan duration. This allows extracting phase distortions from the water reference and corrects them in the water-suppressed scans. Moreover, by performing a piecewise polynomial fit, an overdiscrete phase correction term can be obtained. This achieves comparable results to B_0 correction with a more general and simplified methodology.

In EPSI acquisitions, signal averaging is commonly used to obtain enough signal quality for reliable metabolite quantification. SNR enhancement obtained with the overdiscrete reconstruction reduced the number of signal averages required for this purpose. The equivalent acceleration factor of this approach was R=6–8 with an SNR gain of 2.3. This allows taking full advantage of the acceleration provided by EPSI readouts. Moreover, artifacts and inconsistencies in the direction of the readout gradients were eliminated with the proposed phase correction.

Through polynomial interpolation eddy currents and complex measurement disturbances that have hard to model temporal and spatial distributions can be adaptively estimated and corrected. If all this phase effects occur smoothly in the r-t space. It has been reported that eddy currents occur can be modeled with different time intervals as the residual. The degree of temporal polynomials and the temporal window size showed no significant effect in the phase residual. Nevertheless, this ensured smoothness of the fit and avoid discontinuities that could potentially appear in noisy datasets. Low degree polynomials and a reduced temporal window were chosen for the temporal basis to ensure correspondence to the

phase measured. At higher field strengths, spatial variations of the B_0-field might require higher-order spatial polynomials to reliably correct for this effect.

3.6. Limitations

A limitation of this methodology is the computational cost that the computation of the reconstruction operator has. This is achieved by the inversion of the encoding matrix E which size scales with the over discretization factor ζ^2 and the number of coil elements. Therefore, for large MRSI matrix sizes, the implementation of the reconstruction problem needs to be done iteratively at the cost of computation time. Additionally, during the measurement of the coil sensitivity profiles, a potential misalignment with the MRSI dataset could result in a suboptimal reconstruction. Finally, the gain in SNR would allow increasing the resolution of the acquisition. However, for high-resolution spatial encoding, the limit of the gradient performance might be reached, requiring interleaved EPSI acquisitions that could increase the complexity of the reconstruction and introduce undesired effects.

4. High-Resolution Echo-Planar Spectroscopic Imaging at Ultra-High Field

MR spectroscopic imaging (MRSI) at ultra-high field allows for the detection of low-concentration metabolites in the brain, thanks to the improved sensitivity. Nevertheless, optimized acquisition techniques are still required to address specific limitations of MRSI at ultra-high field. In this chapter, a methodology to achieve fast ^{1}H MRSI at 7T is detailed. The proposed acquisition sequence combines semi-localized by adiabatic selective refocusing (semi-LASER) for localization, symmetric echo-planar spectroscopic imaging (EPSI) for fast spatial encoding at high bandwidth, and an improved water suppression with variable power and optimized relaxation delays (VAPOR). Furthermore, the correction of phase inconsistencies in the symmetric EPSI trajectory enabled MRSI measurements at 7T with high-bandwidth.

The content of this work has been published in the Journal of NMR in Biomedicine under the title ”High-Resolution Echo-Planar Spectroscopic Imaging at Ultra-High Field”.

4.1. Introduction

Proton MR Spectroscopic Imaging (^{1}H MRSI) at ultra-high field (>7T) allows the detection of low concentration metabolites in the brain with a larger chemical shift dispersion and improved signal to noise ratio (SNR). However, challenges need to be addressed to obtain

the theoretical signal improvements at high field strengths. The presence of strong B_0 and B_1^+ inhomogeneities degrades signal quality and spectral resolution. Long repetition times (TR) are often required due to specific absorption rate (SAR) limitations, extending the acquisition duration. Moreover, nuisance signal contributions from water and lipids introduce artifacts that hinder the reliable quantification of metabolites.

Acquisition methods based on free induction decay (FID) have been proposed for ultra-high field MRSI. In these experiments, lipid contamination from the skull is reduced by either acquiring large matrix sizes at short TR, thus improving the point-spread function [11, 35, 89, 78], or using outer volume suppression (OVS) RF pulses around the volume of interest (VOI) [37].

Alternatively, techniques based on volume localization, such as point-resolved spectroscopy (PRESS) [13] and stimulated echo acquisition mode (STEAM) [28] remove the lipid signals originated from the skull by selectively exciting a VOI within the brain. However, the relatively low bandwidth of the excitation and refocusing pulses in the PRESS sequences causes chemical shift displacement errors (CSDE), which are proportional to the field strength [4]. The inaccurate volume selection can potentially introduce unwanted signals from the skull into the measurements. On the other hand, STEAM is less affected by CSDE but achieves only half of the SNR of PRESS. Semi-localization by adiabatic selective refocusing (semi-LASER) [102, 101] uses adiabatic refocusing pulses to effectively reduce the CSDE in-plane enabling precise volume localization at higher fields. Nevertheless, the main drawback of semi LASER is the high SAR introduced, which limits the minimum TR of the sequence. Therefore, the matrix size that can be acquired within a clinically feasible time is restricted, especially in standard phase-encoded MRSI (PE MRSI).

Echo planar spectroscopic imaging (EPSI) [86, 88, 79], is a fast encoding technique capable of encoding one spatial and one spectral dimension in a single TR, as a result, speed is achieved at the cost of SNR. An implementation of this encoding technique is flyback EPSI [19], which is relatively insensitive to timing errors and requires a simple reconstruction process. However, a high gradient performance is needed, limiting the maximum spatial resolution and spectral bandwidth. Moreover, as the signal is not sampled during the

flyback portion of the trajectory its encoding efficiency is substantially reduced. Although interleaved trajectories may overcome these limitations, they require a longer acquisition time and complex processing to avoid aliasing and artifacts.

The SNR efficiency of EPSI could be improved using a symmetric EPSI readout [117]. However, symmetric EPSI presents a miss-match between even and odd lines of the k-t space causing spectral ghosting. To avoid these artifacts, the even and odd lines can be processed separately, with the downside of reducing the effective spectral bandwidth by a factor of two and potentially exceeding the gradient performance needed at high field strengths. The interlaced Fourier transform [72] has been proposed to jointly reconstruct even and odd echoes without sacrificing spectral bandwidth but requiring calibration of the k-space trajectory to correct for eddy current effects and get robust results. Similarly, a postprocessing approach using echo shifts and zero-order phase correction to remove inconsistencies was introduced and demonstrated for EPSI scans of water and fat resonances [1]. In recent approaches, the spectral bandwidth was substantially increased using phase and time shifts at 3T [59] and with a dual readout EPSI at 7T [3]. Conversely, the correction of ghost artifacts in the phase-encode dimension is routinely performed in echo-planar imaging (EPI) [39, 30]. The method consists of estimating constant and linear phase correction terms from a reference scan measured without phase encoding gradients and applying these terms to each phase encoding, i.e. line of k-space.

Water suppression is also necessary to avoid artifacts, baseline distortions, and to reliably quantify metabolites. An effective method based on variable power and optimized relaxation delays (VAPOR) [110], initially implemented in single voxel spectroscopy scans at ultra-high field [81], has been proposed as an alternative to chemical shift selective saturation (CHESS) suppression [34]. VAPOR achieves a reduction in the water signal to the order of magnitude of the metabolites, allowing consistent detection of metabolites close to the water resonance.

This work presents a framework for high-resolution ^{1}H MRSI that enables fast acquisitions with high spectral quality at 7T. The method significantly reduces the acquisition time by implementing a high-bandwidth symmetric EPSI readout in combination with

semi-LASER localization and VAPOR water suppression. Furthermore, an effective phase correction for symmetric EPSI using a single shot water reference scan is introduced to remove spectral ghosting.

4.2. Theory

4.2.1. Phase Correction for Symmetric EPSI

Inconsistencies between even and odd lines in the EPSI trajectory were corrected by adapting the method that has been described for k-space alignment in EPI [117]. The phase correction (PC) term for the k-t space was estimated from a water reference scan measured with the same acquisition settings but without phase encoding gradients.

First, the reference signal S_{ref} was interpolated into k-t space and the phase difference φ_{diff} between adjacent temporal points was calculated using the following equation

$$\varphi^t_{\text{diff}}(\boldsymbol{k}) = \arg[S^t_{\text{ref}}(\boldsymbol{k}) \cdot S^{t+1}_{\text{ref}}(\boldsymbol{k})^*], \tag{4.1}$$

where t represents the temporal location, $\boldsymbol{k}$ the k-space location in the EPSI direction and * denotes the complex conjugate of the signal. Then, a weighted least-squares first-order fit was performed to retrieve the phase correction term

$$\varphi^t_{\text{corr}}(\boldsymbol{k}) = \mathrm{a}_t \cdot \boldsymbol{k} + \mathrm{b}_t \approx \varphi^t_{\text{diff}}(\boldsymbol{k}), \tag{4.2}$$

where a_t and b_t correspond to the linear and constant phase correction coefficients. Finally, the term was applied to each phase encode and channel of the water-suppressed signal S_{sup}

$$S^t_{\text{corr}}(\boldsymbol{k}) = S^t_{\text{sup}}(\boldsymbol{k}) \cdot \exp(-i \cdot \varphi^t_{\text{corr}}(\boldsymbol{k})). \tag{4.3}$$

For validation, the estimated term can be applied to the water reference to visualize the effect of the alignment (Fig. 4.3 c and d). Alternatively, an eddy current correction (ECC) can be performed using a fully-encoded water reference [3]. This method extracts the phase of the reference scan and subtracts it directly from the water suppressed signal. The subtracted

term is assumed to contain all phase effects that are specific to the acquisition e.g., eddy currents, B_0 inhomogeneity, vibrations and gradient imperfections.

4.2.2. Multi-Channel Signal Combination

In the absence of sensitivity information, the signal of multi-element receiver coils can be combined by phasing the signal of each coil element and adding the signal coherently using weights from the maximum averaged magnitude [99, 94]. Given the time-domain signal $y_\gamma(t, \mathbf{r})$ at voxel position r measured with the γ-th coil element, singular value decomposition (SVD) is computed for the maximum temporal signal at each voxel position $\mathbf{r}$, obtaining $\mathbf{Y} = \mathbf{U\Sigma V}^*$. The weight w_γ for each coil element is then estimated from the normalized singular vector in V corresponding to the largest singular value

$$w_\gamma(\mathbf{r}) = \frac{\mathbf{v}^*_{\gamma,\sigma_\mathbf{1}}}{\sum_\gamma \mid \mathbf{v}^*_{\gamma,\sigma_\mathbf{1}} \mid}, \tag{4.4}$$

where * denotes the complex conjugate and σ_1 the largest singular value. The term $w_\gamma(\mathbf{r})$ contains the relative phase and scaling information for each coil. Finally, the combined temporal signal $S(t, \mathbf{r})$ at voxel position $\mathbf{r}$ is obtained as follows

$$S(t, \mathbf{r}) = \sum_\gamma w_\gamma(\mathbf{r}) \cdot y_\gamma(t, \mathbf{r}). \tag{4.5}$$

4.3. Methods

4.3.1. Localized Symmetric EPSI using Semi-LASER

The proposed MRSI sequence (Fig. 4.1) combines VAPOR water suppression and semi-LASER spatial localization with a ramp-sampled symmetric EPSI readout, which requires fewer repetitions to acquire a full k-space, thus reducing the scan time and keeping the total acquisition within the SAR limits. GOIA WURST adiabatic full passage (AFP) RF pulses were used with a duration 4.5 ms, a bandwidth of 10 kHz, 16th order hyperbolic secant (HS) modulation (B_1) and a 4th order gradient modulation [4, 21]. For the slice-selective excitation, an asymmetric sinc pulse was used with a duration of 4.2 ms and a bandwidth

of 3.7 kHz. GOIA-WURST pulses were selected as they have exhibited robust performance with reduced CSDE and a substantial reduction of SAR per excitation, high SNR, and a better volume selection profile.

4.3.2. In Vivo Experiments

MR experiments were conducted on a GE 7T MR950 scanner using a 32 channel receive coil with a volume transmit head coil (NOVA Medical, Wilmington, MA, USA) and a GE 3T MR750w (GE Healthcare, Waukesha, WI, USA) using a 12 channel receive array with a volume transmit body coil (GE Healthcare, Waukesha, WI, USA). The gradient system present at 7T had a maximum gradient strength of 50 mTm^{-1} and a slew rate of 200 $Tm^{-1}s^{-1}$ in each direction. The 3T scanner had a gradient system with a maximum gradient strength of 33 mTm^{-1} and a slew rate of 120 $Tm^{-1}s^{-1}$ in each direction.

Anatomical imaging at 7T consisted of a 3D T1 weighted (T1w) inversion recovery-prepared spoiled gradient echo (IR SPGR) acquisition with the following parameters: TR=3.9 ms, TE=1.8 ms, TI=1350 ms, matrix size 256×256×176 and field of view (FOV) 256×256×176 mm^3. At 3T same sequence was used with the following parameters: TR=7.4 ms, TE=2.1 ms, TI=400 ms, matrix size 256×256×200 and field of view (FOV) 240×240×320 mm^3.

Single slice MRSI measurements of three healthy volunteers were acquired at 7T (^{7T}V1–^{7T}V3) with a 6-minute protocol that included: (i) a water suppressed semi-LASER EPSI scan with four averages and a total duration of 4.8 minutes; (ii) a 3-second water unsuppressed semi-LASER EPSI reference scan with the same sequence parameters but no phase encoding gradients, required for PC; and (iii) a 1.2 minute fully encoded water reference, required for ECC. Prior to the MRSI acquisition, power calibration of VAPOR was performed for each subject to improve water suppression. The following parameters were used: TR/TE=3000/35 ms, matrix size 24×24, FOV 12×12 cm^2, slice thickness 15 mm (^{7T}V1 and ^{7T}V2) and 10 mm (^{7T}V3), spectral points 512, spectral bandwidth 2500 Hz and anterior-posterior (AP) direction for the EPSI readout gradient.

Three additional healthy volunteers (^{3T}V1–^{3T}V3) were measured at 3T with a shorter

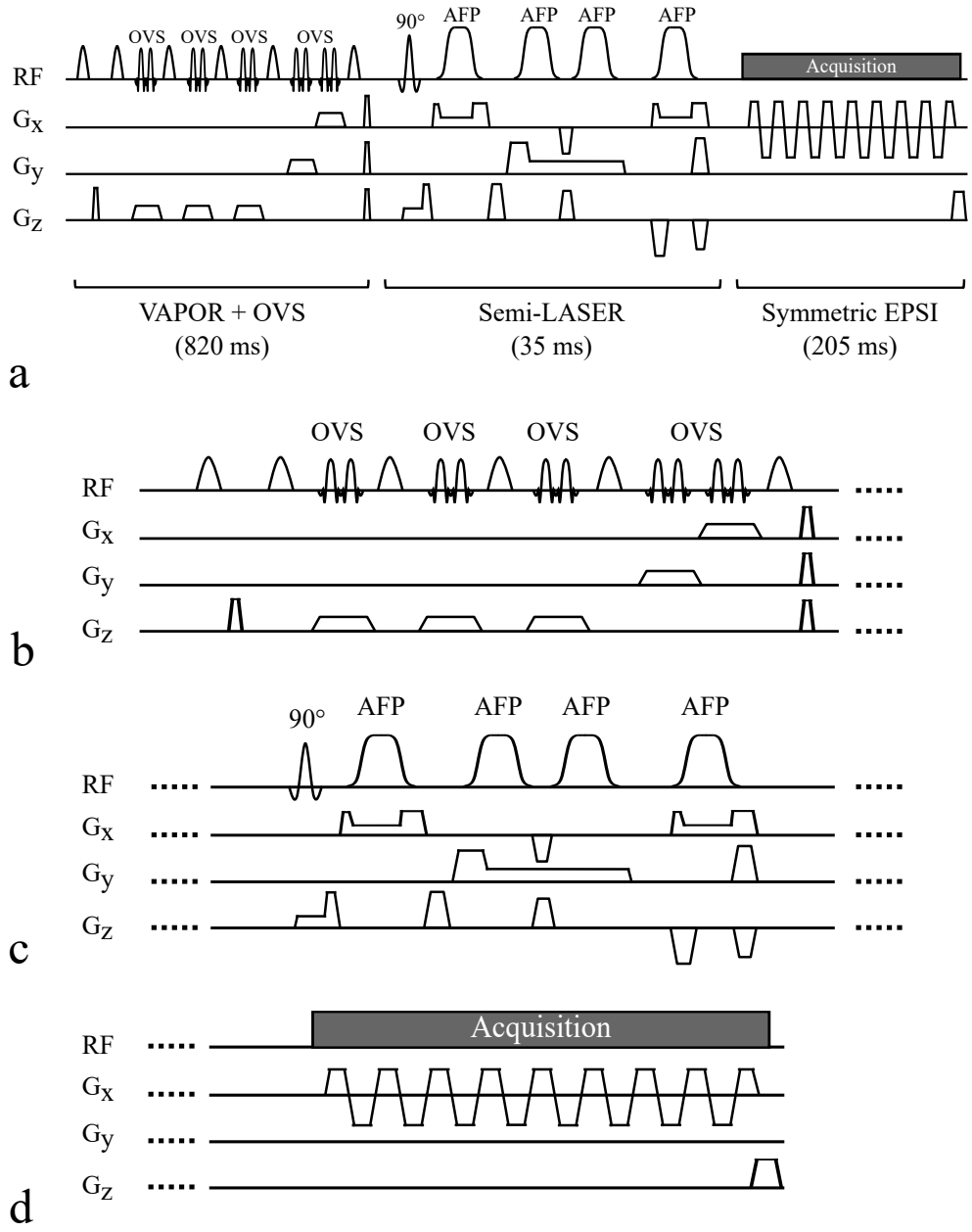

Figure 4.1.: (a) Pulse sequence diagram used for the high-resolution MRSI protocol. The sequence consists of (b) VAPOR water suppression interleaved with outer-volume suppression (OVS) pulses, followed by (c) semi-LASER localization using GOIA WURST adiabatic full passage (AFP) refocusing pulses and (d) ramp-sampled symmetric EPSI readout.

TR of 1500 ms, reducing the total acquisition time of the MRSI protocol (i, ii and iii) to 3 minutes. The slice thickness was 15 mm, the spectral bandwidth 1200 Hz, and TE=35 ms for all cases. At 3T, a lower resolution (1.5 mL), obtained by increasing the FOV to 24×24 cm^2, was chosen to achieve enough spectral quality needed for a reliable metabolite quantification, allowing a consistent comparison to 7T scans.

For comparison, PE MRSI measurements were also acquired at 3T for the same subjects (^{3T}V1–^{3T}V3) using the identical settings. To shorten the acquisition time of PE MRSI, the matrix size was reduced to 20×20, the FOV to 20×20 cm^2 and elliptical k-space sampling was selected, thus retaining the same volume size (1.5 mL) as in EPSI acquisition. Table 1 shows a list of the volunteer scans measured with different field strengths and voxel sizes.

Dataset	FOV (mm^2)	Voxel size (mm^3)	Volume (ml)	Acq. Time (min)	[a] Mean SNR_{peak}	Mean $SNR_{V,t}$	[b]Mean FWHM (Hz)
EPSI							
^{7T}V1	120×120	5×5×15	0.375	5	13.9 ± 1.7	16.6± 2.0	21.5 ±3.26
^{7T}V2	120×120	5×5×15	0.375	5	16.2 ± 2.6	19.3± 3.1	20.2 ±3.16
^{7T}V3	120×120	5×5×10	0.25	5	11.6 ± 1.5	20.7± 2.8	18.8 ±3.01
^{3T}V1	240×240	10×10×15	1.5	2.5	27.1 ± 3.3	11.4± 1.4	14.9 ±1.24
^{3T}V2	240×240	10×10×15	1.5	2.5	26.3 ± 4.4	11.1± 1.9	15.0 ±1.81
^{3T}V3	240×240	10×10×15	1.5	2.5	32.1 ± 3.8	13.5± 1.6	14.6 ±1.23
PE-MRSI							
^{3T}V1	200×200	10×10×15	1.5	8	47.4 ±5.3	11.2 ±1.2	13.9 ±0.51
^{3T}V2	200×200	10×10×15	1.5	8	48.2 ±12	11.4 ±2.8	20.5 ±12.8
^{3T}V3	200×200	10×10×15	1.5	8	77.0±5.1	18.1±1.2	15.2±1.91

Table 4.1.: List of volunteer scans measured with the presented methodology and comparison of SNR and FWHM for different voxel sizes and field strengths.
[a]Mean estimated SNR_{peak} (a.u.) of the NAA singlet at 2.01 ppm. Calculated as the maximum amplitude of the real-valued metabolite peak, divided by the standard deviation of the noise computed for all voxels in the range from 6.0 to 8.0 ppm.
[b]Mean FWHM of the NAA singlet at 2.01 ppm.

4.3.3. Reconstruction and Data Processing

The symmetric EPSI data were reshaped and interpolated into k-t space. Even lines, corresponding to the negative lobes of the trajectory, were reversed and an 8-Hz Gaussian temporal apodization was applied. Subsequently, PC was performed as described in the previous section using the Orchestra reconstruction toolbox (GE Healthcare) to perform the least-squares fit in Eq. 2. For comparison, ECC was applied to the data using the fully encoded water reference scan. Spatial FT was computed followed by a channel combination, residual water removal using Hankel singular value decomposition (HSVD) [8], zero-order phase subtraction at each voxel and temporal FT.

The percentage of aliasing was quantified using the ratio between the integral of the aliased and the real NAA singlet at 2.01 ppm. The aliased NAA peak is found displaced by half bandwidth from the 2.01 ppm location. The SNR per unit volume and unit time ($\mathrm{SNR_{V,t}}$) [79] was also computed to compare signal quality between the acquired datasets with different resolution and duration. The $\mathrm{SNR_{V,t}}$ is defined as follows

$$\mathrm{SNR_{V,t}} = \frac{\mathrm{SNR_{peak}}}{V \cdot \sqrt{t_{\mathrm{acq}}}}, \tag{4.6}$$

where V corresponds to the voxel size (cm^3), t_{acq} to the acquisition time (min), and $\mathrm{SNR_{peak}}$ represents the ratio between the peak amplitude of the metabolite of interest, namely the main NAA singlet at 2.01 ppm, and the standard deviation of the noise computed for all voxels in the range from 6.0 to 8.0 ppm. Additionally, the full width at half maximum (FWHM) was calculated from the local maximum around 2.01 ppm using Matlab (MathWorks, Natick, MA, USA). The analysis included all the voxels within the semi-LASER volume in the scans at 3T and in a region of equivalent size in the scans at 7T. This allowed having comparable shim variations between both field strengths.

4.3.4. Spectral Quantification

The reconstructed spectra were quantified with LCModel [91] using a basis set consisting of 19 metabolites (GPC, Ala, Tau, Lac, Gln, Glc, GABA, Cr, Asc, mI, NAA, Asp, NAAG, GSH,

Scyllo, PCh, 2HG, PE, and Glu) simulated using the GAMMA library. The range from 0.6 to 4.3 ppm was chosen for the analysis.

A quantitative comparison of metabolite concentration ratios and CRLB values obtained from LCModel was performed. All the voxels inside the area of interest were analyzed, independently of the volunteer, and the different acquisition sequences (7T EPSI, 3T EPSI, and 3T PE MRSI) were compared. This included 243 voxels for 7T EPSI, 75 voxels for 3T EPSI, and 75 voxels for 3T PE MRSI. The reported metabolites included creatine (Cr), myo-inositol (mI), total choline (tCho), N acetyl aspartate (NAA) and glutamate-glutamine (Glx). Additionally, glutamate (Glu) and glutamine (Gln) were included separately in the analysis to show the potential separation of these metabolites at 7T.

Metabolite ratio maps were generated for mI, tCho, Cr, Glx, and NAA. The reconstructed maps were interpolated and visualized together with anatomical information, obtained by integrating axial T1w images over the thickness of the volume selected with semi LASER. To quantify the spatial correlation between metabolite maps and anatomical images, the structural similarity index (SSIM) [116] was computed between the volume selected with semi LASER and the corresponding region in the T1w slice. Additionally, edge maps were extracted using Canny edge detection [15] and overlaid on the maps for a better delineation of gray matter (GM) and white matter (WM) structures.

4.4. Results

The prescription of the water suppressed MRSI scan of one subject (^{7T}V1) and a qualitative comparison between uncorrected, PC, and ECC spectra of two representative voxels (I and II) is shown in Fig. 4.2. The alignment of k-t space in a high SNR PC scan is presented using the original water reference signal (Fig. 4.3 c and d). The correction of the mismatch between even and odd lines in the spatiotemporal signal minimized the ghosts generated by the modulation of the temporal signal. The percentage of aliasing quantified using the real NAA singlet at 2.01 ppm is shown in Fig. 4.3. The spatial distribution of this effect (Fig. 4.3 a and b) showed that ghosting increased with distance to the isocenter in the direction

of the EPSI readout gradient.

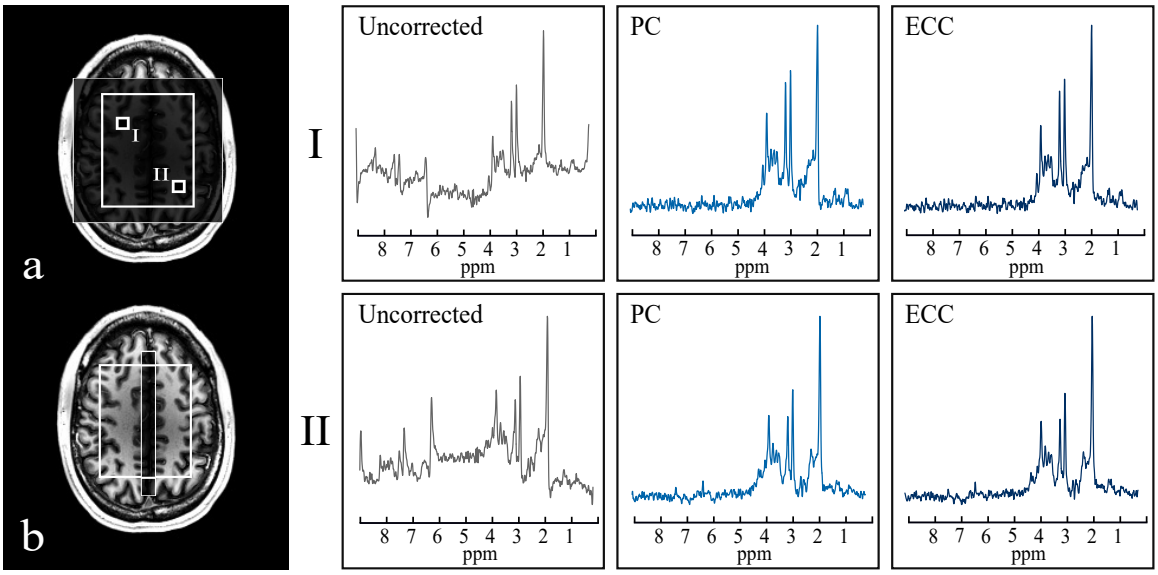

Figure 4.2.: Prescription of (a) the water suppressed MRSI acquisition and (b) the water unsuppressed reference signal acquired with a single phase encoding. For two representative voxels (I and II), uncorrected spectra are presented and the effect of phase correction (PC) is compared to eddy current correction (ECC). PC showed comparable results to ECC but with a negligible increase in acquisition time and a significant reduction in the energy deposition in the subject i.e., total SAR.

The spectral quality was compared qualitatively between acquisitions at 7T (Fig. 4.4) and 3T (Fig. 4.5). The prescribed volume overlaid with the anatomical image and the spectra over a region of interest is shown. Representative spectra of GM and WM voxels showing distinctive features of each tissue type are also presented. The reconstructed 7T dataset was measured with a 4-fold smaller nominal voxel size than the acquisition at 3T.

In Fig. 4.7, the distribution of metabolite concentration ratios and CRLB values obtained from LCModel is shown for all datasets. The expected range of concentration ratios, obtained from literature [91], is displayed in gray. In all cases, the median CRLB was below 20% except for Gln (36%). The metabolite ratio maps computed after LCModel quantification are presented for all the volunteer datasets acquired at 7T (Fig. 4.7). The location and size of the volume prescribed with semi-LASER are presented in the T1w

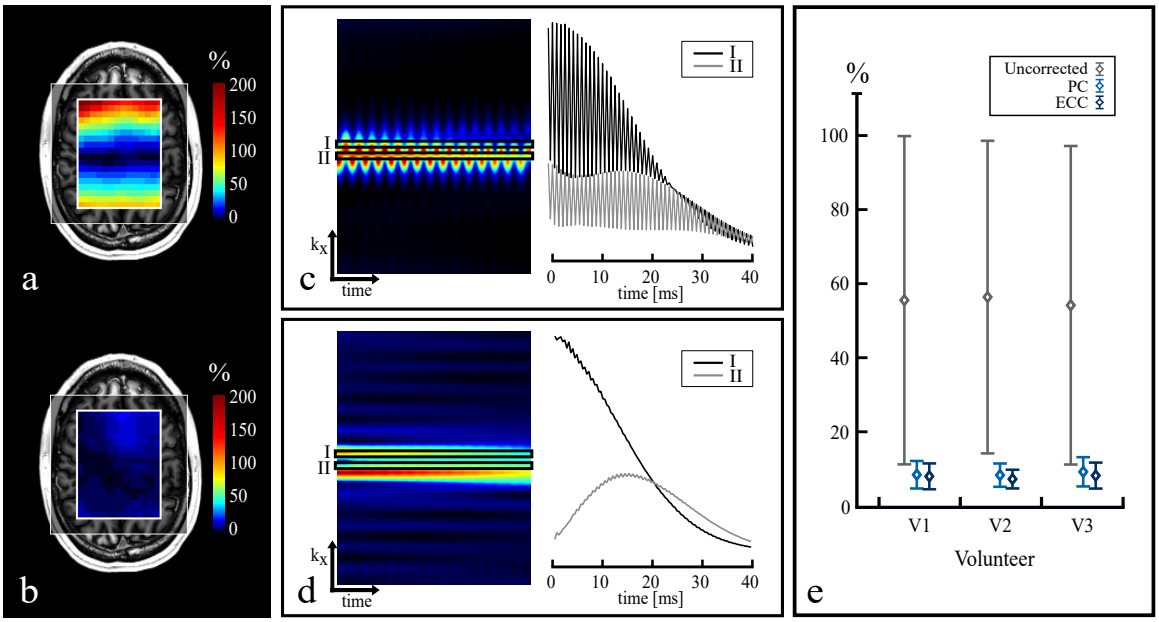

Figure 4.3.: Quantification of the spectral ghosting shown for (a) the uncorrected and (b) the phase-corrected (PC) data. The percentage of aliasing was quantified by NAA-peak integration at the expected ppm location and at the half-bandwidth distance, where aliasing occurred. The effect on the acquired k-t signal in one symmetric EPSI readout is presented for (c) the uncorrected data and (d) after PC. (e) The mean residual aliasing over all voxels in the selected volume is shown for the three volunteers. Quantitative results showed that aliasing removal comparable to ECC could be achieved with PC with reduced acquisition time and SAR.

anatomical images. A noticeable contrast between gray and white matter structures and correlation with anatomical structures were observed in the reconstructed maps. All the volunteer scans measured with the proposed protocol are listed in Table 4.1 and a comparison between volume size, acquisition time, SNR_{peak}, $SNR_{V,t}$, and FWHM of NAA is reported.

4.5. Discussion

Practical considerations for implementing semi-LASER with symmetric EPSI at ultra-high field were presented in this work. An increased resolution with minimal partial volume

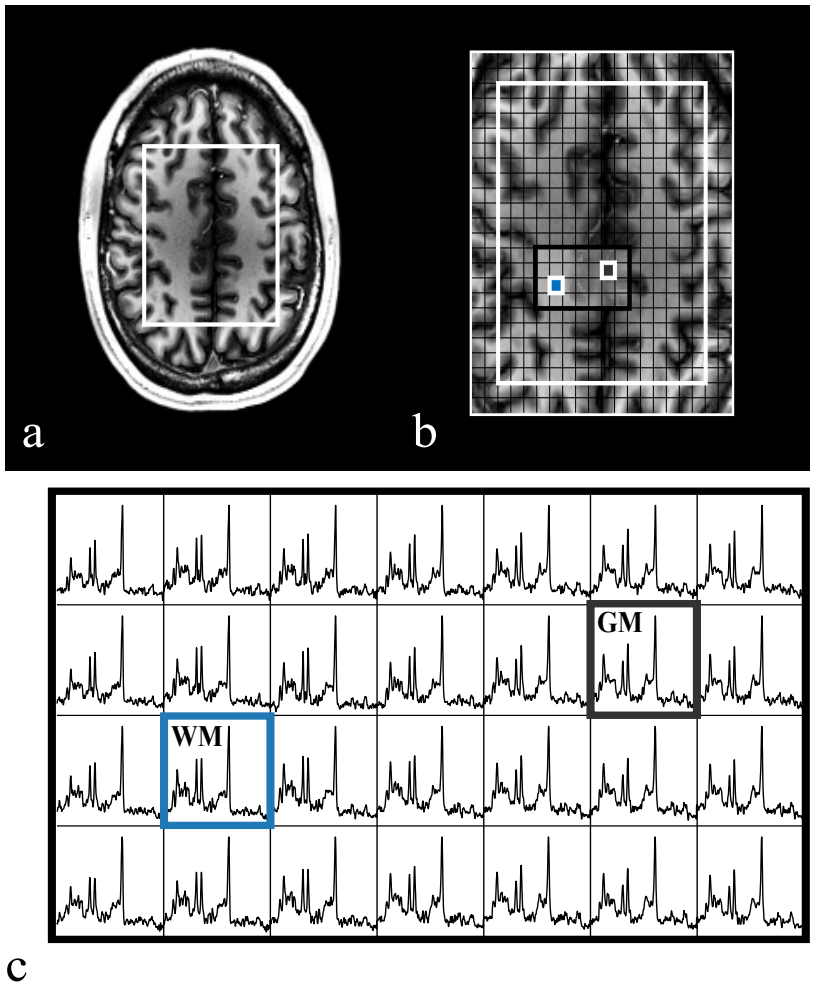

Figure 4.4.: In vivo MRSI dataset (V1) using the proposed protocol at 7T with a voxel size of $0.5 \times 0.5 \times 1.5\,\mathrm{cm}^3$ (0.375 mL). The prescribed volume overlaid with the anatomical image is shown to correlate the spectra with gray and white matter structures (a and b). Spectra over a region of interest and representative white matter (WM) and gray matter (GM) voxels are also presented.

effects was achieved while preserving signal quality. Although this methodology is equally applicable to 3T acquisitions, this method focused on the limitation of MRSI at ultra-high field, namely the increased SAR, increased CSDE, and limitations regarding spectral bandwidth.

The comparison between data acquired at different resolutions, field strengths, and TR was done relative to the SNR per unit volume and unit time. The mean SNR gain at 7T

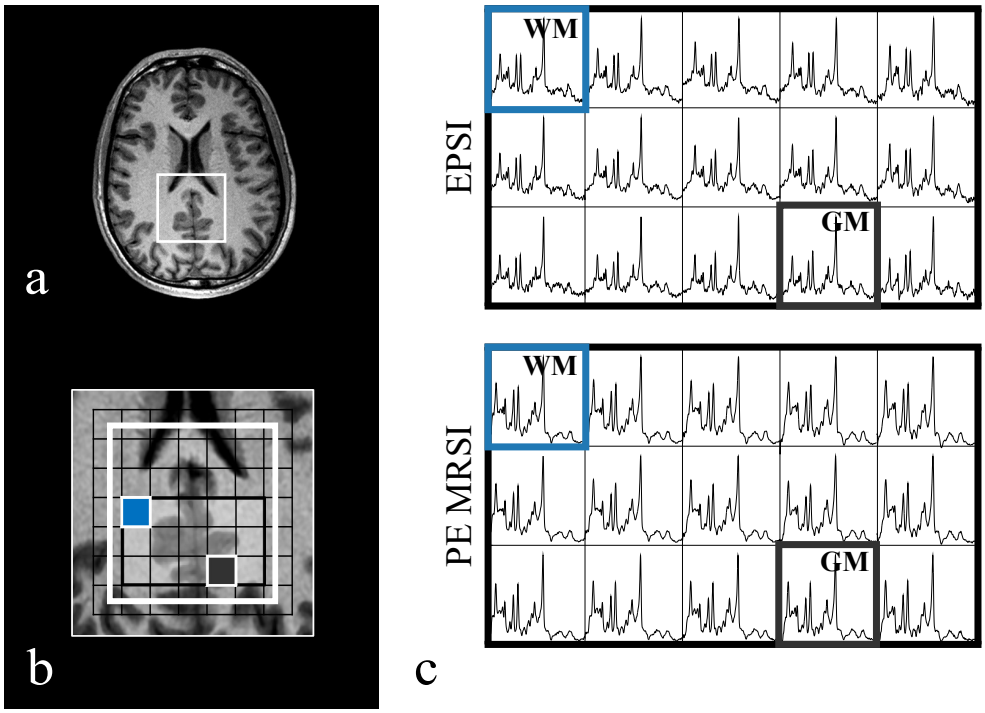

Figure 4.5.: In vivo MRSI data sets acquired using the proposed protocol at 3T with a voxel size of 1.0×1.0×1.5 cm^3 (1.5 mL). The prescribed volume overlaid with the anatomical image allows to correlate the spectra with gray and white matter structures.

achieved of 1.57 (57%) is consistent with previous reports in single voxel spectroscopy [79, 90, 108]. A decrease in the expected signal gain could be explained by the signal decay due to shorter T_2 at 7T, the use of different hardware, and variations in the B_0 and B_1^+ fields.

Mild T_1 saturation effects are expected due to the longer T_1 of the metabolites, although the measurements at 7T were performed with long TR to reduce SAR. Furthermore, a comparable FWHM, i.e. spectral resolution, of the metabolite peaks in ppm was observed. This indicated that the effect of higher B_0-field variations at 7T was compensated by the reduction of the voxel size in plane. The SNR gain has been previously investigated [60], reporting an average SNR ratio of 1.6 between 7T and 3T. Additionally, the expected linear SNR gain (2.33 at 7T) with respect to the field strength was limited by differences in linewidth, T_1 and T_2 at high field strengths.

The PC method introduced here removed ghosting (Fig. 4.3 a, b and e) with a negligible

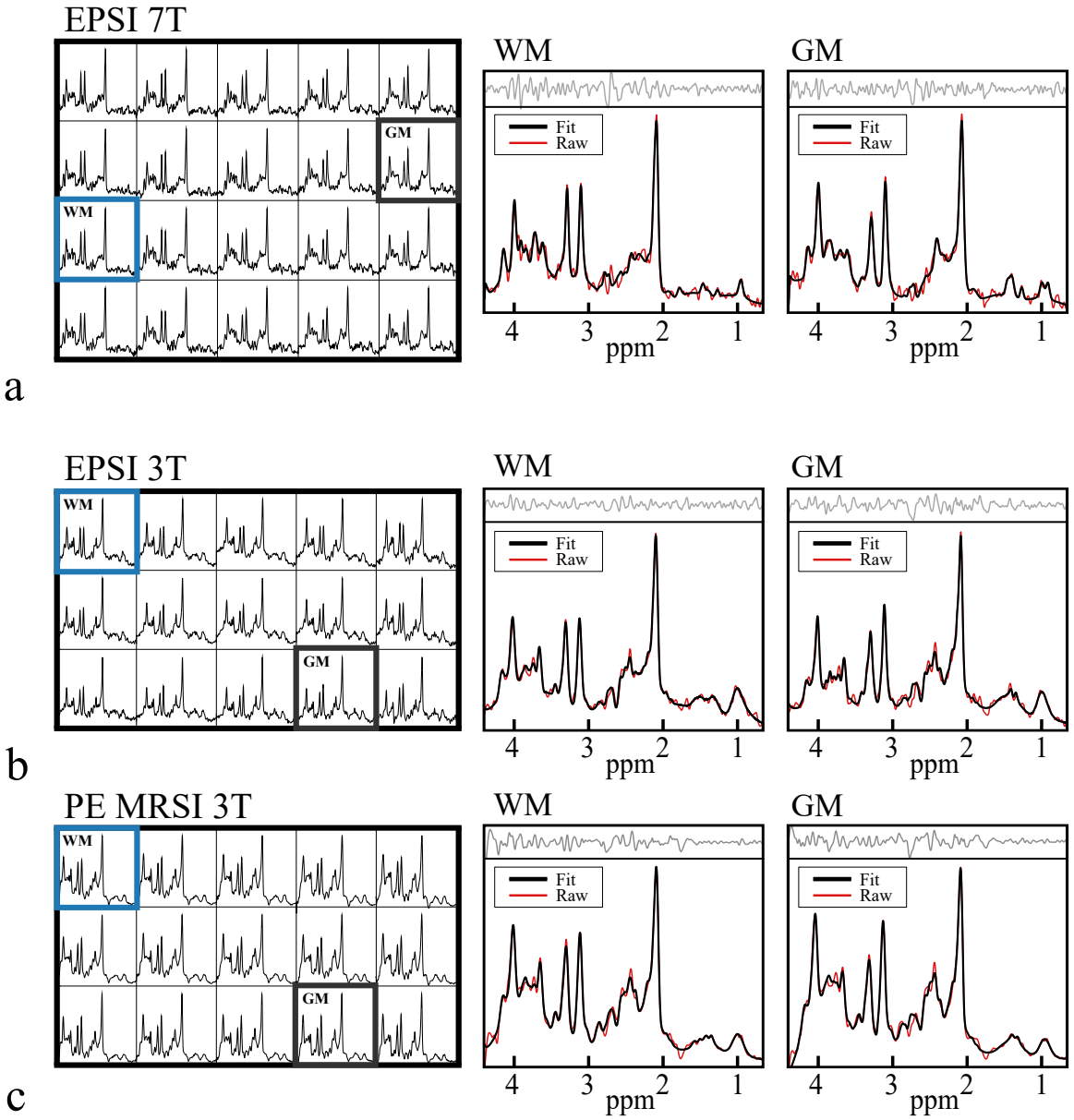

Figure 4.6.: Spectra over the region of interest and the LCModel fit is shown for (a) semi LASER EPSI at 7T, (b) semi LASER EPSI at 3T and (c) phase-encoded MRSI at 3T. For each data set, representative white matter (WM) and gray matter (GM) voxels are presented together with the spectral fit obtained with LCModel. With reduced voxel size, partial volume effects were minimized allowing to better identify spectral features characteristic of each tissue type [91], such as larger choline to creatine ratio (Cho/Cr) in WM compared to GM.

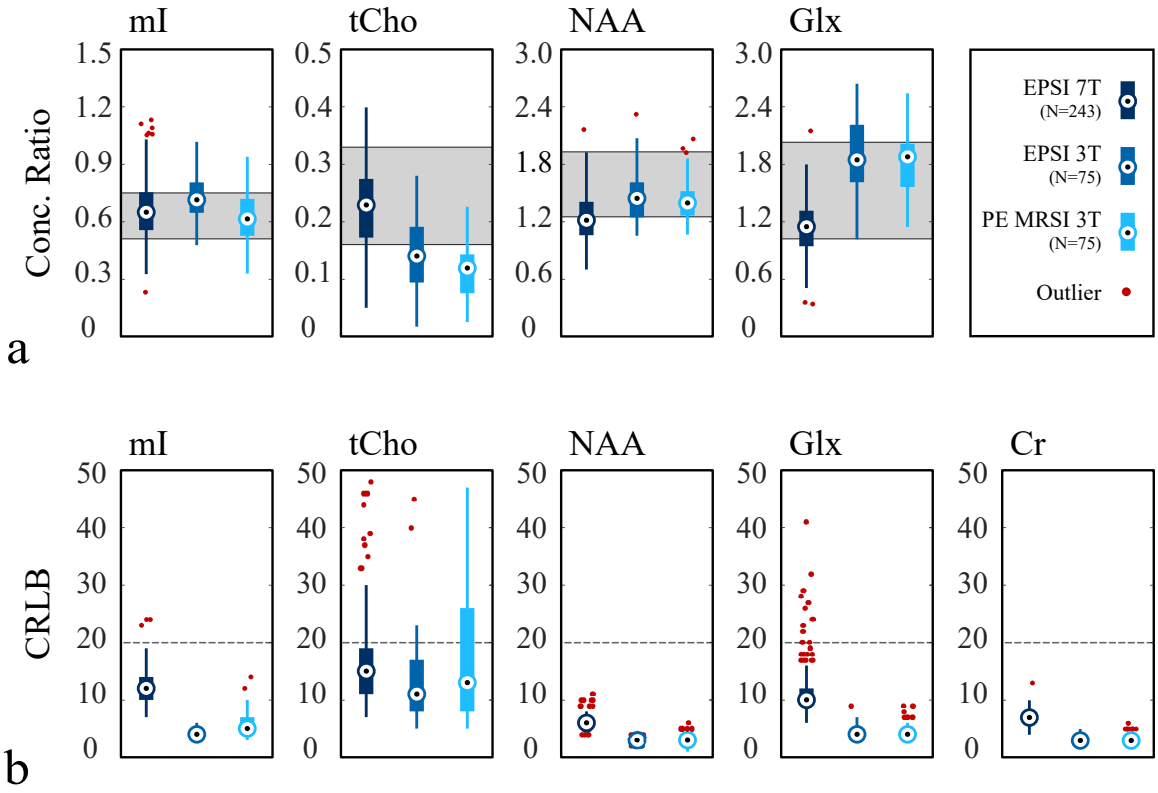

Figure 4.7.: LCModel results comparing (a) the concentration ratios to Cr and (b) the Cramer-Rao lower bounds (CRLB) for all the voxels in the analyzed region of interest with EPSI 7T (N=243), EPSI 3T (N=75) and PE MRSI 3T (N=75). The range of concentration ratios values that has been reported in literature [91] is shown in gray. The distribution of CRLB values shows that fit quality achieved with high-resolution measurements is comparable to lower resolution scans at 3T. The median CRLB was below 20% for all the reported metabolites except glutamine (Gln) measured with EPSI at 7T.

cost in acquisition time using a single shot water reference. As a sufficient spatial resolution (up to 3 mm in EPSI direction) and the spectral bandwidth required at 7T can be achieved with the gradient system (maximum gradient strength 50 mT m^{-1} and slew rate 200 T m^{-1} s^{-1}) in a single shot, interleaved acquisitions were not explored in this work. However, comparable results are expected when applying PC for interleaved scans.

The ECC method, widely used in single voxel and multi-voxel acquisitions [95], was shown here as an effective alternative to correct for inconsistencies in symmetric EPSI,

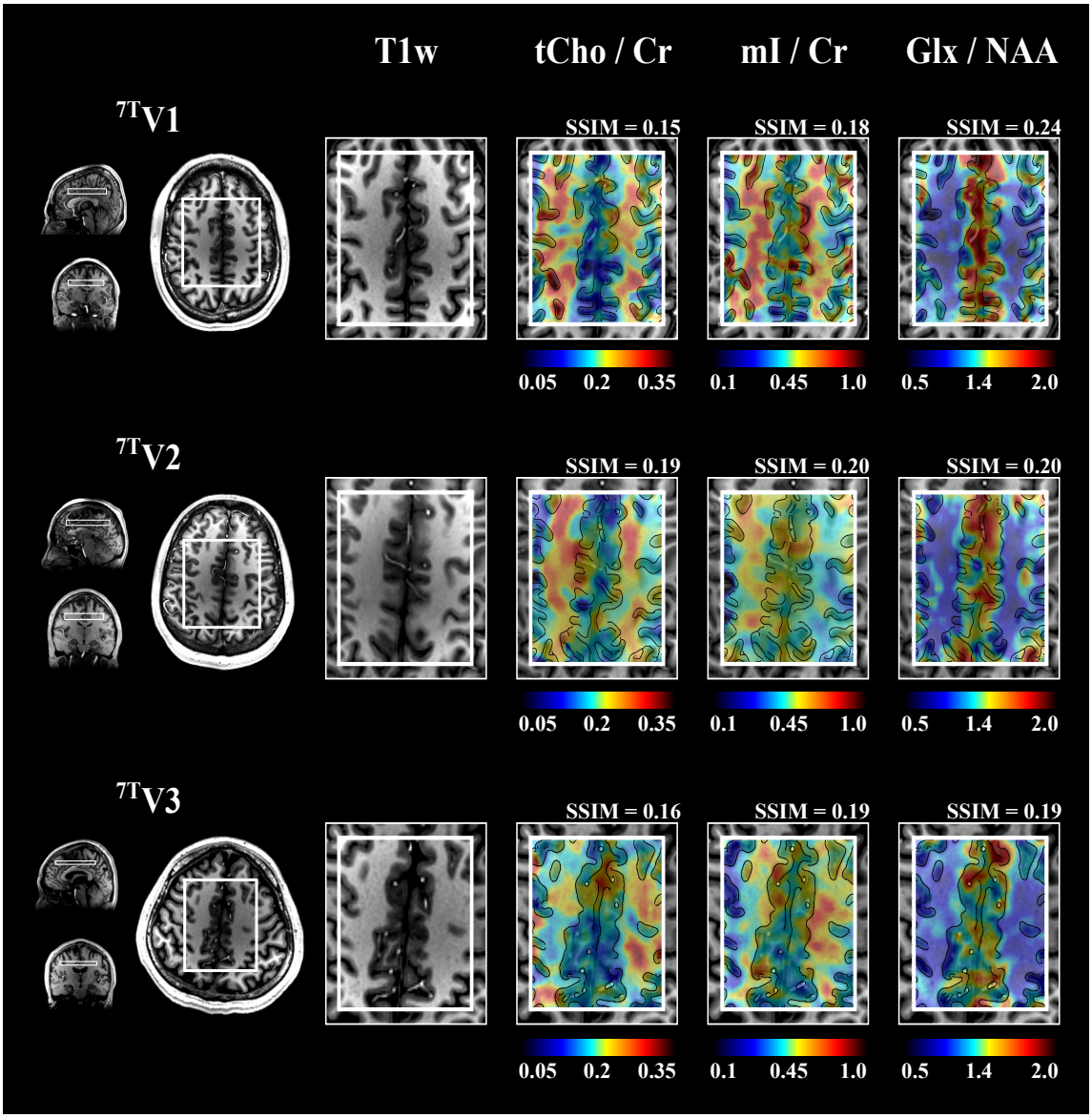

Figure 4.8.: Reconstructed metabolite ratio maps of choline to creatine (Cho/Cr), myo-inositol to creatine (Ins/Cr), and glutamate-glutamine to N acetyl aspartate (Glx/NAA). The maps were computed using LCModel and mapped into the same scale for the three volunteers. Structural features are shown in T1w images integrated over the slice thickness selected with semi-LASER. Edge maps were extracted from the anatomical image and overlaid on the reconstructed maps. The resolution achieved allowed identifying differences in signal intensity expected for WM and GM for the mapped metabolite ratios. The effect of the CSDE was minimal as adjacent metabolites were considered for the computation of the ratios.

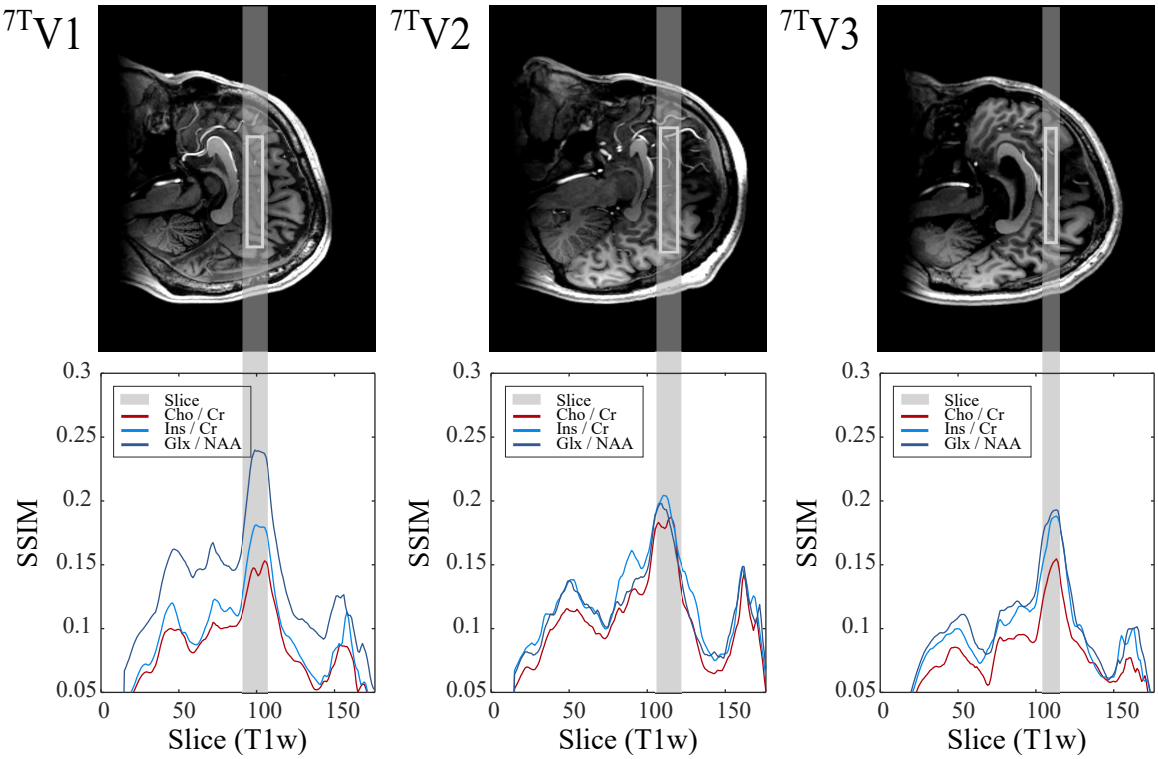

Figure 4.9.: Quantification of the spatial correlation between anatomical (T1w) images and the reconstructed concentration ratio maps using the structural similarity index (SSIM). The SSIM value was computed for all slices in the T1w volume showing the highest correlation at the location of the MRSI measurement.

simultaneously removing phase distortions such as B_0-inhomogeneity, eddy currents, and systems vibrations. Yet, ECC represents less time- and SAR-efficient alternative as it relies on the acquisition of a fully-encoded water reference scan. As the OVS and AFP pulses involved in the sequence account for most of the energy deposited in the subject, the reference measurement may potentially exceed the SAR limits, especially at high fields.

High-resolution scans were achieved without extending the scan duration by reducing the FOV while keeping the matrix size small. This reduced the number of excitations required and kept total energy deposition in the subject under SAR limitations. However, as the selected FOV may not be sufficient to cover the full head, OVS pulses are required to suppress signals outside the volume of interest and avoid spatial aliasing. Alternatively, scans with a larger FOV could be acquired keeping the same nominal resolution and

duration. This could be realized by removing the single pairs of OVS pulses in-plane, thus reducing the SAR per excitation and allowing the shortening of the TR. Nevertheless, as the lower bandwidth excitation pulse produced a larger CSDE, the three pairs of OVS pulses applied in the slice selection dimension could not be removed. Accelerated acquisition sequences have been recently proposed and compared [107], which included encoding efficient sequences using spiral readouts [45] and concentric circle echo-planar trajectories (CONCEPT) [29, 18] capable of acquiring large matrix sizes with high bandwidth. However, in the presence of B_0 inhomogeneity, non-cartesian reconstruction may introduce artifacts that are difficult to correct.

4.6. Limitations

Although the T1w images showed the anatomical context, full comparability with the MRSI scans is still limited with the current slice thickness as partial volume effects and signal bleeding may appear. Additionally, a more extensive study should be performed to study and separate the effects that factors like T_2, T_2^*, T_1, B_0, and B_1^+, have in the reconstructed spectra. Symmetric EPSI with PC achieves a comparable resolution with a robust implementation, nevertheless, whole-brain coverage remains the major challenge for this technique. Both ECC and PC may fail in non-localized ^{1}H MRSI acquisitions due to the presence of strong lipid signals that corrupt the phase estimation from the water reference acquisition.

Part III.

Advanced Quantification Methods for MR Spectroscopy

5. Quantification of Tissue Composition in MR Spectroscopy using Neural Networks

This chapter presents machine learning methods for the analysis, signal enhancement, and quantification of spectra obtained from MRS and MRSI acquisitions. Specifically, methodologies based on Neural Networks (NN) were designed to estimate the tissue partial volumes of gray matter (GM), white matter (WM), and cerebrospinal fluid (CSF), present in an acquired MRS voxel, providing an alternative method to the standard time-intensive MRI segmentation pipeline. The tissue composition was determined from quantified metabolic concentrations using a NN regression model. Moreover, a classification model was generated to determine the specific brain region corresponding to a measured spectrum from both metabolic and tissue components.

The content of this chapter is based on the abstract presented at the 27th annual meetings of the International Society of Magnetic Resonance in Medicine (ISMRM) entitled "Estimation of Brain Tissue Composition and Voxel Location in MR Spectroscopy Using Neural Networks".

5.1. Introduction

Proton MR spectroscopy (MRS) is a quantitative non-invasive modality capable of measuring the metabolic composition of brain tissue quantitatively. However, obtaining a truly quantitative MRS measurement requires a considerable amount of steps added to the

MR acquisition. In clinical MRS, the brain locations that are commonly scanned are the parietal white matter (PWM), posterior cingulate gyrus (PCG), anterior cingulate gyrus (ACG), and left temporal lobe (LTEMP), among others. However, a relatively large tissue volume is excited to achieve good signal quality and high sensitivity, typically between 6mL–10mL. This large volume leads to tissue heterogeneity in the selected voxel, and as a result, the measured spectrum would contain contributions from the different tissue types in the brain: gray matter (GM), white matter (WM), and cerebrospinal fluid (CSF). It is well known that these different compartments present distinctive metabolic signatures due to the tissue structure and cellular composition [115]. Therefore, in order to obtain a reliable metabolite quantification and perform an accurate diagnosis of the results, insight about the tissue composition and brain location is necessary to correct for voxel placement variability, anatomical differences, and partial volume effects.

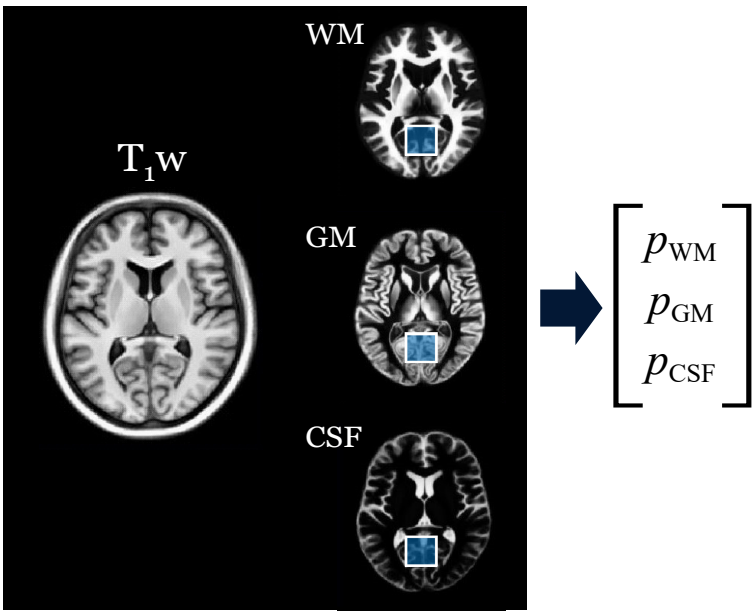

Figure 5.1.: Anatomical T1-weighted image showing the output of the segmentation algorithms where the spatial distribution of brain tissue types is extracted. A typical MRS voxel located in the posterior cingulate gyrus (PCG), is displayed in blue. Inevitably, the scanned volume will contain contributions of all tissue compartments, denoted as the partial volume of gray matter, white matter, and cerebrospinal fluid, respectively p_{GM},p_{WM}, and p_{CSF}

Nevertheless, the procedure to obtain this tissue information, shown in Figure 5.2, is time-consuming and difficult to integrate into a clinical setting, mainly because it involves the acquisition of a T1-weighted (T1w) MR volume, the use specialized segmentation software (e.g. FSL [42]), and the extraction of metadata containing the position and orientation of the MRS volume.

This work proposes the use of supervised machine learning algorithms, specifically neural networks (NN), to estimate the partial volume of GM, WM, and CSF, which contribute to the MRS signal directly using the relative concentrations of brain metabolites obtained from the spectral quantification. Additionally, NN-based classification models were used to determine the brain location of an MRS scan using the metabolites and tissue heterogeneity information.

5.2. Theory

5.2.1. Absolute Metabolite Quantification

Absolute metabolite concentrations are calculated from the output of the spectral fitting software when a water reference is used to properly scale the metabolite signal. To obtain proper concentrations in mmol per volume of tissue (mmol/L) or mmol per mass of tissue (mmol/Kg), it is necessary to correct for different effects that include: water content in the sample, T2 relaxation of both water and metabolite signals (h_{T2}), scanner specific gain calibrations and partial volume fractions (PVF) of the different tissues contained in the sample. For simplicity, T1 effects of water and metabolites are typically assumed to be equivalent and therefore not included in the correction factors.

Tissue fractions correspond to the partial volume of gray matter (p_{GM}), white matter (p_{WM}) and cerebrospinal fluid (p_{CSF}), in the measured volume and were computed from the segmented of the T1 weighted (T1w) anatomical volume at the MRS voxel location. The absolute metabolite concentrations per total volume of brain tissue $C_{met}^{V_t otal}$ (mol/L) are calculated as follows:

$$C_{\text{met}}^{V_{\text{total}}} = C_{\text{met}}^{\text{LCM}} \times h^{\text{Tissue}}, \tag{5.1}$$

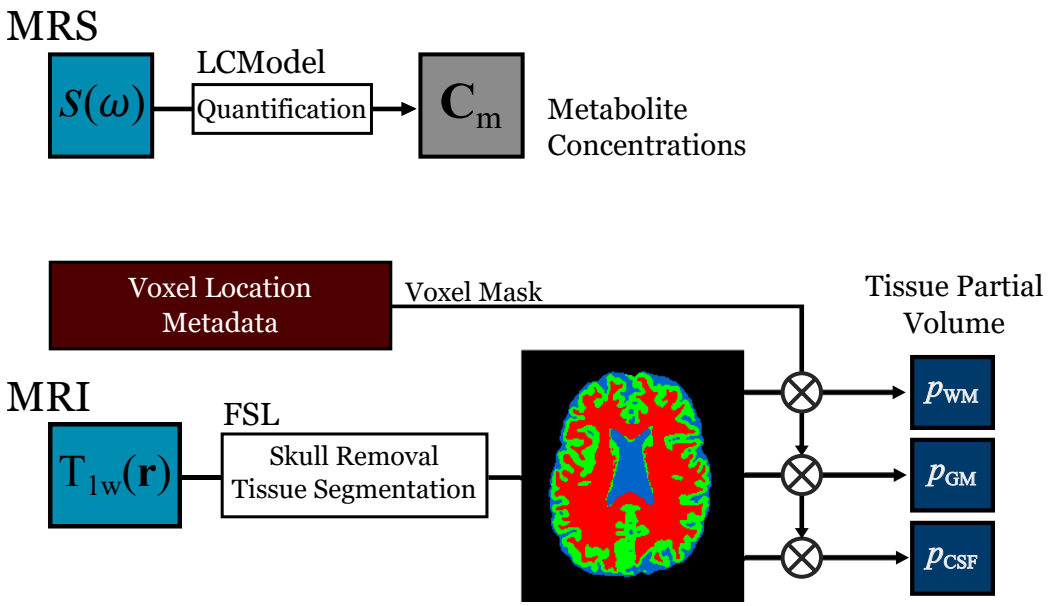

Figure 5.2.: Standard pipeline used to compute tissue partial volumes (p_{GM},p_{WM}, and p_{CSF}) from the MRS and MRI datasets. First, the measured MRS spectrum is quantified with LCModel to obtain the metabolite concentration ratios (C_m), that need to be corrected for tissue composition. To achieve this, a T1-weighted (T1w) volume is segmented to obtain the volume probability map of each tissue type at a high resolution (1 mm^3). Then, a mask of the MRS volume is generated from the metadata and applied to the segmented volume. The values of partial volume are calculated from the sum of each tissue class in the masked volume.

where $C_{\text{m}}^{\text{LCM}}$ corresponds to the ratio between the area of the metabolite fit and the water reference signal obtained from LCModel. The tissue correction factor h^{Tissue} is computed as:

$$h^{\text{Tissue}} = (0.78 \cdot h_{\text{GM}}^{T_2} \cdot p_{GM}) + (0.65 \cdot h_{\text{WM}}^{T_2} \cdot p_{WM}) + (1.0 \cdot h_{\text{CSF}}^{T_2} \cdot p_{CSF}) \tag{5.2}$$

where $h_{\text{Tissue}}^{T_2}$ is the correction factor for the T_2 decay of water in the corresponding tissue type ($h_{\text{GM}}^{T_2} = h_{\text{WM}}^{T_2} = h_{\text{CSF}}^{T_2} = 0.646$).

The absolute metabolite concentration per volume of brain tissue $C_{\text{met}}^{V_{\text{Brain}}}$ (mol/L) is computed by only including the contribution of the brain tissue volume ($V_{\text{Brain}} = 1 - p_{\text{CSF}}$):

$$C_{\text{met}}^{V_{\text{Brain}}} = (0.78 \cdot h_{\text{GM}}^{T_2} \cdot p_{GM}) + (0.65 \cdot h_{\text{WM}}^{T_2} \cdot p_{WM}) + (1.0 \cdot h_{\text{CSF}}^{T_2} \cdot p_{CSF}) \tag{5.3}$$

Finally, the absolute concentration values per mass of brain tissue $C_{\text{met}}^{m_{\text{Brain}}}$ (mol/kg) are computed from the concentration per volume of brain tissue divided by the brain tissue density ($_{\text{Brain}} = 1.05kg/L$):

$$h^{\text{Tissue}} = (0.78 \cdot h_{\text{GM}}^{T_2} \cdot p_{GM}) + (0.65 \cdot h_{\text{WM}}^{T_2} \cdot p_{WM}) + (1.0 \cdot h_{\text{CSF}}^{T_2} \cdot p_{CSF}). \tag{5.4}$$

5.3. Methods

Based on the fact that brain tissue types have characteristic metabolic compositions (Fig. 5.3), the partial volumes of GM, WM, and CSF (p_{GM}, p_{WM}, and p_{CSF}) were determined from the metabolite concentrations (C_m) of a given spectrum using a regression model. In a similar way, as anatomical brain regions are metabolically and structurally different, the region corresponding to a given spectrum could be determined using a classification model. Figure 5.2 shows the standard procedure to determine the tissue partial volume fractions from T1-weighted scans and the MRS voxel location using segmentation algorithms. Figure 5.5 shows the proposed pipeline that estimates the tissue partial volumes from the quantified metabolite concentrations.

5.3.1. Data collection and Processing

This study presents a meta-analysis of 745 spectra obtained from 272 subjects measured at 4 brain regions (PCG=198, PWM=200, ACG=180, LTEMP=167). The scans were performed at 3T using PRESS localization and the following scanning settings: TR=2000 ms, TE=30 ms, voxel size 20×20×20 mm^3, number of averages=128. The voxel location and orientation were extracted from the metadata on the header of the MRS acquisitions. T1w volumes of all the subjects were collected using MPRAGE at 1 mm^3 isotropic resolution. For all the MRS scans, a mask of the measured volume was generated from the metadata and applied to the segmented anatomical volume. Finally, the partial volume fractions were calculated from the sum of the probability of each tissue class within the masked volume.

MRS and MRI datasets were processed following the standard pipeline detailed in Figure

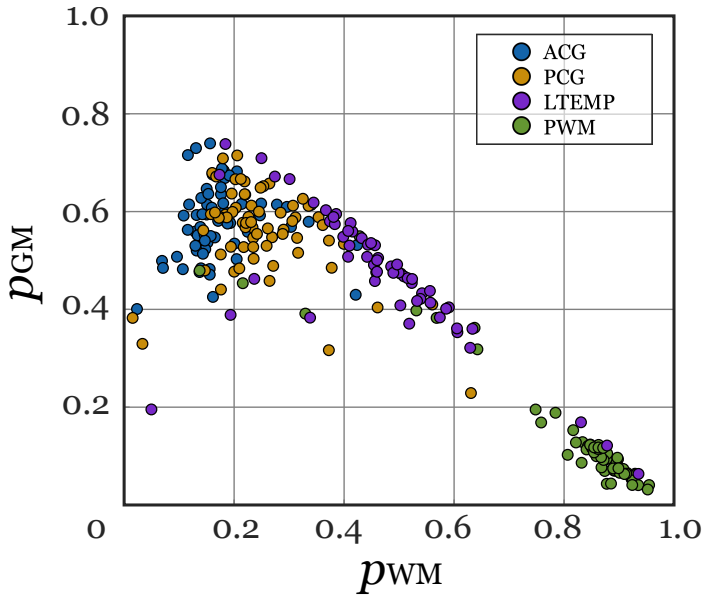

Figure 5.3.: Analysis of the data used to train the NN classification and regression models. The partial volume of GM is plotted against the partial volume of WM for individual voxels acquired at 4 brain locations (PCG, PWM, ACG, and LTEMP). The degree of variability in the composition due to differences in voxel size, voxel placement, and anatomy are observed. Up to a 40% variation are evident for voxels that correspond to gray matter structures, i.e. ACG and PCG.

5.2. The MRS datasets were reconstructed with an in-house Python-based pipeline using OpenMRSLab [5] and quantified with LCModel [91]. Metabolite ratios were used to account for scanner and subject variability. The brain segmentation process was performed on the T1w anatomical volumes using the FSL software library [42] after skull removal.

5.3.2. Regression Model for Tissue Composition

The neural network regression model was trained in Matlab (MathWorks) using the creatine ratios of 18 metabolites (GPC, Ala, Tau, Lac, Gln, Glc, GABA, Cr, Asc, mI, NAA, Asp, NAAG, GSH, Scyllo, PCh, PE and Glu) and 9 macromolecular and lipid components as features. From the whole labeled dataset, 70% of the scans, randomly selected, were used for training, 15% for testing, and 15% for validation. The trained NN consisted of 20 hidden layers. Moreover, 10-fold cross-validation was implemented to obtain the average

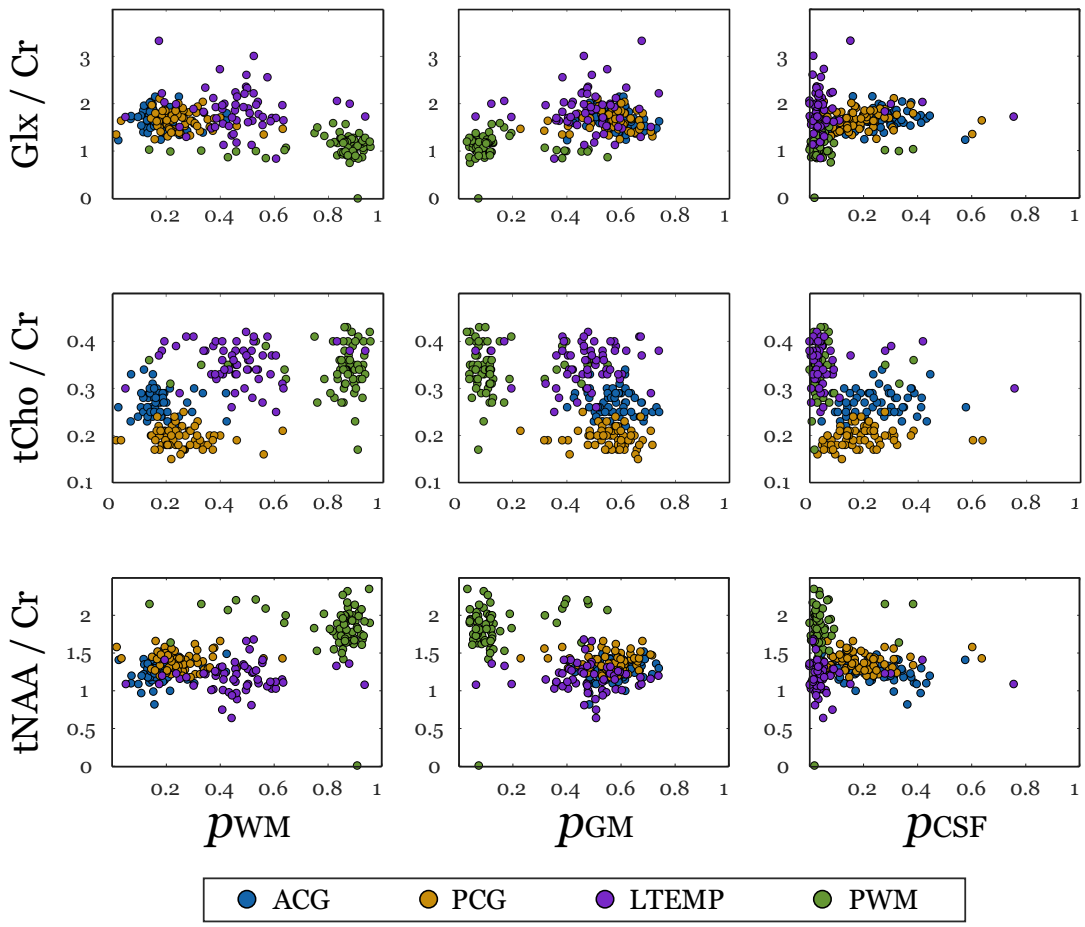

Figure 5.4.: The scatter plots show 2D projections of the high dimensional feature space, which include the quantified metabolite concentrations (C_m) and the partial volumes of WM, GM, and CSF (p_{GM},p_{WM}, and p_{CSF}). In some projections, a clear separation of the brain regions was observed, suggesting that the metabolite ratios and tissue volumes can be used as features to create a regression model.

performance of the network.

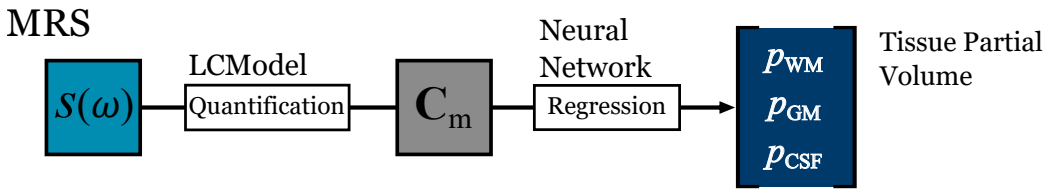

Figure 5.5.: Proposed neural network regression pipeline to estimate the tissue partial volumes from the metabolite concentration ratios.

5.3.3. Classification Model for Voxel Location

In a similar way, the NN classification model was trained in Matlab (MathWorks) using the 18 metabolite rations and 9 macromolecular and lipid components extracted with LCModel. Additionally, the partial volumes of GM, WM, and CSF extracted from anatomical T1w volumes and FSL were included as features. The training dataset was build from 80% of the labeled spectra, the testing and validation sets included 10% of the remaining data. The network architecture had 100 hidden layers and was trained with 10-fold cross-validation.

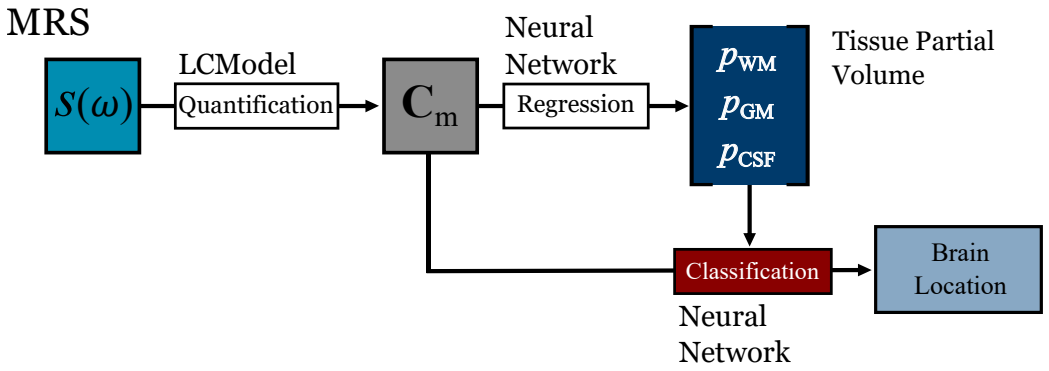

Figure 5.6.: Proposed neural network pipeline for the classification of brain location from the estimated tissue partial volumes (p_{GM},p_{WM}, and p_{CSF}) and metabolite concentration ratios (C_m).

5.4. Results

The training performance of the regression model for tissue volume estimation was evaluated and is shown in Figure 5.7. The optimal learning performance was obtained with a mean squared error (MSE) of 0.013. This value can be considered proportional to the magnitude of the error in the partial volume obtained with the segmentation. A correlation coefficient between the ground truth and the predicted tissue compositions of R=0.92 and R=0.89 was achieved for the training (70%) and the testing (15%), respectively. Finally, a mean absolute error (MAE) of 0.114 was obtained, which corresponded to an 11.4% variability in the voxel composition of an MRS measurement. Given the low concentration of metabolites present in the CSF compartment of the measurement, it was observed that this compartment introduced uncertainty of the partial volumes. This could explain the limit in the minimum MSE and MAE obtained with the current approach. Nevertheless, the correction of CSF in quantitative MRS corresponds to a scaling factor in the concentrations, which could be obtained from the magnitude of the water signal.

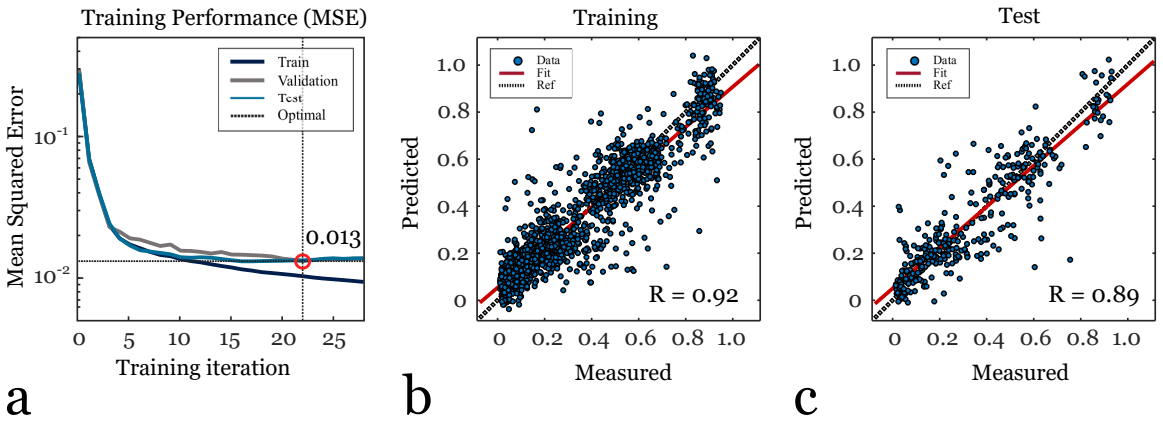

Figure 5.7.: Regression of tissue partial volumes from metabolite concentrations. (a) Training performance showing the optimal mean squared error (MSE=0.013) achieved in the validation set. (b) Correlation (R=0.92) of the predicted partial volume and the true values in the training set (70%) and (c) correlation (R=0.89) of the predicted partial volume and the true values in the test set (15%).

The model for classification of Figure 5.8 presents the results of the brain region classification. High classification accuracy (>0.94) for all regions was achieved. In terms of the importance of features, the metabolite ratios of total N-acetyl aspartate (tNAA), total choline (tCho), and glutamate+glutamine (Glx) to creatine (Cr) were strongly weighted by the regression model. This result is consistent with the fact that these metabolites have a low quantification error (CRLB10) and previous analysis of different tissue composition obtained by biopsies have shown significant differences of these metabolites in gray and white matter [115].

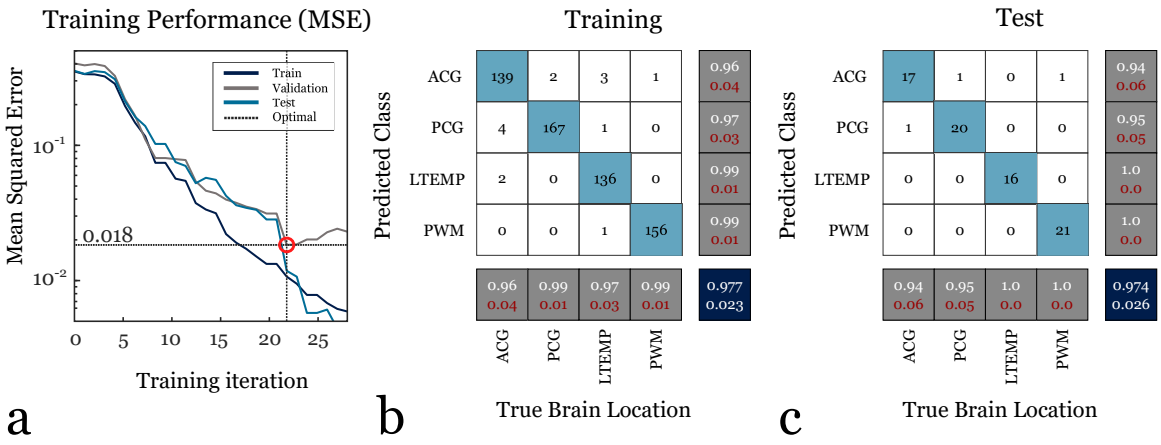

Figure 5.8.: Classification of brain location using neural networks. (a) Training performance showing the optimal mean squared error (MSE=0.018) achieved in the validation set consisting of 10% of the data points. (b) Confusion matrix of the training set (80%) showing high classification accuracy for the 4 different brain locations. (c) Confusion matrix of the test set (10%) showing the classification accuracy.

5.5. Discussion

This work presented a machine learning approach for the estimation of tissue partial volumes and brain location of MRS acquisitions. From the analyzed datasets, the variability of the voxel composition was analyzed. This variability in the tissue composition could be up to 40 percent in brain locations where the gray matter is prominent, such as ACG

and PCG. This not only has to do with the operator-dependent voxel placement variability, but also with the anatomy of the patient and voxel size. High accuracy was achieved for the classification of very distinctive brain regions such as temporal lobe and white matter, and slightly lower for ACG and PCG that are very similar in structure and composition. Additionally, a higher false-positive rate for ACG and PCG was obtained in the classification task (Fig. 5.8) due to potential structural and metabolic similarities between these brain locations.

The proposed method represents an alternative to tissue segmentation algorithms. These require specific anatomical volumes and voxel metadata that are not standardized across vendors. Standard algorithms can also be computationally expensive and sensitive to image properties such as contrast differences, SNR, and resolution. Finally, in the presence of artifacts or inhomogeneities, these methods are prone to errors. Moreover, the trained NN model allows for fast computation of tissue partial volumes in a compact pipeline. This can be potentially implemented to run in real-time at the scanner to navigate the positioning of the voxel prior to the acquisition, which is of special interest in longitudinal examinations. In this way, an improved the reproducibility of MRS and reliability of the metabolite quantification would facilitate the integration and use of this technology in a clinical context.

5.6. Limitations

In the field of supervised machine learning, the proper generalization of the model is very important to reliably apply the trained models in a clinical setting. First, visual inspection of automatically segmented anatomical volumes is necessary to remove cases where the algorithms fail. Also, the data points used for training need to capture the variability of the studied population in terms of age, demographics, sex, among others, for both health and disease conditions. Therefore a very extensive curated database needs to be collected to train and validate the NN models. For the case of MR spectroscopy, such a large number of scans can only be obtained with a multi-site collaboration, initially focused on specific

diseases, and gradually validate it for more applications. Additionally, data harmonization and calibration methods need to be implemented to remove biases in the data and achieve robust machine learning models.

6. In-Vivo Quantitation of Down-Field Metabolites using MR Spectroscopy

This chapter describes a methodology for the measurement of down-field resonances in the brain using standard localized magnetic resonance spectroscopy (MRS) sequences and LCModel regression for quantification. This approach models the metabolite components up-field from the water signal using nuclear magnetic resonance (NMR) simulations to create an accurate representation of the metabolite signal, effectively incorporating prior knowledge to the quantification. A calibration phantom with known metabolic concentrations was developed to perform scanner specific calibrations of the measurement. This accounts for acquisition imperfections that typically lead to inaccurate or unreliable measurements. The content of this chapter is based on the abstract presented at the 27th annual meetings of the International Society of Magnetic Resonance in Medicine (ISMRM) entitled "Regional Differences in Cerebral Phenylalanine Measured with Single Voxel Spectroscopy using PRESS Localization and LCModel Quantification".

6.1. Introduction

Single voxel spectroscopy (SVS) allows for a direct measurement of metabolite levels in the brain non-invasively. However, the quantification of some metabolites, such as the resonances down-field from the water signal, is substantially more challenging due to their relatively low concentration and the limited sensitivity of the technique in that regime. For a

reliable detection of these metabolites in the brain using SVS, some important considerations have to be taken into account [52]. These include: to incorporate accurate prior knowledge to fit the spectral signal using metabolite basis functions and baseline components, to correct potential chemical shift displacement error (CSDE) of the acquisition, and to account for differences in the frequency profile of the RF excitation and refocusing pulses. Considering these factors, a range for the ratio between the Phe concentration in blood and the Phe concentration in brain tissue in the order of 2- to 4-fold has been reported. An example of these down-field resonances is Phenylalanine (Phe), an essential amino acid acquired through diet and metabolized in the liver to tyrosine (Tyr) by the enzyme phenylalanine hydroxylase. Under normal conditions, the concentration of Phe ranges between 0.07–0.30 μmol/ml in blood, and 0.05–0.30 μmol/g in brain tissue [71, 84, 83]. Phenylketonurea (PKU) is a rare genetic condition where the absence of the enzyme phenylalanine hydroxylase causes high Phe levels in blood and consequently its accumulation in tissues [70]. A high concentration of this metabolite in the brain leads to significant neurological and neuropsychological problems and hinders the intellectual and behavioral development. Although newborn screening guarantees an early detection this disease, methods to monitor PKU are limited, particularly in older children and adults who struggle with dietary compliance. The quantification of Phe has been explored in previous studies [54, 85, 56], mainly at low magnetic fields (1.5T), using STEAM localization [13] and measuring relatively large volumes (8-70 mL) in order to obtain reasonable SNR and sensitivity. Although these techniques showed to be effective modeling the down-field spectrum, the large measured volume eliminates the spatial context of the signal, which is of interest to study regional differences, such as white matter abnormalities caused by the accumulation of Phe in the brain of PKU patients [67]. Moreover, the fitting algorithms used to estimate the concentration values are not widely available. The advantages in the detection of Phe using 3T scanners have been recently shown [100]. First, a higher SNR can be achieved at 3T and PRESS localization [28], when compared to STEAM at 1.5T. Consequently, measurement of smaller volumes is possible, enabling localized tissue analysis. Furthermore, the intrinsic lower T2 at high field strengths causes the macromolecular components of the baseline

down-field from the water resonance to decay faster than the metabolites of interest. This partially eliminates the dependency of the quantification on the macromolecular baseline model that could potentially lead to a significant over- or underestimation of the Phe concentration. Nevertheless, some of the previously described technical challenges are still to be properly addressed to obtain reliable Phe measurements. Specifically, the substantial CSDE of PRESS at 3T that reduces the effective excitation volume for the Phe resonance frequencies at 7.4 ppm. This CSDE, which can be in the order of 50% given the bandwidth of standard refocusing pulses (1.4 kHz) and the chemical shift difference between the Cr singlet at 3.0 ppm and the main Phe resonances at 7.4 ppm [4], needs to be considered when modeling the basis sets used by LCModel. Furthermore, the RF pulse profile of the excitation and refocusing pulses is not homogeneous throughout the frequency range of interest and is difficult to determine. Alternatively, 2D spectroscopic approaches such as localized Correlation Spectroscopy (COSY) [109], have shown to be useful for the detection of this metabolite [114]. Although, an improved spectral dispersion of coupled metabolites like Phe or tyrosine (Tyr) is achieved, the quantification of 2D spectroscopic methods is not well stablished and the availability of COSY sequences is limited in clinical scanners. This work describes a methodology for the quantification of Phe in the brain using SVS with the standard SNR-efficient PRESS localization and LCModel quantification [91], measured at 3T. This approach models the metabolite components up-field from the water signal incorporating prior knowledge to the quantification. Moreover, this method incorporates a calibration step that accounts for the main acquisition imperfections that may lead to inaccurate or unreliable Phe measurements, namely the relatively large CSDE of Phe and the inhomogeneous excitation profile of the PRESS RF pulses.

6.2. Methods

6.2.1. Signal Model and Basis Set Simulation

Basis functions for the down-field and up-field metabolite components were generated with the Vespa Simulation and Priorset software [106] using chemical shift values and J-coupling

constants from the literature [31]. The relevant metabolites added to the standard basis set were: phenylalanine (Phe), tyrosine (Tyr), homocarnosine (Hcar), and broad amide (NH) resonances from NAA (lNAA) and creatine (lCr) at 7.8 ppm and 6.6 ppm, respectively. For Phe and Tyr, a separate model for the down-field (lPhe and lTyr) and up-field (rPhe and rTyr) spectral portions of the metabolites was created to account for the uneven excitation of these resonances. Similarly, a set of the standard brain metabolites was simulated. These included: glycerophosphocholine (GPC), alanine (Ala), taurine (Tau), lactate (Lac), glutamine (Gln), glucose (Glc), GABA, ascorbate (Asc), myo-inositol (mI), aspartate (Asp), N-acetyl-aspartyl glutamate (NAAG), glutathione (GSH), scyllo inositol (Scyllo), phosphorylcholine (PCh), phosphoryl ethanolamine (PE) and glutamate (Glu).

6.2.2. MR Acquisition Sequence and In-vivo Experiments

MR spectra of the posterior cingulate gyrus (PCG) and parietal white matter (PWM) were acquired for three groups of PKU subjects (N=25) and one control group (N=9). The scans were performed at two different 3T scanners (Trio and Skyra; Siemens, Erlangen, Germany) using a 32-channel receiver coil. The single voxel spectroscopy (SVS) sequence incorporated water suppression, outer volume suppression, and PRESS localization with the following parameters: TE/TR = 35/2000 ms, 32 signal averages, the center frequency of the excitation pulse at 2.4 ppm, and a voxel size of $30\times30\times30$ mm^3 (27 mL) and $40\times20\times30$ mm^3 (24 mL) for the PCG and PWM voxels, respectively. The protocol included one acquisition with water suppression (SVS_{Wsup}) and one without water suppression (SVS_{Wref}) used for absolute quantification. Anatomical MRI measurements were also acquired using a T1-weighted (T1w) 3D magnetization prepared rapid gradient echo (MPRAGE) sequence with a slice thickness of 2.5 mm and a field of view (FOV) of 20×25 cm. These MRI scans were used to correct for tissue composition and to prescribe the voxel location of the SVS scans.

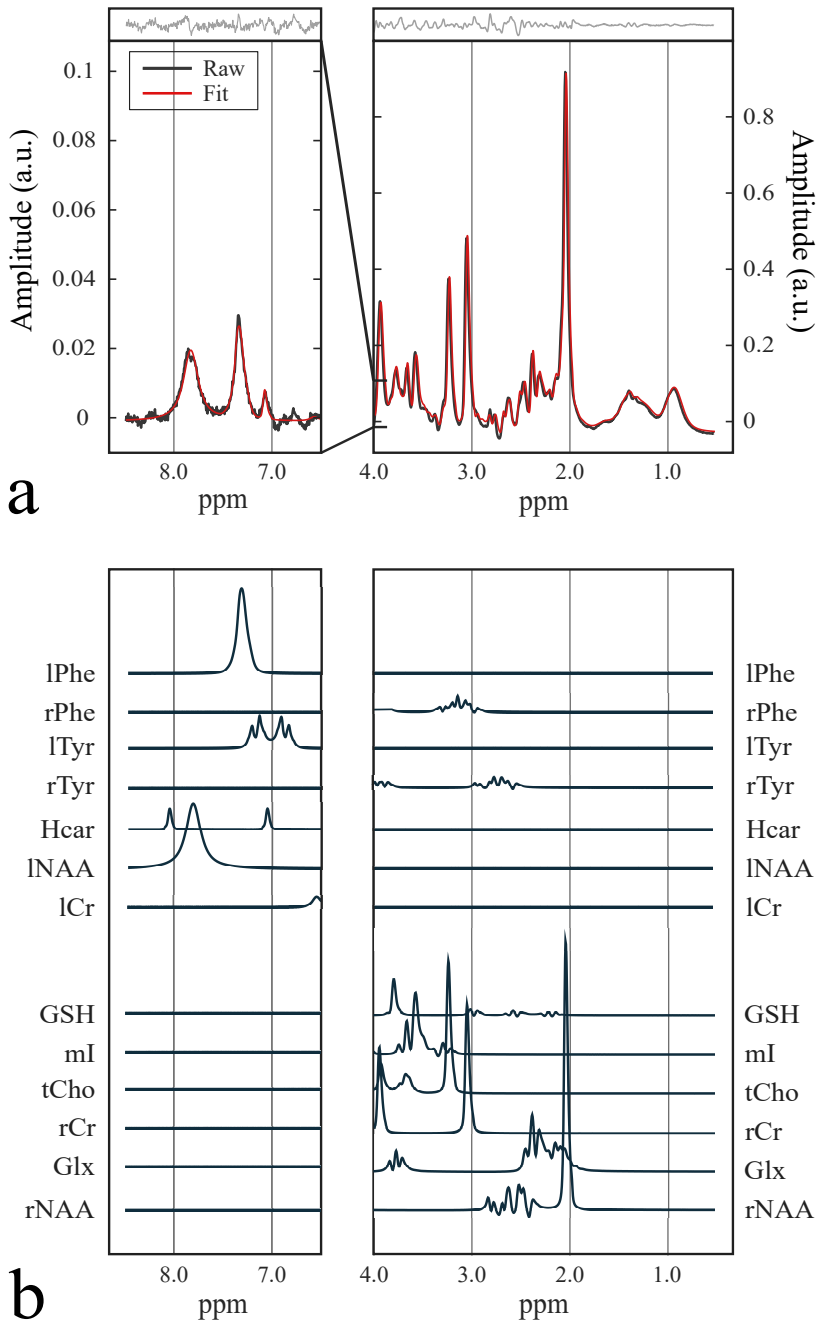

Figure 6.1.: (a) LCModel fit performed on the sum of all in-vivo spectra (N=68) to achieve a high SNR for the down-field metabolites. (b) A subset of the simulated metabolite basis functions used to model the spectrum down-field from the water peak and quantify phenylalanine (Phe). The resonances added to the standard brain basis set were phenylalanine (Phe), tyrosine (Tyr), and homocarnosine (Hcar).

6.2.3. Phantom Calibration

A calibration phantom with known metabolic concentrations was developed to determine correction factors related to (i) the inhomogeneous profile of the excitation and refocusing pulses, (ii) the reduction of the effective excited volume of individual metabolites caused by the CSDE, and (iii) the scanner specific gain. Moreover, it helped to validate the fitting routine with high SNR spectra.

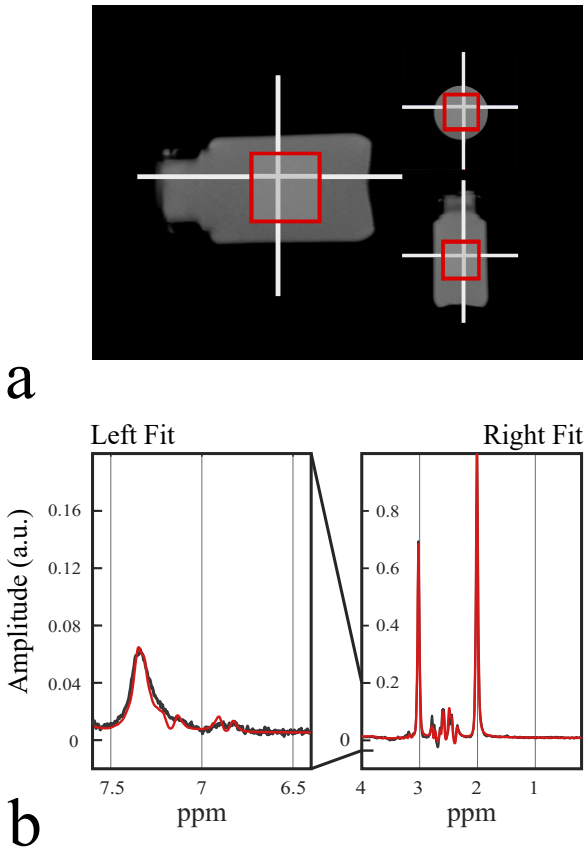

Figure 6.2.: Phantom experiments performed using PRESS with a voxel size of $30\times30\times30\text{mm}^3$ (27mL) and the same scan parameters as the in vivo experiments. (a) Phantom and prescribed volume location. (b) Measured spectra of the calibration phantom. The result of the LCModel fit is shown in red for both down-field (Left Fit) and up-field (Right Fit) from the water peak.

The phantom containing NAA, Cr, Phe, and Tyr, with concentrations in the physiological range was scanned using the same acquisition protocol (Fig. 6.2). The acquired spectrum

was quantified using LCModel assuming the specific T1, T2 and water concentration values of a solution phantom (ATTMET=1.0, ATTH20=exp(TE/80)=0.646, WCONC=55556). Finally, a mean correction factor that includes all the effects listed above was then calculated to match the ground truth concentration, i.e. the actual amount mixed in the phantom.

6.2.4. Spectral Processing

The MRS spectrum was reconstructed using OpenMRSLab [5], a Python-based software package. The processing pipeline included the following steps: (1) signal combination of multi-channel receiver coil, (2) correction of the frequency misalignment between signal averages, (3) coherent signal averaging, (4) eddy current correction, (5) removal of the residual water signal, and (6) removal of the phase offset in the spectrum. All processing steps were applied to both the SVS_{Wsup} and SVS_{Wref} datasets except for (5) which was only applied to SVS_{Wsup}.

The processed spectrum was then quantified with LCModel [91] using the complete simulated basis set. The fitting process required the following non-standard parameters: (i) a frequency range of 0.2-4.0 ppm for the right fit and 6.4-7.6 ppm for the left fit (PPMST=8.5, PPMEND=0.2, PPMGAP=[6.5, 4.0]), (ii) negligible water attenuation due to T2 effects (ATTH2O=1.0, ATTMET=1.0) as it was considered in a later point for the absolute concentration calculations, (iii) full water concentration in the volume (WCONC=55556), and (iv) two soft constraints (NRATIO=2) based on the ratio between right and left resonances of Phe and Tyr obtained from the phantom calibrations. T1 effects of both water and metabolites were assumed to be equivalent and therefore were not included in the correction factors.

6.2.5. Calibration and Absolute Quantification

Absolute concentration values were calculated from the quantified spectrum after correction of water content, T2 relaxation of both water and metabolite signals (h_{T2}), scanner specific gain calibrations and tissue fractions in the scanned volume. T1 effects of water and metabolites were assumed to be equivalent and therefore were not included in the correction

factors. Tissue fractions corresponded to the partial volume of gray matter (p_{GM}), white matter (p_{WM}) and cerebrospinal fluid (p_{CSF}), in the measured volume and were computed from the segmented of the T1 weighted (T1w) anatomical volume at the MRS voxel location. The segmentation process was performed using the FSL software library [42] after skull removal from the T1w volume. Mean values of all the cohorts were used to correct for the water content in PCG (p_{GM} = 0.532 $\pm$ 0.073, p_{WM} = 0.345 $\pm$ 0.067, p_{CSF} = 0.124 $\pm$ 0.066) and PWM (p_{GM} = 0.194 $\pm$ 0.09, p_{WM} = 0.774 $\pm$ 0.11, p_{CSF} = 0.032 $\pm$ 0.025).

The absolute metabolite concentrations per total volume of brain tissue $C_{met}^{V_total}$ (mol/L) were obtained from the following expression:

$$C_{\text{met}}^{V_{\text{total}}} = R_{\text{met}}^{\text{LCM}} \times h^{\text{Tissue}} \times h_{\text{met}}^{\text{Cal}}, \tag{6.1}$$

where $R_{\text{met}}^{\text{LCM}}$ corresponds to the ratio between the area of the metabolite fit and the water reference signal obtained from LCModel, and $h_{\text{met}}^{\text{Cal}}$ represents the metabolite specific correction factor obtained from the calibration scan. The tissue correction factor h^{Tissue} was calculated as follows:

$$h^{\text{Tissue}} = (0.78 \cdot h_{\text{GM}}^{T_2} \cdot p_{GM}) + (0.65 \cdot h_{\text{WM}}^{T_2} \cdot p_{WM}) + (1.0 \cdot h_{\text{CSF}}^{T_2} \cdot p_{CSF}) \tag{6.2}$$

where $h_{\text{Tissue}}^{T_2}$ is the correction factor for the T_2 decay of water in the corresponding tissue type ($h_{\text{GM}}^{T_2} = h_{\text{WM}}^{T_2} = h_{\text{CSF}}^{T_2} = 0.646$).

The absolute metabolite concentration per volume of brain tissue $C_{\text{met}}^{V_{\text{Brain}}}$ (mol/L) was computed by only including the contribution of the brain tissue volume ($V_{\text{Brain}} = 1 - p_{\text{CSF}}$):

$$C_{\text{met}}^{V_{\text{Brain}}} = (0.78 \cdot h_{\text{GM}}^{T_2} \cdot p_{GM}) + (0.65 \cdot h_{\text{WM}}^{T_2} \cdot p_{WM}) + (1.0 \cdot h_{\text{CSF}}^{T_2} \cdot p_{CSF}) \tag{6.3}$$

To obtain absolute concentration values per mass of brain tissue $C_{\text{met}}^{m_{\text{Brain}}}$ (mol/kg), the concentration per volume of brain tissue is divided by the brain tissue density ($_{\text{Brain}} = 1.05 kg/L$):

$$h^{\text{Tissue}} = (0.78 \cdot h_{\text{GM}}^{T_2} \cdot p_{GM}) + (0.65 \cdot h_{\text{WM}}^{T_2} \cdot p_{WM}) + (1.0 \cdot h_{\text{CSF}}^{T_2} \cdot p_{CSF}) \tag{6.4}$$

Finally, the residual baseline component from macromolecules and other low concentration metabolites that contribute to $C_{\text{Phe}}^{m_{\text{Brain}}}$ were subtracted from the estimated concentrations. The offset values were individually computed for PCG and PWM from the difference between the mean Phe concentration obtained from this technique and the expected mean concentration of Phe published in the literature [84, 83, 70], obtained from biopsy and autopsy samples of healthy controls.

6.3. Results

The quantification approach was tested on 68 spectra acquired from PKU subjects and controls measured at the posterior cingulate gyrus (PCG) and parietal white matter (PWM) locations. A single spectrum with high SNR and relatively high Phe was generated by averaging all the spectra included in the study after proper phasing and frequency alignment (Fig. 6.1). This qualitatively showed the performance of the fit and the detection of the down-field resonances, specifically Phe, NAA and Hcar. The phantom experiments were performed to obtain calibration factors at both scanners considered for the calculation of absolute concentrations (Fig. 6.2). The average volume and gain correction factors related to the specific excitation and refocusing pulses in the sequence and B1+ robustness were calculated for the four different phantoms. The mean correction factors obtained from the four acquisitions at each scanner were 1.73 for the Trio measurements and 2.04 for the Skyra measurements. The fitting results for the up-field and down-field spectra were qualitatively assessed and compared between PKU subjects and controls (Fig. 6.3). Reduced baseline influence and relatively flat residuals were observed consistently throughout the cohorts even for low Phe levels. Moreover, this comparison showed a noticeable increase in the Phe peak located at 7.4 ppm in PKU subjects compared to controls.

Absolute metabolite concentrations per mass of brain tissue (μmol/kg) were calculated following the previously described methodology. As a validation step for the quantification of absolute concentrations, the correction factors were also applied to Cr and NAA, which are assumed to be stable in this condition. The results were compared to values previously

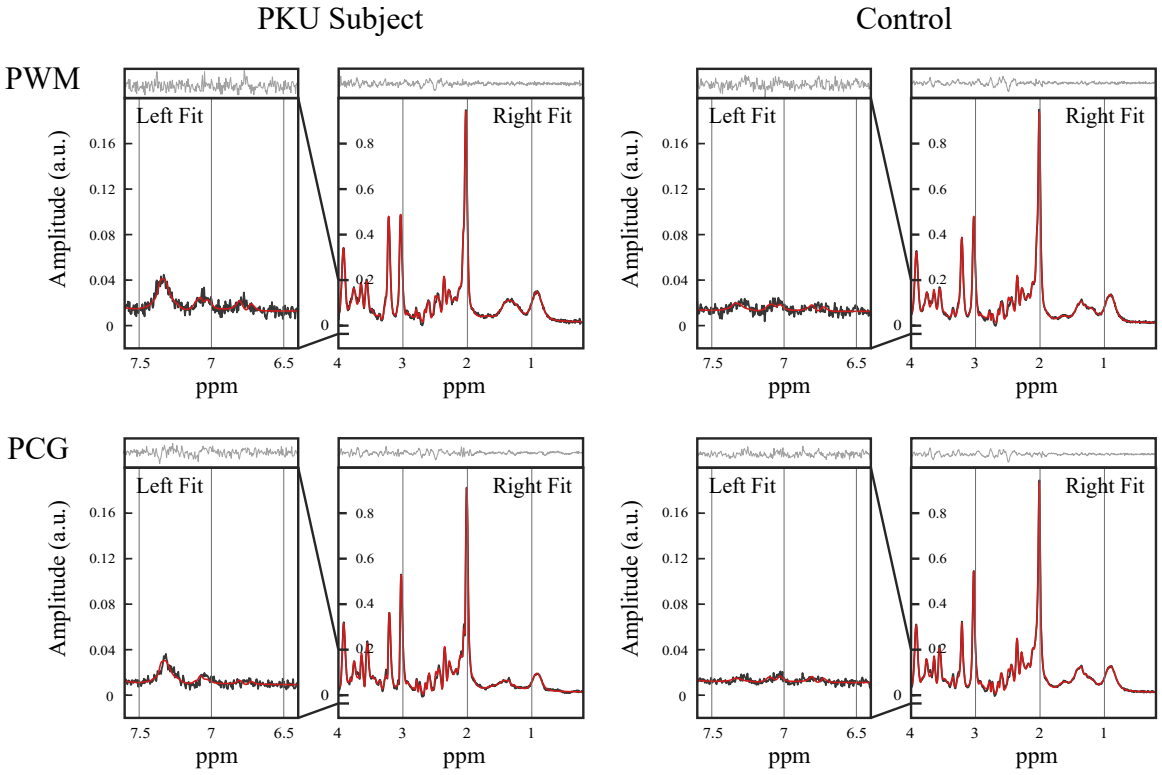

Figure 6.3.: Fitting results of the in vivo measurements shown for a PKU subject (left) and a healthy control (right) at two brain locations, namely the parietal white matter (PWM) and the posterior cingulate gyrus (PCG). The result of the LCModel fit and the residuals for both the down-field (Left Fit) and the up-field (Right Fit) signals is shown. The signal amplitude was normalized to the maximum of the NAA peak and presented in arbitrary units (a.u.) to allow for comparison between the left and right fits.

reported in the literature [53]. The mean absolute concentration of total NAA was 10.5 $\pm$ 0.9 mmol/kg in gray matter and 8.2 $\pm$ 0.6 mmol/kg in white matter. For total Cr, a mean absolute concentration of 7.0 $\pm$ 0.5 mmol/kg in gray matter and 4.7 $\pm$ 0.3 mmol/kg in white matter was found for the analyzed subjects.

A sensitivity analysis for the proposed Phe quantification method was performed using all the 68 acquired spectra (Fig. 6.4). The absolute concentrations ranged between 21 and 728 μmol/kg. Additionally, a mean absolute error of 87 μmol/kg was calculated from the data. Furthermore, CRLB values were used to define three different categories to standardize the data analysis and identify outliers without excluding them from the analysis [55]. The

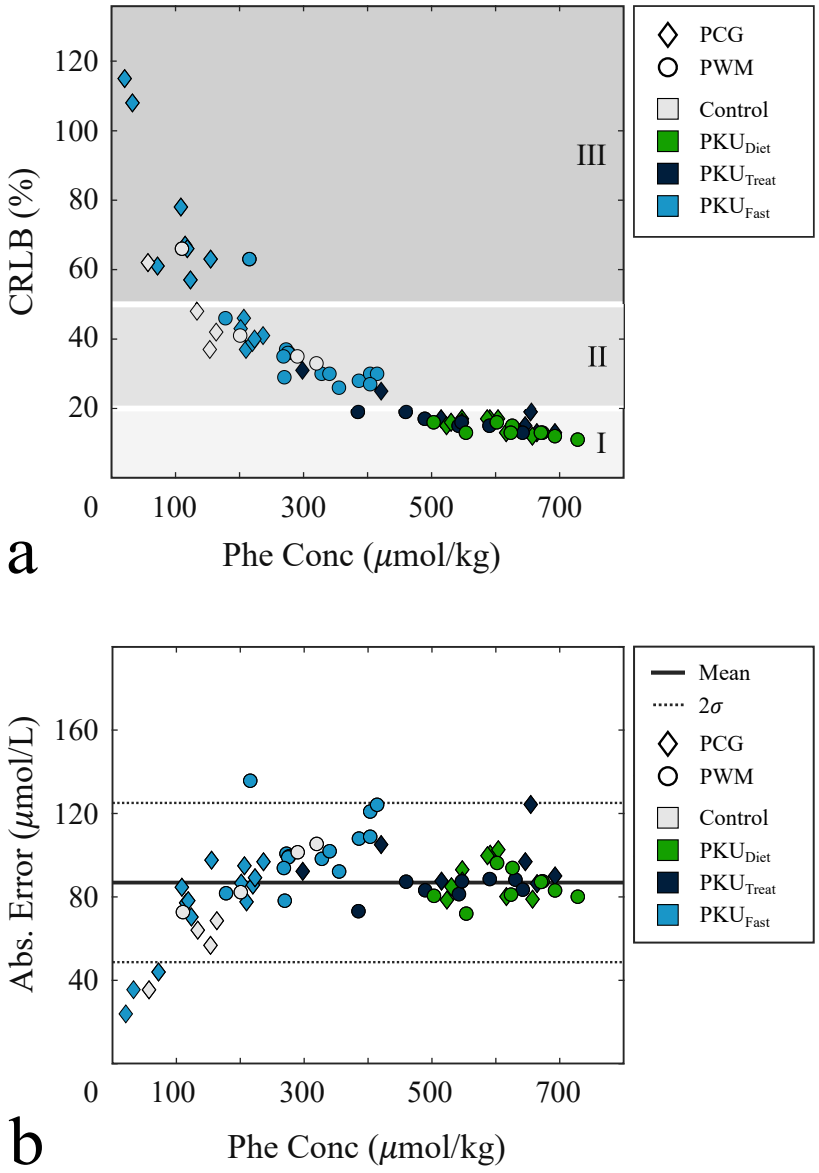

Figure 6.4.: Sensitivity analysis for the Phe quantification technique shown for all PKU cohorts and the control group at both PCG (diamond) and PWM (circle) locations. A total of 68 data points ranging from concentrations below the detection limit (100 μmol/kg) to reliably quantified concentrations up to 700 μmol/kg. (a) Cramer Rao lower bounds (CRLB) shown relative to the Phe absolute concentration. Three different CRLB ranges were empirically defined to standardize the analysis of without excluding data points: (I) reliable quantification of Phe, (II) reliable metabolite detection but unreliable quantification and (III) unreliable detection of Phe. (b) Absolute quantification error measured from the measured value and the CRLB. The plot shows the mean absolute error and the 2σ limit interval that contains most of the values.

samples were classified in the following groups: (I) samples with a reliable quantification of Phe, (II) samples with a reliable detection of Phe but an unreliable quantification and (III) samples for which both the detection and quantification of Phe was unreliable.

6.4. Discussion

This work presented a methodology to measure Phe in the brain using standard and widely available methods, namely, PRESS localized sequences and LCModel quantification. The approach modeled the metabolite components up-field from the water signal using nuclear magnetic resonance (NMR) simulations to create an accurate representation of the metabolite signal, effectively incorporating prior knowledge to the quantification. The residuals down-field from the water signal were in the same order of magnitude as the upstream residuals, showing a relatively small contribution of baseline effects or macromolecules. The use of independent basis functions for down-field and up-field resonances of Phe and Tyr avoided errors caused by highly overlapping frequencies up-field from the water signal that could lead to wrong metabolite concentration estimates. Phe quantification using LCModel showed to be advantageous as it provides quality measures, i.e. CRLB, of the reliability and confidence intervals for all quantified metabolite, allowing to get an objective measure of the sensitivity of this technique. A calibration phantom with known metabolic concentrations was developed to perform scanner specific calibrations of the measurement. Despite the phantom calibrations performed and the corrections applied to the data accounted for the main differences expected in datasets, achieving highly consistent in absolute concentrations of Phe remains challenging in multi-site studies due to potential variability of the sequences and MR systems. With the present analysis, a range for the sensitivity of this quantification technique was determined from absolute concentrations. A 100% uncertainty in concentration values, which corresponds to a CRLB of 50%, was assumed to be the detection limit of the technique (Fig. 4, group III). In general, the detection limit was 100 μmol/kg and only concentrations over 400 μmol/kg could be reliably quantified. The measured values agree with literature biopsies and autopsy results for both

controls and PKU subjects [84, 83, 70]. From all the samples analyzed, a mean absolute error of 87 μmol/kg for volumes of 24 and 27 mL. The scanned volumes corresponded to an effective excited volume of in the range of 12 to 15.9 mL for the Phe down-field resonances. Given the reduced Tyr expected in PKU and the low concentration of Tyr in the brain under normal conditions, reported in the range of 100 to 200 μmol/kg [84, 83, 70], a reliable detection of this metabolite was not possible with the current methodology. Measurements of spatial variations of Phe over small volumes can be performed using spatial encoding, i.e. MR spectroscopic imaging (MRSI) approaches. Moreover, the acquisition presented here, achieved in a 32-average scan (1 min), would allow for reliable dynamic measurements of Phe concentrations in the brain.

6.5. Limitations

Improvements in the sensitivity of this methodology can be achieved through different approaches that remain to be explored. First, the measurement of larger volume sizes with more signal averages can be performed and has shown to be effective for the detection of Phe [54, 56], however, this reduces the local tissue information and temporal context that is of interest in PKU studies. Furthermore, up to 2-fold signal increase, can be potentially achieved by shifting the center frequency of the RF pulses, typically at 2.4 ppm, closer to the Phe resonance, improving the excitation and refocusing of the down-field resonances. For sequences that incorporate RF pulses with limited bandwidth, a more robust localization could be achieved via an interleaved acquisition of one excitation with center frequency at 3.0 ppm (Cr) followed by one at 7.4 ppm (Phe). Similarly, acquisition sequences that incorporate adiabatic pulses, such as semi LASER [4, 102, 101], can improve the localization and measurement of down-field resonances by reducing the CSDE with no SNR loss. Finally, Phe quantification at higher magnetic fields, e.g. 7T, would benefit from higher SNR and spectral dispersion, allowing to decouple specific metabolites from the baseline.

Part IV.

Conclusion

7. Conclusion

In the work described in this thesis, scientific contributions in Magnetic Resonance Spectroscopy (MRS) and Spectroscopic Imaging (MRSI) were presented. As described in the initial chapters, the physical principles, hardware and clinical applications of these techniques have fundamental challenges that may benefit from novel methodologies and algorithms. Mainly, both present a potential clinical value, which motivates for developments that facilitate and broaden their use in the medical practice. Moreover, these modalities face some of the common challenges of medical imaging technologies, such as the need for faster more robust acquisitions with improved sensitivity that can give meaningful diagnostic insight to clinicians.

In the field of MRSI, developments presented in this work addressed the main limitations of the modality in three major categories: (i) improving SNR and spectral quality through novel reconstruction and processing techniques, (ii) achieving highly accelerated scans with robust acquisition techniques and (iii) enabling high-resolution examinations exploiting the increased sensitivity at ultra-high magnetic fields.

First, a methodology for fast ^{1}H MRSI of the brain with improved stability, enhanced SNR, and reduced spectral artifacts was designed (Chapter 3). The method achieved high acceleration factors (R>5) using echo-planar spectroscopic imaging (EPSI). Furthermore, a reconstruction framework with high-order phase correction allowed to effectively correct for phase distortions, caused mainly by B_0 inhomogeneities, B_0 drift, eddy currents, and system

vibrations. The proposed acquisition sequence measured a water-unsuppressed reference scan interleaved and the metabolite signal (i.e. water suppressed) in each phase encoding. This maximized the temporal and spatial correlation between both MRSI datasets, thus improving robustness to instabilities and motion. The described approach demonstrated substantial SNR enhancement (3-4 fold), spectral linewidth improvements, and an effective artifact removal with a single correction step without requiring extra measurements. Moreover, the acceleration factors achieved were comparable to undersampled acquisitions and parallel imaging reconstructions. In this way, smaller voxel sizes with improved metabolite signal can be achieved in a short acquisition ($<$5 min), enabling reliable metabolite mapping at 3T.

Second, a method for robust high-resolution ^{1}H MRSI scans optimized for ultra-high field (7T) was introduced (Chapter 4). Brain MRSI measurements with high spectral quality were acquired in clinically feasible scan times (5 min) and within SAR limits. Moreover, a phase correction (PC) algorithm for symmetric EPSI enabled high bandwidth scans avoiding the need for a separate reconstruction of the even and odd lines of the trajectory. Spectral ghosting was effectively removed with results comparable to performing eddy current correction (ECC), which requires a longer fully-encoded water reference scan. High-resolution (0.25–0.375 mL) metabolite ratio maps were obtained with the presented methodology. The correlation of the reconstructed maps with anatomical structures demonstrated the diagnostic potential of the technique to differentiate tissues based on their metabolic composition.

Finally, advances towards an improved quantification of the metabolic composition of brain tissue in MRS have been presented. On one side, machine learning algorithms were implemented (Chapter 5) to achieve scans with high accuracy, reproducibility, and reduced human errors. The method estimated the partial volume of tissues present in an MRS scan, which is crucial for proper correction of the concentrations measured at different brain regions. The proposed simplified pipeline showed its potential to scale the use of reliable MRS scans. On the other side, the measurement and quantification of low-concentration downfield metabolites present in a proton spectrum were demonstrated using standard sequences and widely available software (Chapter 6). This methodology

was validated in the specific field of metabolic disorders, specifically for the monitoring of brain phenylalanine in subjects with phenylketonuria.

This work described solutions to current clinical challenges and demonstrated how established applications, like MRS and MRSI, can benefit from novel hardware and software technologies. The ultimate goal is to push forward the use of these modalities in clinical applications where they can provide value and positively impact patient care.

Bibliography

[1] Reduction of spectral ghost artifacts in high-resolution echo-planar spectroscopic imaging of water and fat resonances. *Magnetic Resonance in Medicine*, 49(6):1113–1120, 2003. 57

[2] Paula Agostinho, Rodrigo A. Cunha, and Catarina Oliveira. Neuroinflammation, Oxidative Stress and the Pathogenesis of Alzheimers Disease. *Current Pharmaceutical Design*, 16(25):2766–2778, aug 2010. 19

[3] Zhongxu An, Vivek Tiwari, Sandeep K. Ganji, Jeannie Baxter, Michael Levy, Marco C. Pinho, Edward Pan, Elizabeth A. Maher, Toral R. Patel, Bruce E. Mickey, and Changho Choi. Echo-planar spectroscopic imaging with dual-readout alternated gradients (DRAG-EPSI) at 7 T: Application for 2-hydroxyglutarate imaging in glioma patients. *Magnetic Resonance in Medicine*, 00(July), aug 2017. 57, 58

[4] Ovidiu C. Andronesi, Saadallah Ramadan, Eva Maria Ratai, Dominique Jennings, Carolyn E. Mountford, and A. Gregory Sorensen. Spectroscopic imaging with improved gradient modulated constant adiabaticity pulses on high-field clinical scanners. *Journal of Magnetic Resonance*, 203(2):283–293, 2010. 15, 56, 59, 91, 101

[5] Rowland B, John M. Irvine Mariano L, and Lin AP. OpenMRSLab: An open-source software repository for Magnetic Resonance Spectroscopy data analysis tools. *International Society for Magnetic Resonance in Medicine MR Spectroscopy Workshop*, 2016. 82, 95

[6] P B Barker. N-acetyl aspartate–a neuronal marker? *Annals of neurology*, 49(4):423–4, apr 2001. 17

[7] Peter B. Barker, Alberto Bizzi, Nicola De Stefano, Rao Gullapalli, and Doris D. M. Lin. *Clinical MR Spectroscopy: Techniques and Applications*. Cambridge University Press, 2009. 3

[8] H. Barkhuijsen, R. de Beer, and D. van Ormondt. Improved algorithm for noniterative time-domain model fitting to exponentially damped magnetic resonance signals. *Journal of Magnetic Resonance (1969)*, 73(3):553–557, jul 1987. 30, 63

[9] E. Bartholdi and R. R. Ernst. Fourier spectroscopy and the causality principle. *Journal of Magnetic Resonance (1969)*, 11(1):9–19, 1973. 28

[10] Ipshita Bhattacharya and Mathews Jacob. Compartmentalized low-rank recovery for high-resolution lipid unsuppressed MRSI - Supplementary Information. *Magnetic Resonance in Medicine*, 2017. 30

[11] W. Bogner, S. Gruber, S. Trattnig, and M. Chmelik. High-resolution mapping of human brain metabolites by free induction decay 1H MRSI at 7T. *NMR in Biomedicine*, 25(6):873–882, 2012. 36, 56

[12] Jorge Zavala Bojorquez, Stéphanie Bricq, Clement Acquitter, François Brunotte, Paul M. Walker, and Alain Lalande. What are normal relaxation times of tissues at 3 T? *Magnetic Resonance Imaging*, 35:69–80, 2017. 11

[13] P A Bottomley. Spatial localization in NMR spectroscopy in vivo. *Annals of the New York Academy of Sciences*, 508:333–48, nov 1987. 56, 90

[14] Paul Bottomley. Selective volume method for performing localized NMR spectroscopy, 1985. 22

[15] J Canny. A computational approach to edge detection. *IEEE transactions on pattern analysis and machine intelligence*, 8(6):679–698, 1986. 64

[16] Eduardo Caverzasi, Anna Pichiecchio, Guy Umberto Poloni, Alessandro Calligaro, Moreno Pasin, Fulvia Palesi, Gloria Castellazzi, Massimo Pasquini, Massimo Biondi, Francesco Barale, and Stefano Bastianello. Magnetic resonance spectroscopy in the evaluation of treatment efficacy in unipolar major depressive disorder: a review of the literature. *Functional neurology*, 27(1):13–22, 2012. 18

[17] Paul Chang, Sahar Nassirpour, and Anke Henning. Modeling real shim fields for very high degree (and order) B0 shimming of the human brain at 9.4 T. *Magnetic resonance in medicine*, 79(1):529–540, jan 2018. 36

[18] Mark Chiew, Wenwen Jiang, Brian Burns, Peder Larson, Adam Steel, Peter Jezzard, M. Albert Thomas, and Uzay E. Emir. Density-weighted concentric rings k -space trajectory for 1 H magnetic resonance spectroscopic imaging at 7 T. *NMR in Biomedicine*, 31(1):e3838, jan 2018. 73

[19] Charles H. Cunningham, Daniel B. Vigneron, Albert P. Chen, Duan Xu, Sarah J. Nelson, Ralph E. Hurd, Douglas A. Kelley, and John M. Pauly. Design of flyback echo-planar readout gradients for magnetic resonance spectroscopic imaging. *Magnetic Resonance in Medicine*, 54(5):1286–1289, 2005. 37, 56

[20] Robin A. de Graaf. *in vivo NMR Spectroscopy - Principles and Techniques*. Wiley, 2 edition, 2007. 7, 8, 9, 15, 17, 30

[21] Dinesh K. Deelchand, James M. Joers, Karim Snoussi, Meng Gu, Ralph Noeske, Daniel M. Spielman, Brian J. Soher, Peter B. Barker, and Gülin Öz. Across-vendor standardization of semi-LASER for single-voxel MRS at 3 Tesla. In *ISMRM Workshop on MR Spectroscopy*, page 49, 2016. 59

[22] Sean C.L. Deoni. Quantitative Relaxometry of the Brain. *Topics in Magnetic Resonance Imaging*, 21(2):101–113, apr 2010. 11, 12

[23] Olaf Dössel and Thorsten M. Buzug. Magnetische Resonanztomographie. In *Biomedi-*

zinische Technik - Medizinische Bildgebung, chapter 9, pages 327–406. de Gruyter, 2014. 8, 9, 14

[24] Ralf Dringen, Jan M Gutterer, and Johannes Hirrlinger. Glutathione metabolism in brain. *European Journal of Biochemistry*, 267(16):4912–4916, aug 2000. 19

[25] Andreas Ebel, Wolfgang Dreher, and Dieter Leibfritz. Effects of zero-filling and apodization on spectral integrals in discrete Fourier-transform spectroscopy of noisy data. *Journal of Magnetic Resonance*, 182(2):330–338, 2006. 28

[26] Andreas Ebel and Andrew A. Maudsley. Detection and correction of frequency instabilities for volumetric 1H echo-planar spectroscopic imaging. *Magnetic Resonance in Medicine*, 53(2):465–469, 2005. 36

[27] Adalsteinsson Elfar, Irarrazabal Pablo, Topp Simon, Meyer Craig, Macovski Albert, and Spielman Daniel M. Volumetric spectroscopic imaging with spiral-based k-space trajectories. *Magnetic Resonance in Medicine*, 39(6):889–898. 26

[28] J Frahm, K D Merboldt, and W Hanicke. Localized proton spectroscopy using stimulated echoes. *Journal of Magnetic Resonance*, 72(3):502–508, 1987. 56, 90

[29] Jon K. Furuyama, Neil E. Wilson, and M. Albert Thomas. Spectroscopic imaging using concentrically circular echo-planar trajectories in vivo. *Magnetic Resonance in Medicine*, 67(6):1515–1522, jun 2012. 73

[30] Jeremy W. Gordon, Daniel B. Vigneron, and Peder E.Z. Larson. Development of a symmetric echo planar imaging framework for clinical translation of rapid dynamic hyperpolarized 13 C imaging. *Magnetic Resonance in Medicine*, 77(2):826–832, feb 2017. 26, 57

[31] V Govindaraju, K Young, and A A Maudsley. Proton NMR chemical shifts and coupling constants for brain metabolites. *NMR Biomed*, 13:129–153, 2000. 15, 18, 19, 92

[32] Mark A. Griswold, Peter M. Jakob, Robin M. Heidemann, Mathias Nittka, Vladimir Jellus, Jianmin Wang, Berthold Kiefer, and Axel Haase. Generalized Autocalibrating

Partially Parallel Acquisitions (GRAPPA). *Magnetic Resonance in Medicine*, 47(6):1202–1210, 2002. 29, 37

[33] R Gruetter, E J Novotny, S D Boulware, G F Mason, D L Rothman, G I Shulman, J W Prichard, and R G Shulman. Localized 13C NMR spectroscopy in the human brain of amino acid labeling from d-[1-13C]glucose. *Journal of Neurochemistry*, 63(4):1377–1385, 1994. 18

[34] A Haase, J Frahm, W Hänicke, and D Matthaei. 1H NMR chemical shift selective (CHESS) imaging. *Physics in medicine and biology*, 30(4):341–344, 1985. 23, 57

[35] Gilbert Hangel, Bernhard Strasser, Michal Považan, Eva Heckova, Lukas Hingerl, Roland Boubela, Stephan Gruber, Siegfried Trattnig, and Wolfgang Bogner. Ultra-high resolution brain metabolite mapping at 7 T by short-TR Hadamard-encoded FID-MRSI. *NeuroImage*, (October), nov 2016. 25, 36, 56

[36] Kent Harris, Alexander Lin, Pratip Bhattacharya, Thao Tran, Willis Wong, and Brian Ross. Regulation of NAA-Synthesis in the Human Brain in Vivo: Canavan's Disease, Alzheimer's Disease and Schizophrenia. In *N-Acetylaspartate*, volume 576, pages 263–273. Springer US, jan 2006. 17

[37] Anke Henning, Alexander Fuchs, James B. Murdoch, and Peter Boesiger. Slice-selective FID acquisition, localized by outer volume suppression (FIDLOVS) for 1H-MRSI of the human brain at 7 T with minimal signal loss. *NMR in Biomedicine*, 22(7):683–696, 2009. 56

[38] L Hertz and H R Zielke. Astrocytic control of glutamatergic activity: astrocytes as stars of the show. *Trends in Neurosciences*, 27(12):735–743, 2004. 18

[39] R S Hinks, B J MOck, B D Collick, F J Frigo, and T Shubhachint. Method and System for Image Artifact Reduction Using Nearest-Neighbor Phase Correction for Echo Planar Imaging. 2(12), 2006. 57

[40] Jeffrey C. Hoch and Alan S. Stern. *NMR Data Processing*. Wiley, 1996. 28, 30

[41] Wei Huang, Paul R. Fisher, Khaldoon Dulaimy, Luminita A. Tudorica, Brian O'Hea, and Terry M. Button. Detection of breast malignancy: Diagnostic mr protocol for improved specificity. *Radiology*, 232(2):585–591, 2004. PMID: 15205478. 3

[42] Mark Jenkinson, Christian F. Beckmann, Timothy E.J. Behrens, Mark W. Woolrich, and Stephen M. Smith. FSL. *NeuroImage*, 62(2):782–790, aug 2012. 79, 82, 96

[43] K Kantarci. 1H magnetic resonance spectroscopy in dementia. *The British journal of radiology*, 80 Spec No:S146–52, dec 2007. 17

[44] Kejal Kantarci. Proton MRS in mild cognitive impairment. *Journal of magnetic resonance imaging : JMRI*, 37(4):770–7, apr 2013. 19

[45] Dong-Hyun Kim, Elfar Adalsteinsson, and Daniel M. Spielman. Spiral readout gradients for the reduction of motion artifacts in chemical shift imaging. *Magnetic Resonance in Medicine*, 51(3):458–463, mar 2004. 73

[46] Thomas Kirchner, Ariane Fillmer, and Anke Henning. Mechanisms of SNR and Line Shape Improvement by B0 Correction in Overdiscrete MRSI Reconstruction. *Magnetic Resonance in Medicine*, 77(1):44–56, 2017. 37, 38

[47] Thomas Kirchner, Ariane Fillmer, Jeffrey Tsao, Klaas Paul Pruessmann, and Anke Henning. Reduction of Voxel Bleeding in Highly Accelerated Parallel 1H MRSI by Direct Control of the Spatial Response Function. *Magnetic resonance in medicine*, 73(2):469–80, 2015. 37, 38

[48] Klaas P. Pruessmann, Markus Weiger, Peter Börnert, and Peter Boesiger. Advances in Sensitivity Encoding With Arbitrary\nk-Space Trajectories. *Magnetic Resonance in Medicine*, 46:638–651, 2001. 37

[49] U Klose. In vivo proton spectroscopy in presence of eddy currents. *Magn Reson Med*, 14(1):26–30, 1990. 29, 36

[50] Uwe Klose. Measurement sequences for single voxel proton MR spectroscopy. *European Journal of Radiology*, 67(2):194–201, 2008. 22

[51] Nina Vanessa Kraguljac, Meredith Reid, David White, Rebecca Jones, Jan den Hollander, Deborah Lowman, and Adrienne Carol Lahti. Neurometabolites in schizophrenia and bipolar disorder - a systematic review and meta-analysis. *Psychiatry research*, 203(2-3):111–25, 2012. 17

[52] R. Kreis. Comments on in vivo proton magnetic resonance spectroscopy in phenylketonuria. *European journal of pediatrics*, 159 Suppl:S126–8, oct 2000. 90

[53] R. Kreis, T. Ernst, and B.D. Ross. Absolute Quantitation of Water and Metabolites in the Human Brain. II. Metabolite Concentrations. *Journal of Magnetic Resonance, Series B*, 102(1):9–19, aug 1993. 98

[54] R. Kreis, J. Pietz, J. Penzien, N. Herschkowitz, and C. Boesch. Identification and Quantitation of Phenylalanine in the Brain of Patients with Phenylketonuria by Means of Localized in Vivo1H Magnetic-Resonance Spectroscopy. *Journal of Magnetic Resonance, Series B*, 107(3):242–251, jun 1995. 90, 101

[55] Roland Kreis. The trouble with quality filtering based on relative Cram??r-Rao lower bounds. *Magnetic Resonance in Medicine*, 75(1):15–18, 2016. 98

[56] Roland Kreis, K. Zwygart, C. Boesch, and J. M. Nuoffer. Reproducibility of cerebral phenylalanine levels in patients with phenylketonuria determined by 1H-MR spectroscopy. *Magnetic Resonance in Medicine*, 62(1):11–16, 2009. 90, 101

[57] Eriks Kupce and Ray Freeman. Stretched adiabatic pulses for broadband spin inversion. *Journal of Magnetic Resonance, Series A*, 117(2):246 – 256, 1995. 10

[58] John Kurhanewicz and Daniel B. Vigneron. Advances in mr spectroscopy of the prostate. *Magnetic Resonance Imaging Clinics of North America*, 16(4):697 – 710, 2008. Genitourinary MRI. 3

[59] Christian Labadie, Stefan Hetzer, Jessica Schulz, Toralf Mildner, Monique Aubert-Frécon, and Harald E. Möller. Center-out echo-planar spectroscopic imaging with

correction of gradient-echo phase and time shifts. *Magnetic Resonance in Medicine*, 70(1):16–24, 2013. 57

[60] Yan Li, Angela Jakary, Erin Gillung, Stuart Eisendrath, Sarah J. Nelson, Pratik Mukherjee, and Tracy Luks. Evaluating metabolites in patients with major depressive disorder who received mindfulness-based cognitive therapy and healthy controls using short-echo MRSI at 7 Tesla. *Magnetic Resonance Materials in Physics, Biology and Medicine*, 29(3):523–533, 2016. 68

[61] Alexander Lin, Brian D Ross, Kent Harris, and Willis Wong. Efficacy of proton magnetic resonance spectroscopy in neurological diagnosis and neurotherapeutic decision making. *NeuroRx : the journal of the American Society for Experimental NeuroTherapeutics*, 2(2):197–214, apr 2005. 17

[62] Michael Lustig and John M. Pauly. SPIRiT: Iterative self-consistent parallel imaging reconstruction from arbitrary k-space. *Magnetic Resonance in Medicine*, 64(2):457–471, 2010. 29, 37

[63] Richard J Maddock and Michael H Buonocore. MR Spectroscopic Studies of the Brain in Psychiatric Disorders. *Current topics in behavioral neurosciences*, feb 2012. 18

[64] Hai-Ling Margaret Cheng, Nikola Stikov, Nilesh R. Ghugre, and Graham A. Wright. Practical medical applications of quantitative mr relaxometry. *Journal of Magnetic Resonance Imaging*, 36(4):805–824, 2012. 11

[65] Wilson Martin, Reynolds Greg, Kauppinen Risto A., Arvanitis Theodoros N., and Peet Andrew C. A constrained least-squares approach to the automated quantitation of in vivo 1h magnetic resonance spectroscopy data. *Magnetic Resonance in Medicine*, 65(1):1–12. 30

[66] G F Mason, R Gruetter, D L Rothman, K L Behar, R G Shulman, and E J Novotny. Simultaneous determination of the rates of the TCA cycle, glucose utilization, mu-

ketoglutarate-Glutamate exchange, and glutamine synthesis in human brain by NMR. *Journal of Cerebral Blood Flow & Metabolism*, 15(1):12–25, 1995. 18

[67] Mario Mastrangelo, Flavia Chiarotti, Luana Berillo, Caterina Caputi, Claudia Carducci, Claudio Di Biasi, Filippo Manti, Francesca Nardecchia, and Vincenzo Leuzzi. The outcome of white matter abnormalities in early treated phenylketonuric patients: A retrospective longitudinal long-term study. *Molecular genetics and metabolism*, 116(3):171–7, nov 2015. 90

[68] Daisuke Matsuzawa and Kenji Hashimoto. Magnetic resonance spectroscopy study of the antioxidant defense system in schizophrenia. *Antioxidants & redox signaling*, 15(7):2057–65, oct 2011. 20

[69] Andrew A. Maudsley, Zhe Wu, Dieter J. Meyerhoff, and Michael W. Weiner. Automated processing for proton spectroscopic imaging using water reference deconvolution. *Magnetic Resonance in Medicine*, 31(6):589–595, jun 1994. 36

[70] Charles M. McKean. The effects of high phenylalanine concentrations on serotinin and catecholamine metabolism in the human brain. *Brain Research*, 47(2):469–476, 1972. 90, 97, 101

[71] Charles M. McKean and Neal A. Peterson. Glutamine in the Phenylketonuric Central Nervous System. *New England Journal of Medicine*, 283(25):1364–1367, dec 1970. 90

[72] Gregory Metzger and Xiaoping Hu. Application of Interlaced Fourier Transform to Echo-Planar Spectroscopic Imaging. *Journal of Magnetic Resonance*, 125(1):166–170, mar 1997. 57

[73] J R Moffett, M A Namboodiri, and J H Neale. Enhanced carbodiimide fixation for immunohistochemistry: application to the comparative distributions of N-acetylaspartylglutamate and N-acetylaspartate immunoreactivities in rat brain. *The journal of histochemistry and cytochemistry : official journal of the Histochemistry Society*, 41(4):559–70, apr 1993. 16

[74] John R Moffett, Brian Ross, Peethambaran Arun, Chikkathur N Madhavarao, and Aryan M A Namboodiri. N-Acetylaspartate in the CNS: from neurodiagnostics to neurobiology. *Progress in neurobiology*, 81(2):89–131, feb 2007. 17

[75] R Lee Mosley, Eric J Benner, Irena Kadiu, Mark Thomas, Michael D Boska, Khader Hasan, Chad Laurie, and Howard E Gendelman. Neuroinflammation, Oxidative Stress and the Pathogenesis of Parkinson's Disease. *Clinical neuroscience research*, 6(5):261–281, dec 2006. 19

[76] A. Naressi, C. Couturier, I. Castang, R. de Beer, and D. Graveron-Demilly. Java-based graphical user interface for mrui, a software package for quantitation of in vivo/medical magnetic resonance spectroscopy signals. *Computers in Biology and Medicine*, 31(4):269 – 286, 2001. 30

[77] Sahar Nassirpour, Paul Chang, Ariane Fillmer, and Anke Henning. A comparison of optimization algorithms for localized in vivo B0 shimming. *Magnetic resonance in medicine*, 79(2):1145–1156, feb 2018. 36

[78] Sahar Nassirpour, Paul Chang, and Anke Henning. High and ultra-high resolution metabolite mapping of the human brain using 1 H FID MRSI at 9.4T. *NeuroImage*, 168(July 2016):211–221, mar 2018. 25, 36, 56

[79] Ricardo Otazo, Bryon Mueller, Kamil Ugurbil, Lawrence Wald, and Stefan Posse. Signal-to-noise ratio and spectral linewidth improvements between 1.5 and 7 Tesla in proton echo-planar spectroscopic imaging. *Magnetic Resonance in Medicine*, 56(6):1200–1210, dec 2006. 37, 56, 63, 68

[80] Gülin Öz, Jeffry R. Alger, Peter B. Barker, Robert Bartha, Alberto Bizzi, Chris Boesch, Patrick J. Bolan, Kevin M. Brindle, Cristina Cudalbu, Alp Dinçer, Ulrike Dydak, Uzay E. Emir, Jens Frahm, Ramón Gilberto González, Stephan Gruber, Rolf Gruetter, Rakesh K. Gupta, Arend Heerschap, Anke Henning, Hoby P. Hetherington, Franklyn A. Howe, Petra S. Hüppi, Ralph E. Hurd, Kejal Kantarci, Dennis W. J.

Klomp, Roland Kreis, Marijn J. Kruiskamp, Martin O. Leach, Alexander P. Lin, Peter R. Luijten, Małgorzata Marjańska, Andrew A. Maudsley, Dieter J. Meyerhoff, Carolyn E. Mountford, Sarah J. Nelson, M. Necmettin Pamir, Jullie W. Pan, Andrew C. Peet, Harish Poptani, Stefan Posse, Petra J. W. Pouwels, Eva-Maria Ratai, Brian D. Ross, Tom W. J. Scheenen, Christian Schuster, Ian C. P. Smith, Brian J. Soher, Ivan Tkáč, Daniel B. Vigneron, and Risto A. Kauppinen. Clinical Proton MR Spectroscopy in Central Nervous System Disorders. *Radiology*, 270(3):658–679, 2014. 3, 16, 19, 36

[81] Gülin Öz and Ivan Tkáč. Short-echo, single-shot, full-intensity proton magnetic resonance spectroscopy for neurochemical profiling at 4T: Validation in the cerebellum and brainstem. *Magnetic Resonance in Medicine*, 65(4):901–910, apr 2011. 57

[82] L Pellerin and P Magistretti. Glutamate uptake into astrocytes stimulates aerobic glycolysis: A mechanism coupling neuronal activity to glucose utilization. *Proceedings of the National Academy of Sciences of the United States of America*, 91:10625–10629, 1994. 18

[83] T. L. Perry, K. Berry, S. Hansen, S. Diamond, and C. Mok. Regional Distribution of Amino Acids in Human Brain Obtained At Autopsy. *Journal of Neurochemistry*, 18(3):513–519, 1971. 90, 97, 101

[84] T. L. Perry, S. Hansen, K. Berry, C. Mok, and D. Lesk. Free Amino Acids and Related Compounds in Biopsies of Human Brain. *Journal of Neurochemistry*, 18(3):521–528, 1971. 90, 97, 101

[85] J. Pietz, R. Kreis, C. Boesch, J. Penzien, D. Rating, and N. Herschkowitz. The dynamics of brain concentrations of phenylalanine and its clinical significance in patients with phenylketonuria determined by in vivo1H magnetic resonance spectroscopy. *Pediatric Research*, 38(5):657–663, 1995. 90

[86] S Posse, C DeCarli, and D Le Bihan. Three-dimensional echo-planar MR spectroscopic imaging at short echo times in the human brain. *Radiology*, 192(3):733–738, 1994. 37, 56

[87] Stefan Posse, Ricardo Otazo, Stephen R. Dager, and Jeffry Alger. MR spectroscopic imaging: Principles and recent advances. *Journal of Magnetic Resonance Imaging*, 37(6):1301–1325, 2013. 27

[88] Stefan Posse, Gioacchino Tedeschi, Robert Risinger, Robert Ogg, and Denis Le Bihan. High Speed 1H Spectroscopic Imaging in Human Brain by Echo Planar Spatial-Spectral Encoding. *Magnetic Resonance in Medicine*, 33(1):34–40, 1995. 37, 56

[89] Michal Považan, Bernhard Strasser, Gilbert Hangel, Eva Heckova, Stephan Gruber, Siegfried Trattnig, and Wolfgang Bogner. Simultaneous mapping of metabolites and individual macromolecular components via ultra-short acquisition delay1H MRSI in the brain at 7T. *Magnetic Resonance in Medicine*, 00:1–10, 2017. 36, 56

[90] Subechhya Pradhan, Susanne Bonekamp, Joseph S. Gillen, Laura M. Rowland, S. Andrea Wijtenburg, Richard A.E. Edden, and Peter B. Barker. Comparison of single voxel brain MRS AT 3T and 7T using 32-channel head coils. *Magnetic Resonance Imaging*, 33(8):1013–1018, oct 2015. 68

[91] S W Provencher. Estimation of metabolite concentrations from localized in vivo proton NMR spectra. *Magnetic Resonance in Medicine*, 30(6):672–9, 1993. 30, 31, 43, 63, 65, 69, 70, 82, 91, 95

[92] Klaas P. Pruessmann, Markus Weiger, Markus B. Scheidegger, and Peter Boesiger. SENSE: Sensitivity encoding for fast MRI. *Magnetic Resonance in Medicine*, 42(5):952–962, 1999. 29, 37

[93] Gislaine T Rezin, Graziela Amboni, Alexandra I Zugno, João Quevedo, and Emilio L Streck. Mitochondrial dysfunction and psychiatric disorders. *Neurochemical research*, 34(6):1021–9, jun 2009. 17

[94] Christopher T. Rodgers and Matthew D. Robson. Receive array magnetic resonance spectroscopy: Whitened singular value decomposition (WSVD) gives optimal Bayesian solution. *Magnetic Resonance in Medicine*, 63(4):881–891, apr 2010. 28, 59

[95] Joseph R. Roebuck, David O. Hearshen, Matthew O'Donnell, and Tom Raidy. Correction of phase effects produced by eddy currents in solvent suppressed1H-CSI. *Magnetic Resonance in Medicine*, 30(3):277–282, sep 1993. 36, 70

[96] P B Roemer, W A Edelstein, C E Hayes, S P Souza, and O M Mueller. The NMR Phased Array. *Magnetic Resonance in Medicine*, 225(16):192–225, 1990. 28

[97] B Ross and S Bluml. Magnetic resonance spectroscopy of the human brain. *The Anatomical record*, 265(2):54–84, apr 2001. 19

[98] B D Ross. Real or imaginary? Human metabolism through nuclear magnetism. *IUBMB life*, 50(3):177–87, sep 2000. 17

[99] Niclas Sandgren, Petre Stoica, Frederick J. Frigo, and Yngve Selén. Spectral analysis of multichannel MRS data. *Journal of Magnetic Resonance*, 175(1):79–91, jul 2005. 28, 59

[100] T. Scarabino, T. Popolizio, M. Tosetti, D. Montanaro, G.M. Giannatempo, R. Terlizzi, S. Pollice, A. Maiorana, N. Maggialetti, A. Carriero, V. Leuzzi, and U. Salvolini. Phenylketonuria: white-matter changes assessed by 3.0-T magnetic resonance (MR) imaging, MR spectroscopy and MR diffusion. *La radiologia medica*, 114(3):461–474, apr 2009. 90

[101] T. W. Scheenen, Arend Heerschap, and D. W. Klomp. Towards 1H-MRSI of the human brain at 7T with slice-selective adiabatic refocusing pulses. *Magma (New York, N.Y.)*, 21(1-2):95–101, 2008. 23, 56, 101

[102] Tom W J Scheenen, Dennis W J Klomp, Jannie P. Wijnen, and Arend Heerschap. Short echo time 1H-MRSI of the human brain at 3T with minimal chemical shift displacement errors using adiabatic refocusing pulses. *Magnetic Resonance in Medicine*, 59(1):1–6, 2008. 23, 56, 101

[103] A Schousboe. Role of astrocytes in the maintenance and modulation of glutamatergic and GABAergic neurotransmission. *Neurochemical Research*, 28(2):347–352, 2003. 18

[104] A Schousboe and H Waagepetersen. Role of astrocytes in glutamate homeostasis: Implications for excitotoxicity. *Neurotoxicity Research*, 8(3):221–225, 2005. 18

[105] N R Sibson, A Dhankhar, G F Mason, D L Rothman, K L Behar, and R G Shulman. Stoichiometric coupling of brain glucose metabolism and glutamatergic neuronal activity. *Proceedings of the National Academy of Sciences of the United States of America*, 95(1):316–321, 1998. 18

[106] Bj Soher, D Semanchuk, D Todd, J Steinberg, and K Young. VeSPA: Integrated applications for RF pulse design, spectral simulation and MRS data analysis. In *Proceedings of the 19th Annual Meeting ISMRM*, 2011. 91

[107] Bernhard Strasser, Lukas Hingerl, Borjan A Gagoski, Philipp Moser, Gilbert Hangel, Siegfried Trattning, and Wolfgang Bogner. Comparison of Acceleration Methods for Brain MRSI at 7T. In *Proc. Intl. Soc. Mag. Reson. Med.*, page 1251, 2017. 73

[108] Melissa Terpstra, Ian Cheong, Tianmeng Lyu, Dinesh K. Deelchand, Uzay E. Emir, Petr Bednarík, Lynn E. Eberly, and Gülin Öz. Test-retest reproducibility of neurochemical profiles with short-echo, single-voxel MR spectroscopy at 3T and 7T. *Magnetic Resonance in Medicine*, 76(4):1083–1091, oct 2016. 68

[109] M Albert Thomas, Kenneth Yue, Nader Binesh, Pablo Davanzo, Anand Kumar, Benjamin Siegel, Mark Frye, John Curran, Robert Lufkin, Paul Martin, and Barry Guze. Localized two-dimensional shift correlated MR spectroscopy of human brain. *Magnetic Resonance in Medicine*, 46(1):58–67, jul 2001. 91

[110] I Tkác, Z Starcuk, I Y Choi, and R. Gruetter. In vivo 1H NMR spectroscopy of rat brain at 1 ms echo time. *Magnetic resonance in medicine*, 41(4):649–56, apr 1999. 24, 57

[111] J Urenjak, S R Williams, D G Gadian, and M Noble. Specific expression of N-acetylaspartate in neurons, oligodendrocyte-type-2 astrocyte progenitors, and immature oligodendrocytes in vitro. *Journal of neurochemistry*, 59(1):55–61, jul 1992. 16

[112] Marinette van der Graaf. In vivo magnetic resonance spectroscopy: basic methodology and clinical applications. *European Biophysics Journal*, 39(4):527–540, mar 2010. 3

[113] Leentje Vanhamme, Aad van den Boogaart, and Sabine Van Huffel. Improved method for accurate and efficient quantification of mrs data with use of prior knowledge. *Journal of Magnetic Resonance*, 129(1):35 – 43, 1997. 30

[114] Susan E. Waisbren, Sanjay P. Prabhu, Patricia Greenstein, Carter Petty, Donald Schomer, Vera Anastasoaie, Kalin Charette, Daniel Rodriguez, Sai Merugumala, and Alexander P. Lin. Improved Measurement of Brain Phenylalanine and Tyrosine Related to Neuropsychological Functioning in Phenylketonuria Susan. In *JIMD Reports*, volume 4, pages 113–116. 2012. 91

[115] Yonker Wang and Shi-Jiang Li. Differentiation of metabolic concentrations between gray matter and white matter of human brain by invivo1H magnetic resonance spectroscopy. *Magnetic Resonance in Medicine*, 39(1):28–33, jan 1998. 78, 86

[116] Z Wang, A.C. Bovik, H.R. Sheikh, and E.P. Simoncelli. Image Quality Assessment: From Error Visibility to Structural Similarity. *IEEE Transactions on Image Processing*, 13(4):600–612, apr 2004. 64

[117] Matthew L Zierhut, Esin Ozturk-Isik, Albert P Chen, Ilwoo Park, Daniel B Vigneron, and Sarah J Nelson. 1 H spectroscopic imaging of human brain at 3 Tesla: Comparison of fast three-dimensional magnetic resonance spectroscopic imaging techniques. *Journal of Magnetic Resonance Imaging*, 30(3):473–480, sep 2009. 37, 53, 57, 58